

**Centro de Investigación Científica y de Educación
Superior de Ensenada, Baja California**



**Doctor of Science
in Electronic and Telecommunication with
orientation in High Frequency Electronics**

**Measurement testbeds for the characterization of
nonlinear single and dual input devices using
multitones and modulated signals**

Tesis

para cubrir parcialmente los requisitos necesarios para obtener el grado de
Doctor en Ciencias

Presenta:

Thaimí Niubó Alemán

Ensenada, Baja California, México

2021

Tesis defendida por

Thaimí Niubó Alemán

y aprobada por el siguiente Comité

Dr. J. Apolinar Reynoso-Hernández

Codirector de tesis

Dr. Patrick Roblin

Codirector de tesis

Dra. María del Carmen Maya Sanchez

Dr. Humberto Lobato Morales

Dr. Jaime Sánchez García

Dr. José Raul Loo Yau



Dra. María del Carmen Maya Sanchez

Coordinadora del Posgrado en Electrónica y Telecomunicaciones

Dr. Pedro Negrete Regagnon

Director de Estudios de Posgrado

Thaimí Niubó Alemán © 2021

Queda prohibida la reproducción parcial o total de esta obra sin el permiso formal y explícito del autor y director de la tesis

Resumen de la tesis que presenta Thaimí Niubó Alemán como requisito parcial para la obtención del grado de Doctor en Ciencias en Electrónica y Telecomunicaciones con orientación en Altas Frecuencias.

Bancos de prueba para la caracterización de dispositivos no lineales de una y dos entradas utilizando multitonos y señales moduladas

Resumen aprobado por:

Dr. J. Apolinar Reynoso-Hernández

Codirector de tesis

Dr. Patrick Roblin

Codirector de tesis

En un sistema de comunicaciones móviles, el amplificador de RF es el elemento de mayor consumo de potencia y el cual introduce componentes espectrales no deseadas en la señal a transmitir. Su diseño debe proveer la mayor eficiencia posible, y disminuir las no linealidades para garantizar niveles de potencia en canales adyacentes que no generen interferencia y pérdidas de la información. En este trabajo se propone un banco de pruebas para evaluar la linealidad del mismo y de transistores utilizando señales continuas y multitono. Se utiliza una tarjeta secundaria de radiofrecuencia y un periférico universal de software de radio, para generar los tonos en banda base, y el analizador de redes vectoriales para medir las ondas incidentes y reflejadas en la entrada y salida del dispositivo bajo prueba. Se inspecciona la linealidad de los mismos bajo distintas impedancias de carga y fuente. El sistema de medición es un load-pull en tiempo real calibrado y capaz de obtener la fase y amplitud de la ganancia del dispositivo en gran señal para cualquier impedancia. Se realizó una interfaz gráfica en Matlab para el control y programación de los instrumentos del banco de prueba, facilitando la caracterización de estos dispositivos. Dísimiles configuraciones de amplificadores de potencia han sido propuestos en la literatura para proveer una alta eficiencia entre potencias de backoff y pico. Esencial en los sistemas de transmisión modernos, que trabajan con señales moduladas que presentan un valor elevado de relación de potencia pico a potencia promedio. Para la caracterización rápida de señales en banda base y la linealización de dispositivos multipuerto no lineales se propone por primera vez un banco de pruebas calibrado basado en un analizador de redes vectorial comercial. Este, permite adquirir señales continuas y periódicas moduladas de banda ancha sin romper contacto con el dispositivo, en hasta cinco canales. Las mediciones en el dominio del tiempo son posibles calibrando todos los receptores en el dominio de la frecuencia. Esta calibración proporciona una corrección de fase y amplitud para los tonos de modulación de todas las ondas incidentes y reflejadas en el ancho de banda de adquisición. Se emplea una señal de multiplexación por división de frecuencia ortogonal conocida como estándar de fase. Se recupera la constelación IQ de una señal de 500 MHz de ancho de banda, 100 000 tonos y modulada con un esquema 64 QAM OFDM, obteniendo una magnitud de vector de error del 0,48 %. Como aplicación, un amplificador de potencia de dos entradas y una salida, en una configuración híbrida Doherty-Chireix es caracterizado a 2,08 GHz. Se utiliza una señal de onda continua para determinar la diferencia de fase entre los puertos de entrada y los niveles de potencias, que proporcionan una eficiencia de drenador óptima y eficiencia de potencia agregada para cada potencia de salida. La respuesta dinámica de dicho amplificador se adquiere en cinco canales utilizando el mismo banco de pruebas. Varias señales periódicas OFDM, con 24 000 tonos, son medidas antes y después de la linealización en una fracción de segundo.

Palabras clave: Amplificadores de potencia, DPD, Doherty PA, Chireix PA, outphasing PA, dual input PA, Load-pull, Source-pull, OFDM.

Abstract of the thesis presented by Thaimí Niubó Alemán as a partial requirement to obtain the Doctor of Science degree in Sciences Postgraduate Program in Electronics and Telecommunications with orientation in High Frequency Electronics.

Measurement testbeds for the characterization of nonlinear single and dual input devices using multitones and modulated signals

Abstract approved by:

Dr. J. Apolinar Reynoso-Hernández

Thesis Co-Director

Dr. Patrick Roblin

Thesis Co-Director

In a mobile communication system, the RF amplifier is the element with the highest power consumption and which introduces unwanted spectral components in the signal to be transmitted. Its design must provide the highest possible efficiency, and reduce non-linearities to guarantee power levels in adjacent channels that do not generate interference and loss of information. In this work a test bench is proposed to evaluate the linearity of them and transistors using continuous and multitone signals. A radio frequency daughter card and universal radio software peripheral are used to generate the baseband tones, and the vector network analyzer is used to measure incident and reflected waves at the input and output of the device under test. Their linearity are inspected under different load and source impedances. The measurement system is a calibrated real-time load-pull capable of obtaining the phase and amplitude of the device's gain in large signal for any impedance. A graphical interface was created in Matlab for the control and programming of the test bench instruments, facilitating the characterization of these devices. Dissimilar power amplifier configurations have been proposed in the literature to provide high efficiency between backoff and peak powers. Essential in modern transmission systems, which work with modulated signals that have a high value of the peak to average power ratio. For the rapid characterization of baseband signals and the linearization of non-linear multiport devices, a calibrated test bench based on a commercial vector network analyzer is proposed for the first time. This allows the acquisition of continuous and periodic wideband modulated signals without breaking contact with the device, in up to five channels. Time domain measurements are possible by calibrating all receivers in the frequency domain. This calibration provides amplitude and phase corrections for the modulation tones of all incident and reflected waves in the acquisition bandwidth. An orthogonal frequency division multiplexing signal known, is used as phase standard. The IQ constellation is recovered from a signal of 500 MHz bandwidth, 100 000 tones and modulated with a 64 QAM OFDM scheme, with an error vector magnitude of 0.48%. As application, a two-input, one-output power amplifier in a hybrid Doherty-Chireix configuration is characterized at 2.08 GHz. A continuous wave signal is used to determine the phase difference between the input ports and the power levels, which provide optimal drain and added power efficiencies for each output power. The dynamic response of this amplifier is acquired in five channels using the same test bench. Several periodic OFDM signals, with 24,000 tones, are measured before and after linearization in a fraction of a second.

Keywords: Power Amplifier, DPD, Doherty PA, Chireix PA, outphasing PA, dual input PA, Load-pull, Source-pull, OFDM.

Dedication

***To my angels Yeyi, Grandma, Grandpa, and
my little sister Flavi.***

Thanks to

The Ensenada Center for Scientific Research and Higher Education opened the doors to the doctoral program in electronics and telecommunications. Thanks to the National Council of Science and Technology (CONACyT) for giving me financial support to carry out my doctoral studies under the scholarship number: 16141248 and the grants 638999, and CB 2013-222949-Y (Basic Sciences Project) and the US National Science Foundation under grant 1740119. Thanks to my advisors, professor J. Apolinar and professor Patrick who further opened the research world. I thank them infinitely for their outstanding dedication, guide, patience, knowledge, wisdom all these years and for sharing their passion for the investigation with me. Thanks to professors, María del Carmen Maya, Jaime Sánchez García, Humberto Lobato, José Raúl Loo Yau, for each of their suggestions and recommendations during my Ph.D. program. Thank you and professor José Luis Medina for your time and knowledge provided in classes. To professor Jorge Enriquez Preciado, who since the first day gave me a warm welcome to Ensenada. To professor Patrick' students, in special Chenyu Liang, and Yunsik Hahn, who collaborated and helped me during my research stay at OSU. To Cicese administrative staff that makes possible our stay in the center. To my Cuban friends in Ensenada, for all the good moments shared. To Clau, Dila, and Mirtha who gave me the welcome to Columbus, Ohio. Thanks to professor Jean Pierre, Dr. Jan Verspecht, Ing. Dexter Yamaguchi, and Keysight Technologies for the opportunity to work in this excellent company. To my parents for all the values instilled, for teaching me to pursue my dreams, for insisting not only on professional growth but also on being a better human being every day. Each of my achievements have been possible thanks to you. To my aunts, uncles, cousins, grandmother, who supported me at all times. To my goddaughter to bring bright to my days with just a smile. To my husband for deciding to share this path, thank you for your patience, support and to giving me strength when I needed it the most. Thanks to my sister, for being my Jiminy Cricket, for your wisdom, kindness, and your tireless warrior forces. For each of your sincere words, for being present each day of this journey no matter what. You always made me believe that everything is possible in this life. "Only the sky is the limits".

"Thanks to the life, that has gave me so much..."

Contents

	Página
Spanish Abstract	ii
English Abstract	iii
Dedication	iv
Thanks to	v
List of figures	ix
List of tables	xiv
List of abbreviations	xv
Chapter 1 Introduction	
1.1 Motivation	1
1.2 State of the art	2
1.3 General Objective	5
1.3.1 Specific objectives	6
Chapter 2 Vector Network Analyzer (VNA)	
2.1 Introduction	7
2.2 Scattering matrix definition	7
2.3 Vector Network Analyzer errors and models	8
2.3.1 3-term error model	10
2.3.2 12-term error model	11
2.3.3 8-term error model	12
2.3.4 Switch error correction	13
2.4 Calibration techniques	16
2.4.1 One-port calibration	17
2.4.1.1 Reflection standard models	18
2.4.2 Short-Open-Load-Reciprocal (SOLR) calibration technique	21
2.4.3 Quick-SOLT (QSOLT) calibration technique	26
2.4.4 Thru-Reflect-Line (TRL) calibration technique	27
Chapter 3 Load-Pull (LP) techniques	
3.1 Introduction	29
3.2 Conjugate and load line Match	32
3.2.1 Impact of the load line on the output power of a nonlinear device	33
3.2.1.1 Calculating the series reactance values, for which the average output power remains constant.	40
3.2.1.2 Calculating the shunts susceptance values, for which the average output power remains constant.	41
3.2.2 Transistor package effect on the constant power contours.	43
3.3 Load-Pull systems	45
3.3.1 Passive LP	47
3.3.1.1 Electromechanical Tuner (EMT)	47

Contents (continue)

3.3.1.2	Electronic Tuner (ETS)	49
3.3.1.3	Non-real-time, and real-time LP systems	50
3.3.2	Active LP	51
3.3.2.1	Closed-loop active LP system	52
3.3.3	Envelope LP systems	53
3.3.4	Feed-forward and open-loop LP systems	55
3.3.4.1	Improving the Feed-forward and open-loop LP systems	59
3.3.5	Harmonic LP system	62
3.3.6	Real-time multitone LP System	65
3.4	The proposed testbed	66
3.4.1	System calibration	67
3.4.2	Signal generation	71
3.5	Measurement Results	72
3.5.1	One tone measurement	72
3.5.2	Carrier to intermodulation with two tones	74
3.5.3	Multitone Load-pull results	75
Chapter 4	Calibrated digital predistortion using a VNA as the receiver	
4.1	Motivations	78
4.2	Description of the testbed	78
4.2.1	Processing the acquired data from the PNA-X	80
4.3	Measurements with LTE signal and linearization	81
4.3.1	Linearization results	81
4.3.2	Figures of merit	83
4.3.3	Testbed proposed to measure multiple input power amplifiers	83
4.4	Description of the testbed	86
4.4.1	Standard VNA calibration	88
4.4.2	Calibration of the VSNA	89
4.4.3	Extending the measurement frequency span of the VSNA until 500 MHz.	93
4.4.4	Measurements performed with the PNA-X-VSNA and VSA	95
Chapter 5	Multiple input single output PAs	
5.1	Introduction	100
5.2	Load Modulation techniques	102
5.2.1	Single input Doherty PA	102
5.2.1.1	Operating principle	102
5.2.2	Dual-input Doherty PA	104
5.2.3	Chireix PA	104
5.3	Hybrid Doherty Outphasing PA (HD-OPA)	105
5.3.1	HD-OPA characterization	106
5.3.2	Input signal alignment required for OPA characterization	106
5.3.3	CW measurements used to acquire the OPA LUT	107
5.3.4	HD-OPA characterization using modulated signals	114

Contents (continue)

5.3.5 Linearization results	116
Chapter 6 Conclusions and future work	
6.1 Future works	122
6.2 Publications	123
References	125
Appendix 1	130
Appendix 2	136

List of figures

Figure	Page
1 LP subcategories.	3
2 DUT of two-port.	8
3 Two-port VNA diagram.	9
4 1-port VNA configuration.	11
5 12-term error model signal flow diagram.	11
6 2-Port VNA diagram with 12-term error.	12
7 2-port VNA configuration with 8-term error	13
8 VNA diagram for the switch error corrections.	14
9 S-parameter magnitudes of a 6.8 cm line after removing the switch errors.	16
10 Model for reflection standard.	18
11 Signal flow graph model of an offset device.	19
13 Load standard models.	20
12 Open and short standard models of the cal Kit 85052-C.	21
14 Cascade representation of two-ports VNA.	22
15 Amplitude of the transmission tracking error (dB).	25
16 Phase of the transmission tracking error (°).	26
17 S-parameters of a 6.8 cm line without removing the switch errors.	27
18 Standards of the TRL technique.	28
19 General block diagram of an RFPA.	30
20 Linear and nonlinear behavior of RF PA.	30
21 I-V curves, with the load line of a FET transistor	32
22 Conjugate and load line Match (from Cripps (1999)).	32
23 Typical schematic of a FET amplifier.	34
24 Waveforms in class A RF PA.	35
25 Instantaneous output power in class A amplifier.	36
26 Drain waveforms in class A amplifier for different resistive loads, which produce the same output RF power.	37
27 Output voltage waveforms in class A amplifier that generate the same average output power $P_{o_{avg}}/p$, with Drain current swing $(0-2I_{DD})$	38
28 Load line trajectories to obtain the optimum average output power.	40
29 Class A amplifier with series reactance and pure resistive load $R_{LO} = R_{opt}/p$	41

List of figures (continue)

Figure	Page
30 Class A amplifier with shunt susceptance and a conductance $G_{HI} = 1/\rho R_{opt}$.	42
31 Constant power contour in Smith Chart.	42
32 2-port network used to emulate the effect of package on the constant power contours.	43
33 Rotation of the power contour along the constant conductance circle ($G = 1/\rho R_{opt}$).	44
34 Rotation of the power contour along the resistance constant circle ($R_L = R_{opt}/P$).	45
35 Setup to measure a nonlinear device with real-time LP system.	47
36 Electromechanical tuner (EMT).	48
37 Generic representation of the reflection coefficients generated with EMT.	49
38 Non-real-time LP systems setup.	51
39 Closed-loop active LP system.	52
40 Envelope LP system.	54
41 Active LP.	55
42 Circles in the plane bi/aj as function of $\angle a_2/a_1$ and center S_{ij}	57
43 Example of optimal and avoidable areas in the Smith Chart to characterize an hypothetical transistor.	59
44 Enhanced feed-forward LP system.	60
45 Behavior on the Smith Chart of the enhanced feed-forward LP system.	61
46 Comparing the power consumed by the classic and enhanced feed-forward LP systems.	62
47 Multiharmonic active LP system using feed-forward configuration.	63
48 Open harmonic active LP system configuration.	64
49 Testbed for linearity characterization.	66
50 TRL calibration. a) PNA-X configuration, b) error matrices, c) calibration standards.	68
51 Short-Open-Load (SOL) and absolute calibrations.	68
52 Device connected into the fixture.	69
53 GNU radio blocks to generate the baseband tones.	72

List of figures (continue)

Figure	Page
54 AM-AM, Gain and 2nd harmonic distortion of CGH40010F transistor.	73
55 AM-AM for different quiescent points of CGH40010F transistor.	73
56 AM-PM for different quiescent points of CGH40010F transistor.	73
57 Power contour CGH40010F transistor.	74
58 Carrier to Intermodulation (dBm).	75
59 Input spectrum of the DUT.	75
60 Output spectrum of the DUT.	76
61 Power contours and optimum impedances with multitone signals.	76
62 (a) Schematic and (b) picture of the testbed used for the measurements. .	79
63 DSP flowchart for the received signals.	80
64 Phase calibration ϕ_{CAL} corrections obtained for 11 different measurements.	81
65 Dynamic AM-AM and AM-PM curves of ZFL-2500 amplifier without DPD (black), its inverse (blue), with DPD (red).	82
66 Spectra of ZFL-2500 amplifier before and after DPD.	82
67 Constellations (a) for a thru: raw (red dots) and calibrated (blue dots)) with 20 MHz OFDM, and for the PA input (b) (blue dots) and output with DPD (c) and without DPD (d) for 5 MHz OFDM (red dots).	84
68 Proposed Vector Signal Network Analyzer (VSNA) testbed for the charac- terization and linearization of dual-input outphasing PAs.	87
69 Synchronization system connection.	88
70 Amplitude and phase calibration factors of VSNA (PNA-X) receivers R1,R2 and C.	91
71 Flowchart of the VSNA post-processing applied to the raw data of each channel to obtain the corrected multi-channel measurement data.	92
72 Verification of the VSNA calibration for a 100-MHz 16-QAM signal using the IQ constellations: (a) received and obtained after successively applying the VSNA (b) time alignment, (c) LO phase offset, (d) amplitude and (e) residual phase corrections.	92
73 Amplitude and phase corrections using a 500 MHz signal.	93
74 IQ-constellation of the received signal after corrections for a 64 QAM 500 MHz signal.	94

List of figures (continue)

Figure	Page
75 Phases of the subcarriers in the frequency domain vs the original ones. . .	94
76 Testbed to measure different OFDM signal with PNA-X and VSA.	95
77 Flowcharts, (a) To extract the phase and amplitude calibrations, and (b) to measure and correct a new signal.	96
78 PDF of different communication standards versus backoff power.	101
79 Techniques to enhance the DE at backoff power.	101
80 Single input Doherty PA diagram.	102
81 Simplified Doherty PA diagram.	103
82 Dual-input Doherty PA.	104
83 Simplified scheme of Chireix PA.	105
84 Hybrid Doherty-Chireix outphasing PA squeme	105
85 Hybrid Doherty Outphasing PA Liang <i>et al.</i> (2019b) used to demonstrate the multi-channel application of the VSNA.	106
86 Flowchart for CW measurements.	108
87 Drain efficiency (%) versus P_{out} (dBm) and outphasing angle ($^{\circ}$).	108
88 Optimal simulated and measured outphasing angles θ ($^{\circ}$) versus P_{out} (dBm) at ω_0	110
89 Optimal measured DC Power (W) versus P_{out} (dBm) for the main (red circles) and peaking (blue square) PAs at ω_0	110
90 Drain efficiency (%) and dissipated power (%) versus P_{out} (dBm) within the 120 MHz frequency span of this HD-OPA.	111
91 Gain (dB) versus P_{out} (dBm) for different frequencies.	112
92 Gain (dB) versus P_{out} (dBm) and Outphasing angle θ ($^{\circ}$).	112
93 PAE % versus P_{out} (dBm) and outphasing angle ($^{\circ}$).	113
94 Flowchart describing the error correction applied in post-processing to the raw data to obtain the calibrated dynamic behavior of the OPA modulated signals.	114
95 HD-OPA Dynamic Behavior with an OFDM 10 MHz signal.	115
96 HD-OPA Dynamic Behavior with an OFDM 20 MHz signal.	116
97 Simplified diagram of the integration of the DPD with the OPA LUT.	117

List of figures (continue)

Figure	Page
98 AM-AM and AM-PM of the HD-OPA before and after the DPD, for a 10 MHz BW signal.	117
99 Output spectra observed in (a) Matlab, (b) SA-PNA-X for a 10 MHz BW signal.	118
100 AM-AM and AM-PM of the HD-OPA before and after the DPD, for a 20 MHz BW signal.	118
101 Output Spectrum observed in the SA-PNA-X for a 20 MHz BW signal.	118
102 IQ constellations for a 16 QAM OFDM signal of 10 MHz BW.	119
103 Adjacent Channel Leakage Ratio	120
104 Representation of the DUT in a fixture with the error boxes of each port. . .	130
105 Two lines of different lengths.	132
106 Reflected loads connected to each reference port.	134
107 Scheme of the DUT output.	136
108 Scheme of the measurement setup when the load tuner is connected. . . .	137
109 Through connection to measure the output reflection coefficients at DUT reference planes.	138

List of tables

Table		Page
1	12-term error model for 2-port	12
2	Output voltage amplitudes and their respective phases ϕ , which give $P_{o_{avg}}/\rho$	39
3	Output current amplitudes and their respective phases ϕ , which give $P_{o_{avg}}/\rho$	40
4	Input/Output power and optimum impedances.	77
5	Figures of Merit for the OFDM Measurements.	85
6	EVM values in % and dB obtained for an OFDM signal of 100 MHz with 16 QAM at each step of the calibration	93
7	EVM values in % and dB obtained for an OFDM signal of 500 MHz with 64 QAM at each step of the calibration	95
8	Characteristics of the OFDM signals measured with VSNA and VSA . .	99
9	Average EVM and SNR obtained with the VSNA and VSA	99
10	LUT of the HD-OPA for maximum efficiency.	109
11	Figures of merit obtained with a 10 MHz OFDM signal.	119
12	Figures of merit obtained with a 20 MHz OFDM signal.	119

List of abbreviations

ACLR	Adjacent Channel Leakage Ratio
ACPR	Adjacent Channel Power Ratio
ADC	Analogue to Digital Converter
ADS	Advance Design System
AM-AM	Amplitude to Amplitude Modulation
AM-PM	Amplitude to Phase distortion
AWG	Arbitrary Waveform Generator
BER	Bit Error Rate
BPSK	Binary Phase Shift Keying
C/I	Carrier to Intermodulation
CW	Continuous Wave
DAC	Digital to Analog Converter
DDS	Direct Digital synthesizer
DE	Drain Efficiency
DMM	Digital Multimeter
DPD	Digital pre-distortion
DR	Dynamic range
DSP	Digital Signal Processor
DUC	Digital-Upconverter
DUT	Device Under Test
EMT	Electromechanical Tuner
ETS	Electronic Tuner
EVM	Error Vector Magnitude
FET	Field-Effect Transistors
FFT	Fast Fourier Transform
FIR	Finite duration Impulse Response
FPGA	Field Programmable Gate Array
GaN	Gallium Nitrate
GRC	GNU Radio Companion
GSM	Global System for Mobile Communica- tions
HD-OPA	Hybrid Doherty Outphasing PA
HEMT	High Electron Mobility Transistor
IFFT	Inverse Fast Fourier Transform
IMD	Intermodulation Order
IMN	Input Matching Network
ITU	International Telecommunication Union
LFTX	Low Frequency Transmitter
LINC	Linear amplification using Nonlinear Components
LMBA	Load Modulated Balanced Amplifier
LO	Local Oscillator
LP	Load-Pull
LRL	Line-Reflect-Line
LRM	Line-Reflect-Match
LRRM	Line-Reflect-Reflect-Match
LSNA	Large-Signal Network Analyzer
LTE	Long Term Evolution
LUT	Look-Up-Table

MESFET	Metal Semiconductor Field-Effect Transistors
MPT	Multi-Purpose Tuner
MQAM	M-ary Quadrature Amplitude Modulation
MTA	Microwave Transition Analyzer
NCO	Numerically Controlled Oscillator
NMSE	Normalized Mean Square Error
NVNA	Nonlinear Vector Network Analyzer
OFDM	Orthogonal Frequency-division Multiplexing
OMN	Output Matching Network
OPA	Outphasing Power Amplifier
OS	Operation system
PA	Power Amplifier
PAE	Power Added Efficiency
PAPR	Peak to Average Power Ratio
PDF	Probability Density Function
QAM	Quadrature Amplitude Modulation
QPSK	Quadrature Phase Shift Keying
QSOLT	Quick-SOLT
RBW	Resolution Bandwidth
RFPA	Radio Frequency Power Amplifier
RMS	Root Mean Square
SA	Spectrum Analyzer
SNR	Signal to Noise Ratio
SOLR	Short-Open-Load-Reciprocal
SOLT	Short-Open-Load-Thru
SP	Source-Pull
TRL	Thru-Reflect-Line
TRM	Thru-Reflect-Match
USMT	Unequal Space Multitone
USR	Universal Software Radio Peripheral
VNA	Vector Network Analyzer
VSA	Vector Signal Analyzer
VSG	Vector Signal Generator

Chapter 1. Introduction

This chapter will give a brief introduction to the study object of this dissertation. Firstly the main motivations that drove this work will be presented. Then a review of the state-of-art and the objectives of this research will be discussed.

1.1 Motivation

The rapid growth of wireless communication services has led to the development of new standards that provide a higher transmission rate in a given bandwidth, which brings a constant update of the hardware. These systems demand better power consumption, efficiency, linearity, and high bandwidth (> 100 MHz for 5G networks). Therefore, it is necessary to consider them in designing the components that are part of the system. The devices that contribute the most to the deterioration of the requirements mentioned above are those whose behavior is nonlinear. The most critical element in a communication system is the Power Amplifier (PA). It is the one with the highest consumption, power dissipation, and it causes more significant interference in adjacent channels, reasons why their design is essential. The PAs provide greater efficiency when operating in their saturation zone. They exhibit nonlinear behavior, generating frequency components in the output signal that were not in the input signal, increasing the Adjacent Channel Power Ratio (ACPR). Thus, a design compromise arises between the efficiency and linearity of a PA. To obtain a linear, efficient, and broadband PA, first, it is first designed to be efficient and broadband, which is already a significant challenge. Then it is linearized by using a Digital pre-distortion (DPD). As greater bandwidths are required, the complexity and current consumption of the DPD increases (this high current consumption harms the overall efficiency of the amplifier).

The PA design consists of finding the optimal source and output loads at the fundamental frequency that minimize the input reflections and maximize the output power (P_{OUT}) of the transistor while sustaining a reasonable, efficiency and linearity. It also determines the harmonic terminations that improves the PA Drain Efficiency (DE) (η_D). The PA design process defines thus the optimal source and load impedance terminations at the fundamental and harmonic frequencies which must be provided by the PA input (IMN) and output (OMN) matching networks, respectively.

The Source-Pull (SP) and Load-Pull (LP) are the techniques that allow exploring the nonlinear behavior of the Device Under Test (DUT), as different set of controlled input and output loads are presented to it. These measurements are done at several frequencies and biases to find the condition where the PA operation is optimum. This is commonly evaluated based on metrics such as; P_{OUT} , η_D , Power Added Efficiency (PAE), and the spectral regrowth that arise from the device nonlinearities and are characterized by the ACPR. Harmonic LP technique is used for optimizing the impedances at harmonic frequencies.

The vast majority of the PA designers use software tools, like Advance Design System (ADS), that include the compact nonlinear transistor models (this is the PA core), source and load pulls capabilities, an Harmonic balance simulator, and others functions, that together facilitate the design of a PA.

The design's success depends on the accuracy of the model, whose extraction is based on the transistor measurements with small and large signals. Still, due to imperfections during the manufacturing process, the behavior of the components in the same batch can be slightly different. Hence, the model is an approximation of the actual behavior of the device used. The SP and LP techniques are used in the transistor model extraction, the PA design, and the performance verification of the built PA. In addition, fine-tuning of the IMN and OMN can take place to optimize the PA response.

1.2 State of the art

As mentioned before, SP and LP are crucial techniques used in the transistor model extraction and PA design. Accordingly to the device nature used to generate the impedance, it can be grouped into three main categories: passive, active (a signal is injected into the reference plane of the DUT), and hybrid systems (is a combination of the two mentioned before). They can also be grouped into different subcategories, as shown in Figure1. The most notable disadvantage of the passive LP system is the losses presented in the path, making it impossible to reach higher reflection coefficients (Γ) values, as some PA designs require. The active LP solves this problem by injecting an amplified signal, a sample of the DUT output signal (closed-loop configuration), or an independently signal (open-loop configuration) combined with the one

coming from the DUT conforming to an impedance. The closed-loop configuration converges faster than the open-loop one, but for specific values, the transistor can oscillate.

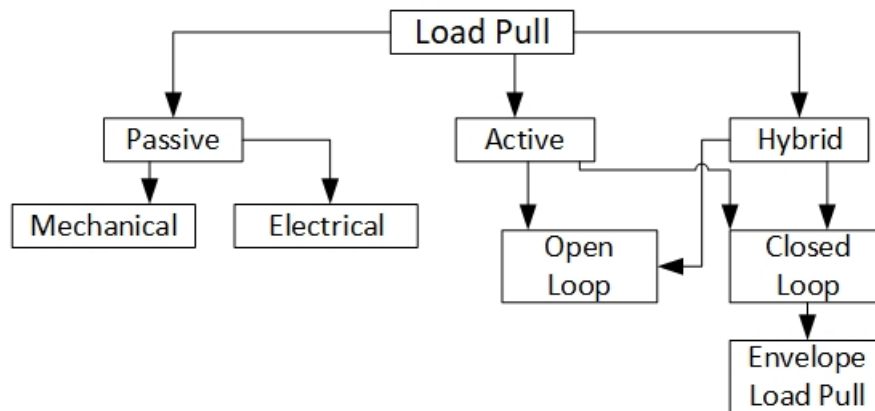


Figure 1. LP subcategories.

To inspect the impact of the harmonic impedance terminations in the PA behavior, harmonic LP systems are used. Some configurations to generate them are summarized below:

- Resonant Stub: consists of an open stub with a quarter wavelength (at the harmonic frequency) connected to the central conductor by sliding contact. The movement of it along the conductor can change the reflection coefficient phase observed by the DUT at the harmonic frequency. It was the first solution to generate harmonic tuners presented in 2000 under patent number 6297649.
- Multiple passive wideband tuners, each one working at a different frequency and joined using a multiplexer; thereby, each tuner has limited bandwidth.
- Wideband passive tuners connected in a cascade, internal or external, here the number of probes determines the harmonics that can be handle.
- Multiple sources, each operating at different frequencies (fundamental and harmonic), combined with a multiplexer and placed at the output reference of the DUT. A driver PA is used to achieve a high reflection coefficient, as is the case for harmonics, where an open or short termination is often required.
- Hybrid harmonic LP which is a combination of passive and active LP techniques.

Due to the importance of the LP systems, there are plenty of publications about it. Simpson (2009) and Focus (2007) compare several harmonic LP techniques. Tsironis (2012) compares purely active and hybrid LP systems, concluding that active closed-loop systems are not an acceptable solution, either with or without the use of passive pre-tuning tuners. On the other hand, open-loop active injection LP systems require additional synthesizers and high power amplifiers, making the system more expensive. The active hybrid open-loop injection system using broadband tuners generates hanging harmonic loads and does not provide optimal harmonic impedance and power injection. Only open-loop hybrid active injection with harmonic tuners offers a good compromise. In Hosein and Beauchamp (2013) a hybrid LP measurement system is presented, which uses multi-purpose mechanical tuners and signal injection by means of generators at the fundamental frequency and in the first two harmonics, generating impedances as close to the edge of Smith's chart as required. The tuner is previously moved as close as possible to this value to generate a particular reflection coefficient. A finer adjustment in magnitude and phase is made using the signal generator.

In Choi *et al.* (2013) a time domain measurement system with hybrid harmonic LP is proposed, which allows the identification of the optimal harmonic terminations necessary to obtain the maximum efficiency. F.L. Ogboi, P.J. Tasker (2013) proposed a calibrated multitone LP system to optimize the linearity of the device by varying the baseband impedance presented to the transistor.

Multitone signals are of great interest for intermodulation measurements in active devices. In Farsi *et al.* (2014), a 7-tone signal is obtained to prevent the third and fifth order of intermodulation, and El Mahalawy *et al.* (2014) used a harmonic LP to improve the PAE of a 0.25 μm Gallium Nitrate (GaN) transistor operating at 10 GHz; an improvement in 11 % is exhibited when the optimum harmonic terminations are reached. In Tao *et al.* (2015) presents a design method for high efficiency power amplifiers by performing low frequency measurements with active harmonic LP, achieving an efficiency of 77 %, and Marchetti *et al.* (2015) measured AlGaN / GaN transistors using a harmonic LP system with a mixed-signal. The main advantage of this configuration is the measurement speed. One year later, Laurent *et al.* (2016) proposed a multitone load measurement system using an Arbitrary Waveform Generator (AWG) and a Large-Signal Network Analyzer (LSNA) as a receiver. At the same time, Kahil

et al. (2016) generated tones through an explicit algorithm that is described in Teysier *et al.* (2014). The proposed drive signal ensures that the intermodulation products of the DUT do not overlap. The later system represents an innovative testbed with multi-tone LP (MTLP) for characterizing the linearity of power transistors. The configuration allows emulating a complete linearity measurement system without requiring the modulation and demodulation of complex signals, making it very useful for wafer transistor measurement. Furthermore, the measurement time for device characterization with this technique is shorter than the standard one. In the design of multioctave power amplifiers ($N_{octaves} = 2^N * f$), certain harmonics are within the operating band, so one must carefully perform LP techniques within and out of the band. A new methodology for their design is presented in Taghavi *et al.* (2016), using harmonic sequential characterization. If the bandwidth of interest ($BW = f_{stop} - f_{start}$) is greater than one octave, then $f_{stop} > 2 * f_{start}$, the lower frequency range (*FLIB*) and higher (*FHIB*) within the band are defined in the equations (1) and (2):

$$f_{start} < FLIB < \frac{f_{stop}}{2} \quad (1)$$

$$\frac{f_{stop}}{2} < FHIB < f_{stop} \quad (2)$$

It can be seen from equation (1) that the second harmonic is within the band of interest, while for the upper-frequency range, the harmonics are more significant than f_{stop} and are outside the band of interest. In LP characterization, harmonic impedances are usually selected to obtain the optimal performance in power and efficiency. However, they cannot characterize the band's lower range in multioctave designs until the optimal impedances are identified. In Taghavi *et al.* (2016) the algorithm for sequential LP is proposed. It is concluded that for the study of harmonics in the PA working band, better performance is obtained using the harmonic sequential technique than with the conventional LP, improving the drain efficiency of a PA using GaN High Electron Mobility Transistor (HEMT), CGH40010F, manufactured by Cree Inc. by 10 %.

1.3 General Objective

The objectives of this work are the large signal characterization of the GaN HEMT power transistors and PAs by using real-time LP systems with single and multitone

signals, and the development of a testbed to extract the static and dynamic behavior and linearization of multiple-input PAs using the new Spectrum Analyzer (SA) option of the PNA-X Vector Network Analyzer (VNA).

1.3.1 Specific objectives

1. Proposal for a fully automated testbed for real-time LP measurements using multitone signals.
 - 1.1 Study the state of the art and the different load pull system configurations.
 - 1.2 Study the different calibration techniques used to characterize DUT in a fixture.
 - 1.3 Configuration of the measurement setup to work remotely and create the protection required to work with high power.
2. Proposal of a new testbed for the static, dynamic characterization and linearization of multiple input devices with modulated signals.
 - 2.1 Explore the functionality of the SA option of the VNA to perform the static and the dynamic characterization of single input single output nonlinear devices.
 - 2.2 Propose a correction algorithm to demodulate the signal and compute the in-band distortion, using the traditional calculation of the EVM in the IQ-constellation domain.
 - 2.3 Create the functions in Matlab to configure and communicate with the instruments. Generate the waveforms, download them to the AWG and capture the measurements from the VNA.
 - 2.4 Demonstrate the wideband capability of the setup.
 - 2.5 Compare the functionality of the new testbed proposed with a commercial Vector Signal Analyzer.
 - 2.6 Extract the static and the dynamic behaviors and the linearization of a multiple input single output nonlinear device.

Chapter 2. Vector Network Analyzer (VNA)

This chapter will cover different error models used to represent the systematic errors present in one-port and two-port VNA; also, the most used calibration methods to remove them from the DUT measurements will be explained.

2.1 Introduction

The characterization of power transistors using small and large signals to obtain the scattering parameters (S-parameters) and the hot S-parameters are required to guarantee a good model extraction that represents the DUT behavior. Which will allows predicting in advance its response under Continuous Wave (CW) and modulated signals. The most used instrument to perform these measurements is the VNA, which measure the incident and reflected waveform ratios at the input and output of the DUT. Reflections occur when the impedance of the input or output networks of a DUT does not match the impedance of the measurement system. The reflection coefficient (Γ) defined in equation (3) is a measure of how much voltage is reflected from the DUT. Its magnitude value $|\Gamma|$ varies from 0 to 1, where $|\Gamma| = 0$ implies a perfect impedance match (not reflections) and $|\Gamma| = 1$ a full mismatch (the whole transmitted signal reflects from the DUT into the source),

$$\Gamma = \frac{Z_i - Z_o}{Z_i + Z_o}. \quad (3)$$

Equation (3) Z_i is the DUT impedance and Z_o the characteristic impedance of the measurement system.

2.2 Scattering matrix definition

Figure 2 shows a two-port DUT, fed with a generator with characteristic impedance Z_o , and loaded with Z_o . V_1 , I_1 , and V_2 , I_2 , are the input and output voltages and currents of the DUT, respectively, while (a_1, a_2) and (b_1, b_2) are the incident and reflected waveforms at DUT ports. They are defined in equation (4) and (5), where V_i and I_i are the voltage and current at port i , respectively,

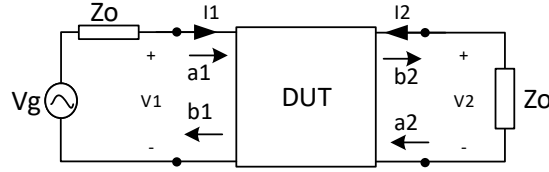
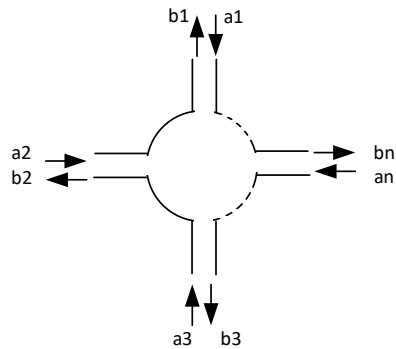


Figure 2. DUT of two-port.

$$a_i = \frac{1}{2} \left(\frac{V_i}{\sqrt{Z_o}} + \sqrt{Z_o} \times I_i \right), \quad (4)$$

$$b_i = \frac{1}{2} \left(\frac{V_i}{\sqrt{Z_o}} - \sqrt{Z_o} \times I_i \right). \quad (5)$$

If $a_{1,2}$ and $b_{1,2}$ are fully measured (amplitude and phase) across a band of interest, the DUT performance can be determined. The S-parameters (elements of the scattering matrix), defined in equation 6, are used to describe the linear performance of a DUT, depending on the incident and reflected waveforms measured using small signal excitations. The elements of the matrix are calculated at each port, by making the independent variables (a_i) of the remaining ports equal to zero ($S_{ij} = \frac{b_i}{a_j}, | a_k = 0, k = 1 : n, k \neq j$).



$$\begin{bmatrix} b_1 \\ b_2 \\ \cdot \\ b_n \end{bmatrix} = \begin{bmatrix} S_{11} & \dots & S_{1n} \\ S_{21} & \dots & S_{2n} \\ \cdot & \cdot & \cdot \\ S_{n1} & \dots & S_{nn} \end{bmatrix} \begin{bmatrix} a_1 \\ a_2 \\ \cdot \\ a_n \end{bmatrix} \quad (6)$$

2.3 Vector Network Analyzer errors and models

Figure 3 shows fundamental blocks of a two-ports VNA (four receivers). To measure the S-parameter of a two-ports DUT, the source is first connected to the input port of the DUT while the output port is loaded with Z_o ; Therefore, the S_{11} and S_{21} parameters

are computed in the forward direction, then the position of the switch is changed to drive the source signal to the output port. At the same time, the input is loaded with Z_0 , allowing to calculate S_{22} and S_{12} , in the reverse direction, in accordance with the S-parameter definition. A four-port VNA adds another source with a switch and a 50 ohm load to measure the scattering elements of a 4×4 matrix. The approach explained before is extended to fulfill four-ports measurements.

The directional couplers in Figure 3, are needed to sample the incident and reflected Radio frequency (RF) waveform in both forward and reverse direction and send them to the Receiver and Detector part of the VNA, where mixers down-convert the RF signals to a fixed low frequency (IF): to accomplish it the Local Oscillator (LO) source is tuned to $RF+IF$ frequency. The next step the signal is to filter and digitize using Analogue to Digital Converter (ADC) and finally, they are processed in the Digital Signal Processor (DSP) and the values shown in the VNA display.

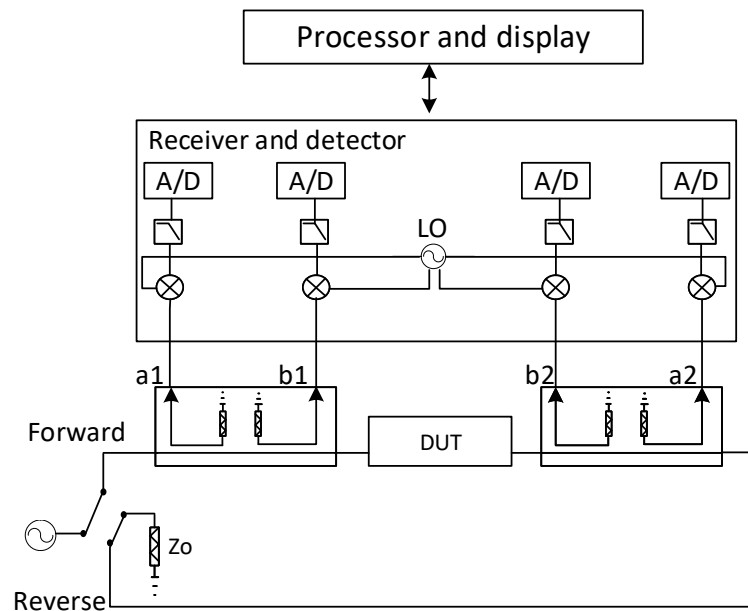


Figure 3. Two-port VNA diagram.

Several errors of different nature present in the VNA will be transferred to the DUT measurements if they are not previously removed. They can be grouped as:

- **Systematic errors:** They originate from the nonlinearities of the components that are part of the instrument, such as directional couplers, dividers, mixers, switches, and others. They are repetitive and stable and can be minimized using

the measurements of known elements (calibration standards).

- **Random errors:** are due to unknown effects of an arbitrary nature. They can not be measured as they are not repetitive.
- **Environmental errors:** they are a result of environmental changes on time, like the temperature, humidity, pressure, and others. It is possible to reduce their effects with appropriate control of these physical variables where the measurements are done.
- **Residual errors:** are caused by of imperfection in the calibration: standards are used to remove the systematic errors and drift, lack of stability, and repeatability after the error correction.

To develop an error correction procedure, it is necessary; first, that a VNA model be constructed that considers the systematic errors, which, after been calculated, will be removed from the measured waveforms, to obtain the actual behavior of the DUT.

2.3.1 3-term error model

Figure 4 (a) shows simplified signal flow diagram, used to one-port calibration, where the 3-term errors are:

1. the directivity error (e_{00}) is caused mainly by the coupler leakage or couple directivity, which increases if cables and connectors are placed between the coupler and the DUT,
2. the reflection ($e_{10}e_{01}$) error originates from an imperfect reflectometer, mixer tracking and the cables length imbalance between the ports, and
3. the source match (e_{11}) error represents the mismatch between the coupler, cables, and connectors in the measurement port.

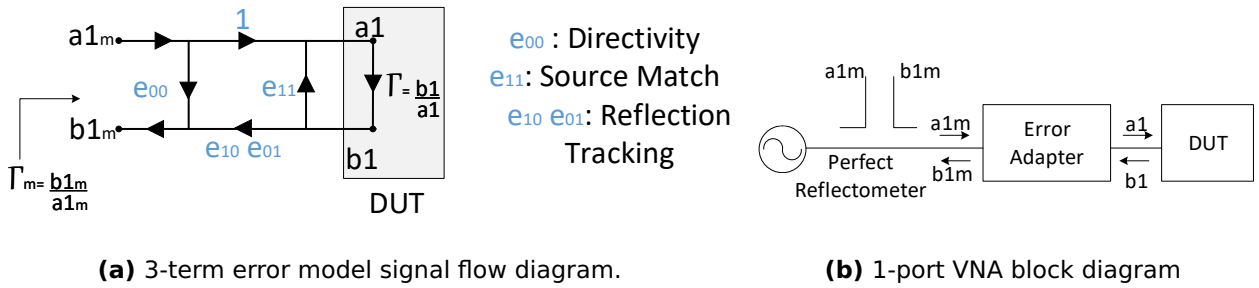


Figure 4. 1-port VNA configuration.

Figure 4 (b) shows a simplified 1-port VNA represented with a perfect reflectometer and an error adapter between it and the DUT. This configuration removes the error from the measured waveforms (a_{1m}) and (b_{1m}), to correct the waveforms at the DUT reference plane (a_1, b_1).

2.3.2 12-term error model

The two-ports VNA can be represented using a 12 error-terms model, as shown in Figure 3. To obtain the S-parameters of a two-port DUT, it will be necessary, first, to introduce a signal at port-1 ($a_{1m}^F \neq 0$), while the port-2 is loaded with a Z_o impedance ($a_{2m}^R = 0$). These measurements are done in the forward direction (F), as shown in 5 (a),. Then the measurements in reverse direction (R) are done by making ($a_{1m}^F = 0$) and ($a_{2m}^R \neq 0$), 5 (b).

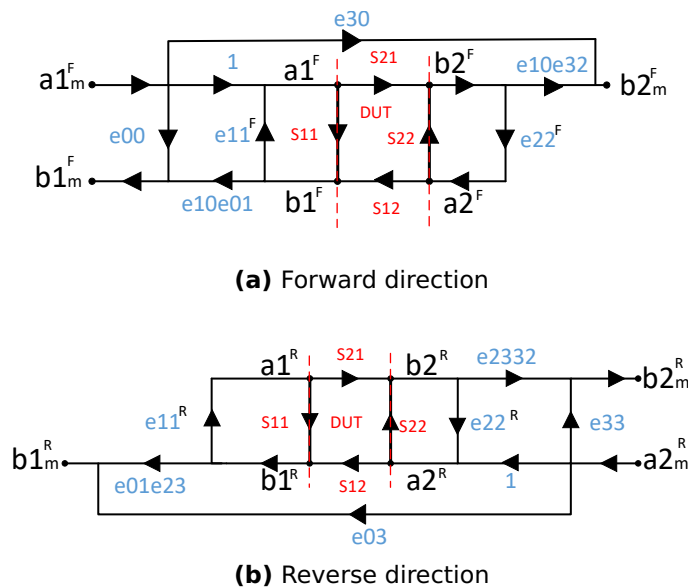


Figure 5. 12-term error model signal flow diagram.

As the one-port model, the two-port model can be represented as a perfect reflectometer with an error adapter for the forward and reverse directions, as observed in Figure 6 (a), (b), respectively. The error adapter models (F) and (R) are shown in Figures 5 (a) and (b). Table 1 summarizes the error-terms present in both directions with **Isolation** equal to e_{30} and e_{03} .

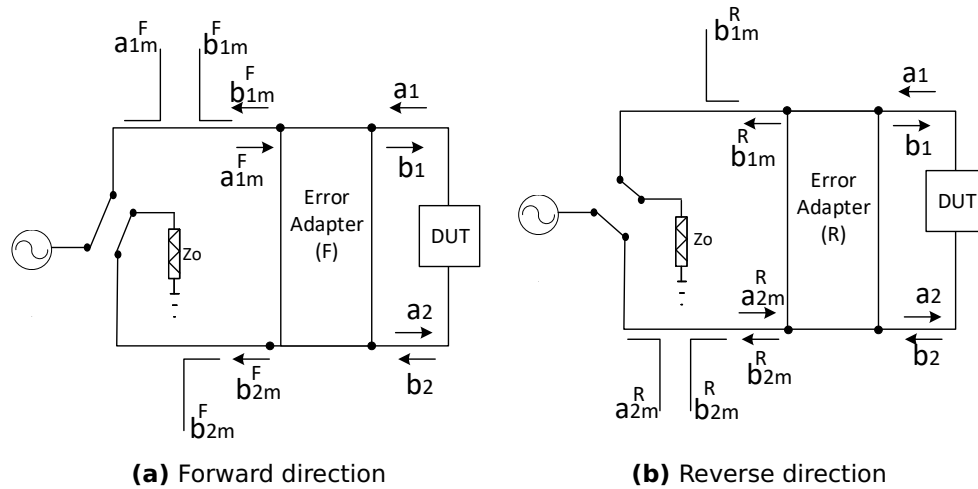


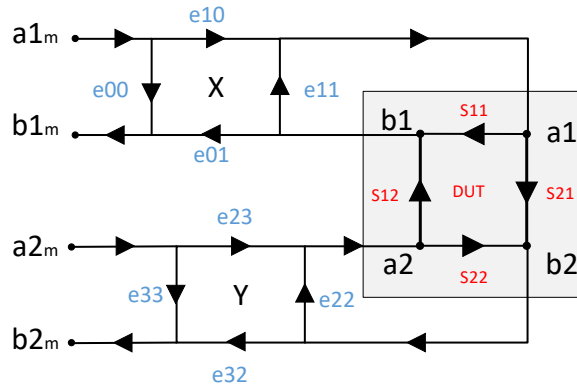
Figure 6. 2-Port VNA diagram with 12-term error.

Table 1. 12-term error model for 2-port

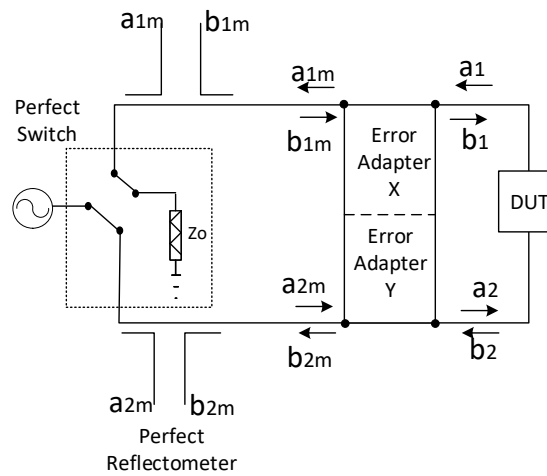
	Port 1	Port 2
Port1	e_{00} (Directivity) e_{11}^F (Source match) $e_{01}e_{10}$ (Reflection Tracking)	$e_{10}e_{32}$ (Transmission tracking) e_{22}^F (Load match)
Port2	$e_{01}e_{23}$ (Transmission Tracking) e_{11}^R (Load Match)	e_{22}^R (Source Match) e_{33} (Directivity) $e_{23}e_{32}$ (Reflection Tracking)

2.3.3 8-term error model

Figure 7 shows the 8-term error model, suitable for 2-port measurements, which is obtained from the 12-error term, P. Dunsmore (2012), assuming that the isolation terms are zero ($e_{30} = 0$, $e_{03} = 0$) and that the switch is perfect. Therefore, it does not introduce any change in the port match of the VNA when it switches from the forward direction to reverse or vice-versa since it assumes that $e_{11}^R = 0$, $e_{22}^F = 0$. Figure 7 (b) shows the VNA diagram represented by a perfect reflectometer, a perfect switch, and two error box adapters (X and Y) for ports one and two respectively.



(a) 8-term error signal flow diagram



(b) 2-port VNA diagram

Figure 7. 2-port VNA configuration with 8-term error

2.3.4 Switch error correction

As explained in section 2.2, the DUT scattering parameters are determined by introducing a signal in one of the DUT ports while loading the rest of them with Z_o . This process is repeated for all the ports, measuring each time the ratio $\left(\frac{b_i}{a_j}\right)$, with $i, j = 1 : Nports$. When the VNA sources and the load Z_o are not perfectly matched, each time the switch changes its position, the S-parameters will present errors.

To obtain the switch errors and remove their effects from the DUT measurements, the following models shown in Figure 8 (a) and (b) are considered for the forward and reverse direction. These models feature a perfect reflectometer, an imperfect switch, and an error adapter box. For the ideal case where the source and Z_o are matched,

it is appreciable from Figures 8 (a) and (b), that $a_3 = 0$ and $a'_o = 0$ in the forward and reverse directions.

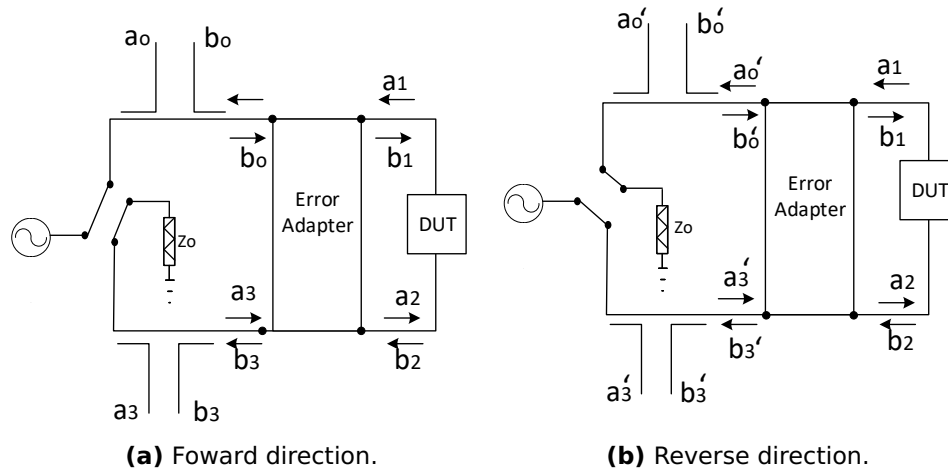


Figure 8. VNA diagram for the switch error corrections.

The equations (7) and (8), represent the S-parameters measured with a non-calibrated VNA in forward and reverse directions, respectively,

$$\begin{bmatrix} b_o \\ b_3 \end{bmatrix} = \begin{bmatrix} S_{11m} & S_{12m} \\ S_{21m} & S_{22m} \end{bmatrix} \begin{bmatrix} a_o \\ a_3 \end{bmatrix}, \quad (7)$$

$$\begin{bmatrix} b'_o \\ b'_3 \end{bmatrix} = \begin{bmatrix} S_{11m} & S_{12m} \\ S_{21m} & S_{22m} \end{bmatrix} \begin{bmatrix} a'_o \\ a'_3 \end{bmatrix}. \quad (8)$$

The S_{ij} are unique, which means that they have the same values measured in forward and reverse direction. As a result of equations (7) and (8), equation (9) can be obtained:

$$\begin{bmatrix} b_o & b'_o \\ b_3 & b'_3 \end{bmatrix} = \begin{bmatrix} S_{11m} & S_{12m} \\ S_{21m} & S_{22m} \end{bmatrix} \begin{bmatrix} a_o & a'_o \\ a_3 & a'_3 \end{bmatrix}. \quad (9)$$

The raw S-parameters, measured with the uncalibrated VNA are,

$$\begin{aligned}
 B &= S A, \\
 S &= B A^{-1}, \\
 \begin{bmatrix} S_{11m} & S_{12m} \\ S_{21m} & S_{22m} \end{bmatrix} &= \begin{bmatrix} \frac{b_0 - b'_0 \frac{a_3}{a_0}}{d} & \frac{b'_0 - b_0 \frac{a'_0}{a_3}}{d} \\ \frac{b_3 - b'_3 \frac{a_3}{a_0}}{d} & \frac{b'_3 - b_3 \frac{a'_0}{a_3}}{d} \end{bmatrix}, \tag{10}
 \end{aligned}$$

$$\text{with } d = 1 - \frac{a'_0 a_3}{a_3 a_0}.$$

Considering the raw measured S-parameters before removing the switch errors : $S_{11} = \frac{b_0}{a_0}$, $S_{21} = \frac{b_3}{a_0}$, $S_{11} = \frac{b_0}{a_0}$, $S_{12} = \frac{b'_0}{a_3}$, $S_{22} = \frac{b'_3}{a_3}$, equation 10 can be rewritten as:

$$\begin{bmatrix} S_{11m} & S_{12m} \\ S_{21m} & S_{22m} \end{bmatrix} = \begin{bmatrix} \frac{S_{11} - S_{12} \frac{a_3}{a_0}}{d} & \frac{S_{12} - S_{11} \frac{a'_0}{a_3}}{d} \\ \frac{S_{21} - S_{22} \frac{a_3}{a_0}}{d} & \frac{S_{22} - S_{21} \frac{a'_0}{a_3}}{d} \end{bmatrix}. \tag{11}$$

In equation (11), S_{ijm} are the S-parameters of the DUT after applying the switch error correction. Six measurements are required to calculate them (assuming that a 2-port device is measured): $\frac{a_3}{a_0}$ and $\frac{a'_0}{a_3}$ which are acquired in forward and reverse directions, respectively, and the four raw S-parameters of the DUT.

Another way to rewrite equation (11) is shown in (12), where $\Gamma_1 = \frac{a'_0}{b'_0}$ and $\Gamma_2 = \frac{a_3}{b_3}$ are acquired in reverse and forward directions, respectively. The advantage of (12) is that Γ_1 and Γ_2 , are independent of the DUT, therefore they can be measured just one time as long as the switch does not change its behavior, reducing the six required measurements in equation (11) to four,

$$\begin{bmatrix} S_{11m} & S_{12m} \\ S_{21m} & S_{22m} \end{bmatrix} = \begin{bmatrix} \frac{S_{11} - S_{12} S_{21} \Gamma_2}{D} & \frac{S_{12} - S_{12} S_{11} \Gamma_1}{D} \\ \frac{S_{21} - S_{22} S_{21} \Gamma_2}{D} & \frac{S_{22} - S_{21} S_{12} \Gamma_1}{D} \end{bmatrix}, \tag{12}$$

with $D = 1 - S_{12} S_{21} \Gamma_1 \Gamma_2$.

Figures 9 (a) and (b) compare the S_{11} and S_{22} parameters calculated, including

the switch error correction (blue line) with their respective measurements done with a calibrated Vector Signal Analyzer (VSA) (red line). From Figures 9 (a) and (b) it is appreciable that S_{11} and S_{22} magnitudes are smoother after removing the switch errors.

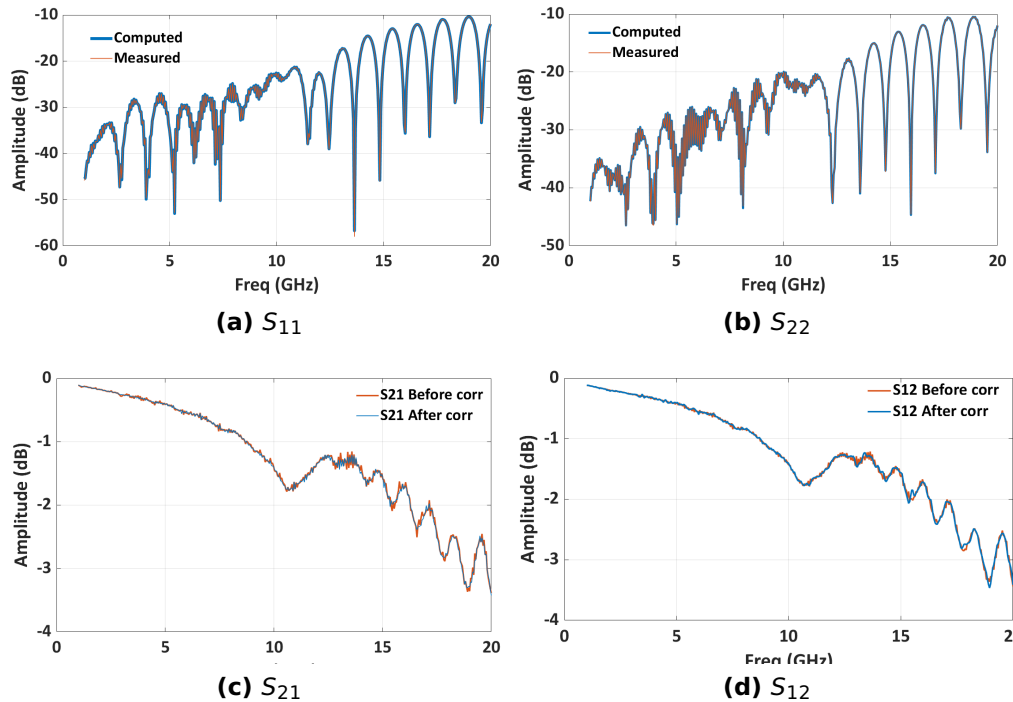


Figure 9. S-parameter magnitudes of a 6.8 cm line after removing the switch errors.

Figures 9 (c) and (d) show the magnitude of S_{21} and S_{12} of the DUT, before (red) and after (blue) the switch error correction. An appreciable noise reduction is observed in both parameters after the correction. The phase of S_{21} and S_{12} are omitted because the switch error corrections do not have any effect on their behavior.

2.4 Calibration techniques

Calibration is the procedure that removes all possible errors, allowing the placement of the reference planes at the DUT input and output. Several techniques to compute the VNA errors are available in the literature. In this section, some calibration techniques will be explained.

2.4.1 One-port calibration

The one-port calibration will be described considering the three-term error model of Figure 4 (a). Applying Mason rules to the flow graph of Figure 7 (a), the measured reflection coefficient (Γ_m) is obtained in equation (13). It depends on the VNA errors and the actual reflection coefficient (Γ). A linear system of three equations with three variables, is obtained from equation (13),

$$\Gamma_m = e_{00} + \frac{e_{10}e_{01}\Gamma}{1 - e_{11}\Gamma}. \quad (13)$$

The error values (e_{00} , e_{11} , $e_{10}e_{01}$), are commonly found using an open, short, and load. In the case where the reflection coefficients of the standards used are ideal, where for the open $\Gamma_o^{Ideal-Open} = 1$, the short $\Gamma_s^{Ideal-Short} = -1$, and the load $\Gamma_l^{Ideal-Load} = 0$. The measured Γ for each standard can be written as a function of the error-terms as follows:

$$\begin{aligned} \Gamma_m^{Ideal-Load} &= e_{00} + \frac{e_{10}e_{01}(0)}{1 - e_{11}(0)}, \\ \Gamma_m^{Ideal-Short} &= e_{00} + \frac{e_{10}e_{01}(-1)}{1 - e_{11}(-1)}, \\ \Gamma_m^{Ideal-Open} &= e_{00} + \frac{e_{10}e_{01}(1)}{1 - e_{11}(1)}. \end{aligned} \quad (14)$$

From 14 the 1-port error-terms are calculated as,

$$\begin{aligned} e_{00} &= \Gamma_m^{Ideal-Load}, \\ e_{11} &= \frac{\Gamma_m^{Ideal-Open} + \Gamma_m^{Ideal-Short} - 2e_{00}}{\Gamma_m^{Ideal-Open} - \Gamma_m^{Ideal-Short}}, \\ e_{10}e_{01} &= -\frac{2(\Gamma_m^{Ideal-Open} - e_{00})(\Gamma_m^{Ideal-Short} - e_{00})}{\Gamma_m^{Ideal-Open} - \Gamma_m^{Ideal-Short}}. \end{aligned} \quad (15)$$

Three well known non-ideal standards are considered to compute the error-terms, and their models are preloaded in the VNA firmware. The generalized solution for the error-

terms is,

$$\begin{bmatrix} e_{00} \\ -\Delta_e \\ e_{11} \end{bmatrix} = \begin{bmatrix} 1 & \Gamma_{AO} & \Gamma_{AO}\Gamma_{MO} \\ 1 & \Gamma_{AS} & \Gamma_{AS}\Gamma_{MS} \\ 1 & \Gamma_{AL} & \Gamma_{AL}\Gamma_{ML} \end{bmatrix}^{-1} \begin{bmatrix} \Gamma_{MO} \\ \Gamma_{MS} \\ \Gamma_{ML} \end{bmatrix}, \quad (16)$$

$$\Delta_e = e_{00}e_{11} - (e_{10}e_{01}).$$

where Γ_{AO} , Γ_{AS} , Γ_{AL} , are the actual reflection coefficients of the standards, and Γ_{MO} , Γ_{MS} , Γ_{ML} , are their respective raw measurements, which can take any value. The labels *O*, *S* and *L* denote *open*, *short* and *load*.

Knowing the 3-term error of 1-port and measuring the raw reflection coefficient (Γ_m) of a one-port DUT, the actual Γ is obtained using equation (17),

$$\Gamma = \frac{\Gamma_m - e_{00}}{e_{11}\Gamma_m - \Delta_e}. \quad (17)$$

2.4.1.1 Reflection standard models

The standard reflective model is represented by lumped circuit elements (capacitors and inductors) and distributed elements representing offset delay and loss. Figure 10 represents the model for reflection standard (*open*, *short* and *load*, or arbitrary impedance), described in the Agilent Application Note 8510-5B.

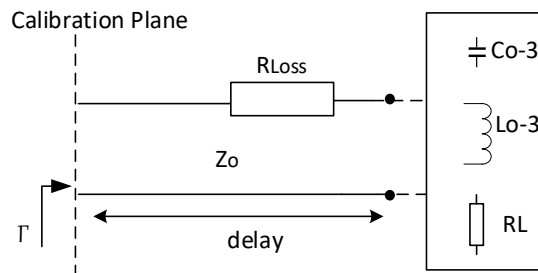


Figure 10. Model for reflection standard.

The *open* and *short* standards are modeled using a third order polynomial, where C_0-C_3 , L_0-L_3 are the coefficients used to obtain the phase shift caused by the fringing

capacitance, and the residual inductance, respectively, as a function of the frequency. The terminal impedance (RL) is only specified for an arbitrary impedance standard. An offset delay occurs if the reflection standard used has an electrical length relative to the calibration plane. The delay is calculated in equation (18), where l is the physical offset length of the standard in meter, ϵ_r is the relative permittivity of the material used inside the standard, and $c = 3 \times 10^{10} \text{ cm/s}$ is the speed of light in vacuum,

$$\text{offset delay}(s) = \frac{l\sqrt{\epsilon_r}}{c}. \quad (18)$$

The offset Z_o is the characteristic impedance within the offset length, while the offset loss represents the magnitude loss due to skin effect of the offset coaxial type standard only.

Figure 11 shows the flow graph model of an offset device, which is the case of the coaxial *open* and *short* standards of the cal Kit 85052C, used in this dissertation.

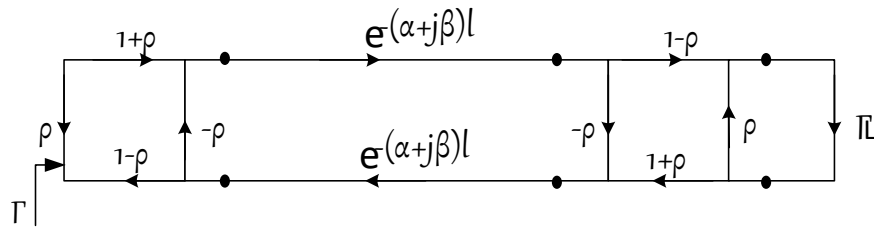


Figure 11. Signal flow graph model of an offset device.

The offset of the *open* and *short* standards are modeled as a perfectly uniform lossy air dielectric transmission line. Applying Mason rules to the signal flow graph of Figure 11, the expected reflection coefficient (Γ) of the standard is calculated as,

$$\Gamma = \rho + \frac{(1 - \rho^2)(e^{-2(\alpha+j\beta)l})[-\rho(1 - \rho\Gamma_L) + \Gamma_L(1 - \rho^2)]}{1 - \rho(e^{-2(\alpha+j\beta)l})[\rho - \Gamma_L(1 - \rho^2) - \rho\Gamma_L]}. \quad (19)$$

where $\Gamma_L = \frac{Z_L - Z_r}{Z_L + Z_r}$, Z_L is the standard impedance, $Z_r = 50 \text{ ohm}$, $\rho = \frac{Z_o - Z_r}{Z_o + Z_r}$, α and β are the propagation loss and phase constants of the offset line, and l is the physical length of the offset line.

To compute the standard reflection coefficient using equation (19), it is necessary to obtain:

1. Length of the offset line,

$$l = c \times \text{offset delay}, \text{ (for air dielectric } (\epsilon_r=1)).$$

2. Z_o , *Offset Delay*, *OffsetLoss*, the inductances, and capacitances are provided by the cal Kit.

3. Standard reflection coefficient:

$$\Gamma_{short} = \frac{j2\pi f L_t(f) - Z_o}{j2\pi f L_t(f) + Z_o} e^{-j4\pi l/\lambda}, \quad L_t = L_o + L_1 f + L_2 f^2 + L_3 f^3,$$

$$\Gamma_{open} = \frac{1 - j2\pi f C_t(f) Z_o}{1 + j2\pi f C_t(f) Z_o} e^{-j4\pi l/\lambda}, \quad C_t = C_o + C_1 f + C_2 f^2 + C_3 f^3.$$

Figure 12 (a) shows a comparison between the reflection coefficients of the open and short standards of the cal Kit 85052-C (3.5 mm), calculated with the models exposed before, and their corresponding measurements obtained with a calibrated VNA. Notably, a good correlation between them is achieved. The minimum and the maximum frequencies of these standards are 0 and 38.8 GHz. The span frequency is set to 2GHz – 4GHz to distinguish their trajectory in the Smith Chart. Figures 12 (b) and (c) show the simplified model of the open and short standards of the cal Kit 85052-C (3.5 mm). The ideal-open and short are located at (∞) and (0) in the Smith Chart, respectively, for all frequencies. Due to the phase of the offset delay, the open fringing capacitance, short inductance, and the length of the offset line, change with frequency in the clockwise direction, as shown in Figure 12 (a) shows.

The model of the load standard is shown in Figure 13 (a). It is formed by a delay line terminating with a resistance R. Its value can be different from the impedance of the system Z_o , but for simplicity, the impedance of the delay line and R are commonly set to Z_o . Therefore the input impedance of the model is Z_o , which gives a $\Gamma = 0$. Finally, in Figure 13 (b), an alternative to model the load standard is shown, which consists in a delay line terminated by a series R-L circuit. This is useful to model on-wafer load standards.

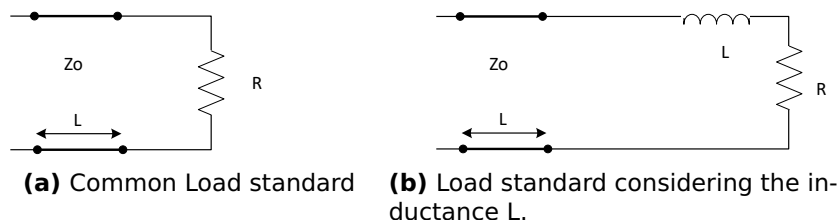
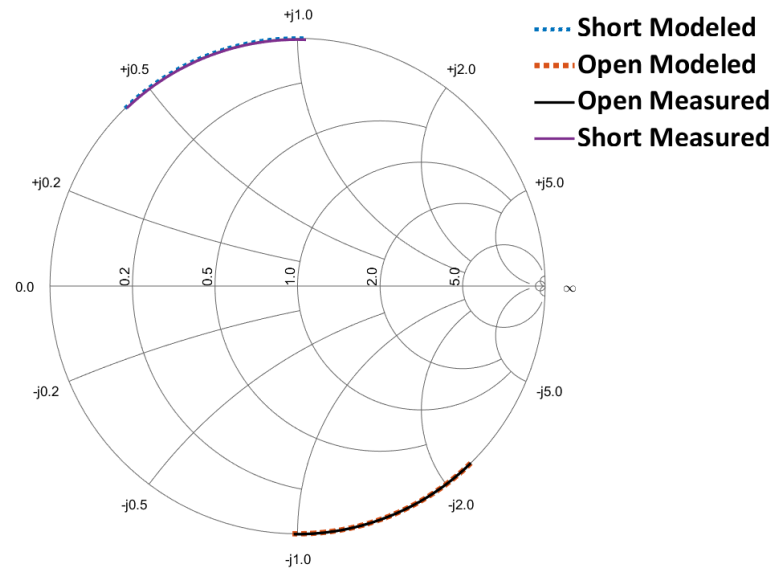
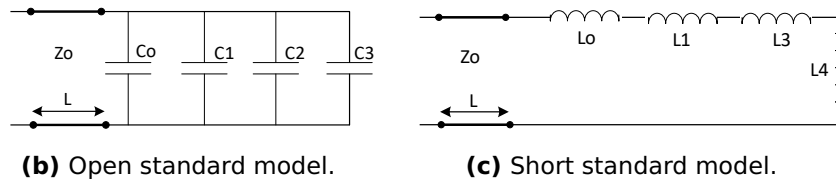


Figure 13. Load standard models.



(a) Open and short standards in Smith Chart.



(b) Open standard model.

(c) Short standard model.

Figure 12. Open and short standard models of the cal Kit 85052-C.

2.4.2 Short-Open-Load-Reciprocal (SOLR) calibration technique

Different methods are developed to determine the 8-term-error of the of Figure 7 (a). The SOLR method described in Ferrero and Pisani (1992) is useful when a non-insertable connectors are used (DUT with the same-sex connectors on each port) or when on-wafer devices are measured. It does not require a known *thru* standard, as long as it satisfies the reciprocity property ($S_{21} = S_{12}$). If the DUT is reciprocal, it can be used itself as the unknown *thru*, reducing, in this case, the number of connections.

It is noted from Figure 7 (a) that the signal flow graph is a cascade of the input port error box (x), the DUT, and the output error box (y), therefore using the transmission matrix (T) defined in equation (21), it is more appropriate to express the measured S-parameters in terms of the actual S-parameters for a linear DUT using:

$$\begin{bmatrix} a_1 \\ b_1 \end{bmatrix} = \begin{bmatrix} t_{11} & t_{12} \\ t_{21} & t_{22} \end{bmatrix} \begin{bmatrix} b_2 \\ a_2 \end{bmatrix}, \quad (20)$$

where t_{ij} is related to S_{ij} ,

$$T = \frac{1}{S_{21}} \begin{bmatrix} 1 & -S_{22} \\ S_{11} & -\Delta_S \end{bmatrix}, \quad (21)$$

$$\Delta_S = S_{11}S_{22} - S_{21}S_{12}.$$

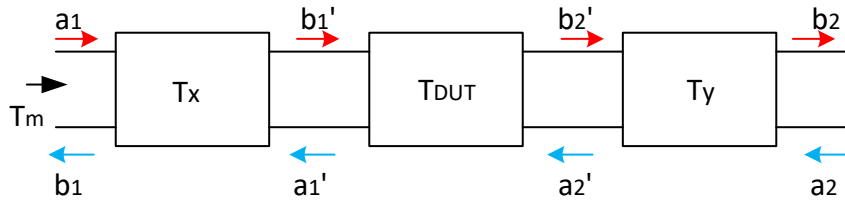


Figure 14. Cascade representation of two-ports VNA.

Figure 14 shows the cascade representation of a two-ports VNA with a DUT. To obtain the expression of the transmitting matrix T_m from the S-parameters measured with the VNA, the equation (21). Applying the transmission matrix to all three stages in Figure 14 we have:

$$\begin{bmatrix} a_1 \\ b_1 \end{bmatrix} = T_x \begin{bmatrix} b'_1 \\ a'_1 \end{bmatrix}, \quad \begin{bmatrix} b'_1 \\ a'_1 \end{bmatrix} = T_{DUT} \begin{bmatrix} b'_2 \\ a'_2 \end{bmatrix}, \quad \begin{bmatrix} b'_2 \\ a'_2 \end{bmatrix} = T_y \begin{bmatrix} b_2 \\ a_2 \end{bmatrix}. \quad (22)$$

Given we define T_m from:

$$\begin{bmatrix} a_1 \\ b_1 \end{bmatrix} = T_m \begin{bmatrix} b_2 \\ a_2 \end{bmatrix}, \quad (23)$$

it results from equations (22) and (23) that we have $T_m = T_x T_{DUT} T_y$,

$$\begin{bmatrix} a_1 \\ b_1 \end{bmatrix} = T_x T_{DUT} T_y \begin{bmatrix} b_2 \\ a_2 \end{bmatrix}. \quad (24)$$

Equation (24), shows that, when devices are placed in cascade configuration, the total transmitting matrix is simple computed as a multiplication of each individual T-matrix. To obtain the S-parameters of the cascade configuration, a simple conversion from T to S-parameters is done.

The transmitted measured matrix (T_m), in function of each port term-errors and the scattering parameters of the DUT is shown in equation (25). It is noticed that S_{21} and $e_{10}e_{32}$, must be non-zero. Similarly the transmission tracking term in reverse direction ($e_{23}e_{01}$) of equation (26),

$$T_x = \frac{1}{e_{10}} \begin{bmatrix} 1 & -e_{11} \\ e_{00} & -\Delta_x \end{bmatrix}, \quad T_y = \frac{1}{e_{32}} \begin{bmatrix} 1 & -e_{22} \\ e_{33} & -\Delta_y \end{bmatrix},$$

$$\Delta_x = e_{00}e_{11} - e_{10}e_{01}, \quad \Delta_y = e_{22}e_{33} - e_{32}e_{23}, \quad (25)$$

$$T_m = \frac{1}{e_{10}e_{32}} \begin{bmatrix} 1 & -e_{11} \\ e_{00} & -\Delta_x \end{bmatrix} \frac{1}{S_{21}} \begin{bmatrix} 1 & -S_{22} \\ S_{11} & -\Delta_s \end{bmatrix} \begin{bmatrix} 1 & -e_{22} \\ e_{33} & -\Delta_y \end{bmatrix}. \quad (26)$$

The actual values T_{DUT} -matrix of the DUT, are obtained by inverting the input (T_x) and output (T_y) matrices, as shown in equation (26):

$$T_{DUT} = T_x^{-1} T_m T_y^{-1},$$

$$T_{DUT} = \frac{1}{e_{23}e_{01}} \begin{bmatrix} -\Delta_x & e_{11} \\ -e_{00} & 1 \end{bmatrix} \begin{bmatrix} t_{11m} & t_{12m} \\ t_{21m} & t_{22m} \end{bmatrix} \begin{bmatrix} -\Delta_y & e_{33} \\ -e_{22} & 1 \end{bmatrix}. \quad (27)$$

An important aspect of the 8-term error model, shown in Figure 5, is that, only seven independent terms are needed: three error-terms at port one (e_{00} , e_{11} , Δ_x), three at port two (e_{22} , e_{33} , Δ_y). They are calculated from the one-port calibration, and the transmission tracking error measured in reverse direction $e_{23}e_{01}$. The transmission tracking error measured in the forward ($e_{10}e_{32}$) and reverse directions, present in equation (25), (26), respectively, are calculated as presented in Ferrero and Pisani

(1992), where the only requirement is to use as element of calibration a reciprocal device, called unknown *thru*. Knowing that the determinant of the transmission matrix of a reciprocal device is 1, $e_{23}e_{01}$ is calculated as shown in equation (28),

$$e_{23}e_{01}I = T_{DUT}^{-1}T_{x_1}^{-1}T_mT_{y_1}^{-1},$$

$$\det(e_{23}e_{01}I) = \det(T_{DUT}^{-1})\det(T_{x_1}^{-1})\det(T_m)\det(T_{y_1}^{-1}),$$

where I is the identity matrix, and T_{x_1} and T_{y_1} are defined as,

$$T_{x_1} = \begin{bmatrix} 1 & -e_{11} \\ e_{00} & -\Delta_x \end{bmatrix}, \quad T_{y_1} = \begin{bmatrix} 1 & -e_{22} \\ e_{33} & -\Delta_y \end{bmatrix},$$

$$e_{23}e_{01} = \pm \sqrt{\det(T_{x_1})\det(T_m)\det(T_{y_1})}. \quad (28)$$

The transmission tracking error measured in forward direction ($e_{01}e_{23}$), is obtained by calculating the determinant of equation (27),

$$e_{01}e_{23} = \pm \sqrt{\frac{\det(T'_x)\det(T'_y)}{\det(T_m)}}, \quad (29)$$

with T'_x and T'_y defined as,

$$T'_x = \begin{bmatrix} -\Delta_x & e_{11} \\ -e_{00} & 1 \end{bmatrix}, \quad T'_y = \begin{bmatrix} -\Delta_y & e_{22} \\ -e_{33} & 1 \end{bmatrix}.$$

To determine the sign of ($e_{01}e_{23}$) and ($e_{23}e_{01}$) the X matrix is computed as equation (30), where all the error elements are known, and T_m is the raw measured transmission matrix of the unknown *thru*. A rough knowledge of the S_{21} phase shift (≤ 180), allows

to solve the sign ambiguity,

$$X = T_x^{-1} T_m (T_y^{-1}), \quad (30)$$

$$X = \frac{1}{e_{23}e_{01}} T_{DUT},$$

$$S21_{thru} = \frac{e_{23}e_{01}}{X_{11}}. \quad (31)$$

The $e_{23}e_{01}$ is a characteristics of the test set. Therefore, it must be kept constant and independent of the unknown *thru* used. Several reciprocal devices are used to demonstrate it. Figures 15 (a) and (b) show the absolute values of the transmission tracking obtained in forward and reverse direction, calculated using two lines of different length (4 cm and 6.89 cm), a 3 dB attenuator, and a directional coupler (the coupling port was loaded with 50 ohm). A good correlation between them is achieved. The span frequency selected is 1 GHz – 20 GHz, with 401 points.

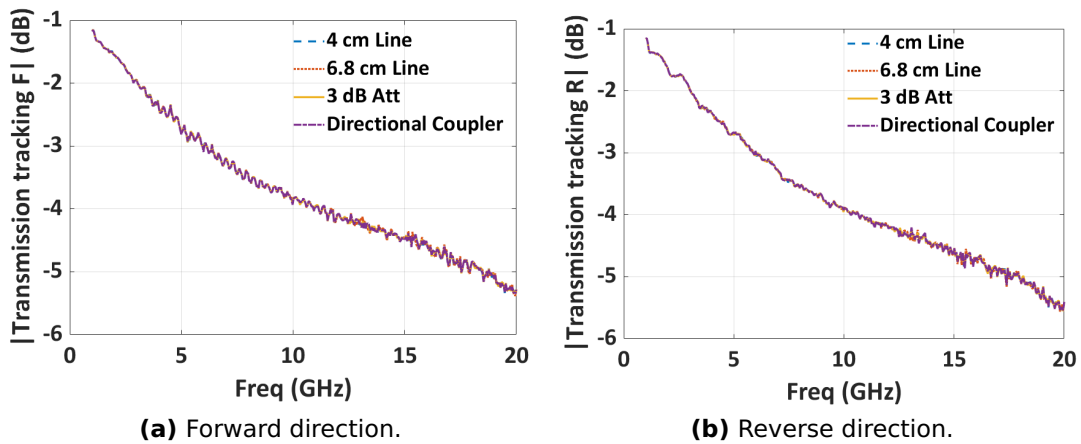


Figure 15. Amplitude of the transmission tracking error (dB).

Figures 16 (a) and (b) show the phase of the transmission tracking error measured in the forward and reverse directions, respectively. Also shown are the positive (blue) and the negative (red) roots of equation (28). It is appreciable that the selected phase of the errors is alternating its value between both roots (for more details, both graphs were zoomed in).

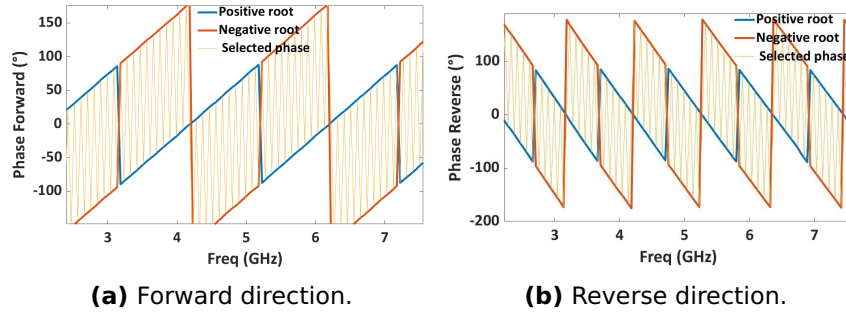


Figure 16. Phase of the transmission tracking error (°).

Once all the error-terms are calculated, the error correction algorithms are applied to the measured DUT measurements to correct for the testbed calibration errors. The S-parameters of the linear device, showed in equation (32), are calculated by matching the left and right elements of equation (30), where X_{ij} are the entries of the matrix X . It is noticed from equation (32), that the transmission tracking error is only present in the transmission scattering parameters (S_{21} , S_{12}) of the DUT, as expected,

$$S_{DUT} = \begin{bmatrix} \frac{X_{21}}{X_{11}} & \frac{1}{e_{23}e_{01}} \frac{X_{22}X_{11} - X_{21}X_{12}}{X_{11}} \\ \frac{e_{23}e_{01}}{X_{11}} & -\frac{X_{12}}{X_{11}} \end{bmatrix}. \quad (32)$$

Figure 17, shows the S-parameters of a 50 ohm line with a length of 6.8 cm, fabricated in a Rogers RT Duroid 5880 substrate with $\epsilon_r = 2.1$. It is noticed from Figures 17 (b) and (c) that the device satisfies the reciprocity property required for the calculation of the transmission tracking errors. Also, the amplitudes shown in Figures 17 (b) are noisy, which is due to the imperfection in the switch.

2.4.3 Quick-SOLT (QSOLT) calibration technique

The Short-Open-Load-Thru (SOLT) calibration and QSOLT calibration (proposed in Ferrero and Pisani (1991)), provide alternative methods to determine the 8-term-errors of a 2-port VNA, but unlike the SOLR, they require a well defined *thru*. The speed of the QSOLT lies in the fact that the 1-port calibration is performed in only one of the test ports (the SOLT performs 1-port calibration at each test port). The QSOLT has 7-term-errors plus the switch error, which are determined during measurements of the *thru*. The one-port three error-terms are obtained using the 1-port calibration. The

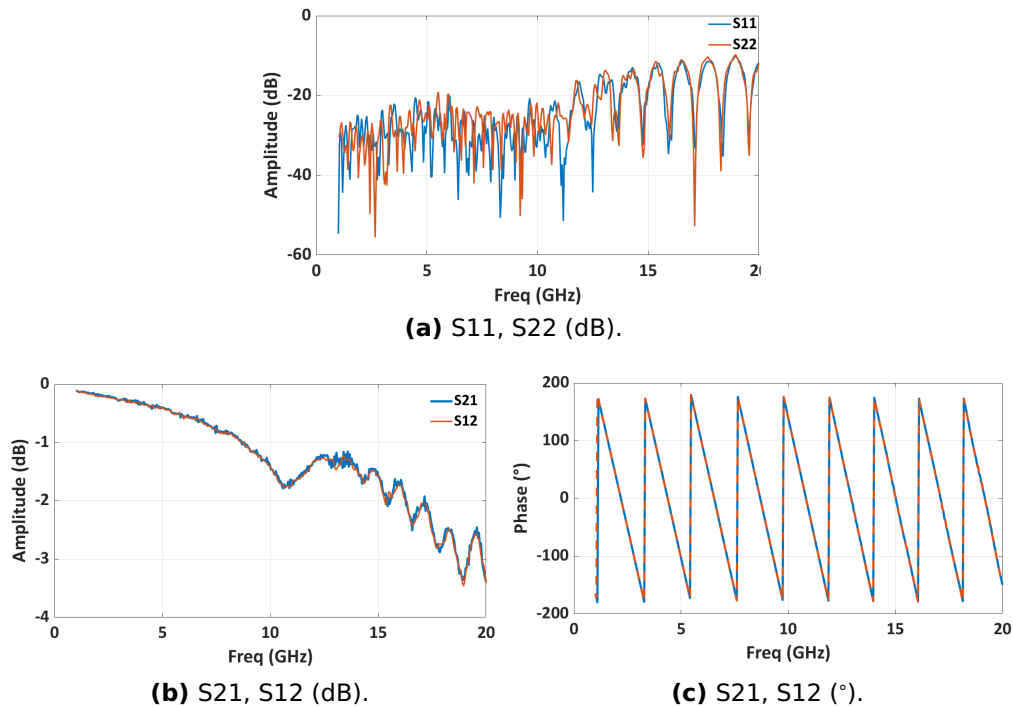


Figure 17. S-parameters of a 6.8 cm line without removing the switch errors.

remaining 4-terms are determined with the 4 independent equations formed with the well known *thru*'s S-parameters.

2.4.4 Thru-Reflect-Line (TRL) calibration technique

The TRL calibration as the QSOLT has 7-term-error and the switch error. As its name indicates, it uses, as standards, a zero-length *thru*, *reflects*, and a *line* Figure 18. All the *lines* have the same impedance Z_L and propagation constant γ . And the *reflects* connected to each port are identical. The TRL theory is derived in Appendix 1. Another version of TRL is sometimes called Line-Reflect-Line (LRL), but they are essentially the same. The difference is that LRL uses a non-zero-length *thru* standard, which is the case for on-wafer measurements where the probes can not be connected. The TRL calibration method was presented by Engen and Hoer (1979), where the transmitting parameters are used, and also they assumed that the delay line is non-reflecting, which means that the calibration reference impedance is identical to the delay line impedance Z_L . The *line* standard length must be different from the *thru* length in such a way that the shift phase through the *thru* is different from the shift phase of the *line* by at least 20° and no more than 160° , limiting the calibration bandwidth.

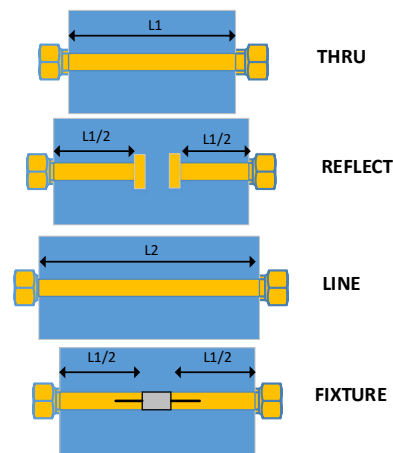


Figure 18. Standards of the TRL technique.

In Marks (1991) a Multi-line TRL method is presented, where multiple redundant lines are incorporated. This method increases the calibration bandwidth. It reduces the random errors (introduced, for example, by poor connector repeatability), improves the accuracy concerning the conventional TRL method, while extending the calibration bandwidth with use of multiple lines. In DeGroot *et al.* (2002), the Multi-line TRL algorithm and the estimation of the transmission line propagation constant are presented. In Lopez-Gonzalez *et al.* (2006) the Multi-line TRL algorithm with the Huber estimation is proposed to enhance the reduction of the random effects. In Reynoso-Hernandez *et al.* (2012) the conventional TRL method is derived with ABCD parameters instead of transmitting parameters; an approach which yields a proof that the calibration reference impedance is referred to Z_0 . Therefore, it is not required to a reference impedance transformation after the calibration as in Engen and Hoer (1979). The Thru-Reflect-Match (TRM), Line-Reflect-Match (LRM) and Line-Reflect-Reflect-Match (LRRM) are other advanced techniques to determine the systematic errors of the PNA-X. A generalized TRM calibration technique is explained for the first time in Pulido-Gaytán *et al.* (2015), where a symmetrical or nonsymmetrical load of arbitrary impedance can be used for the match standard.

They are useful to characterize a DUT on a fixture, as is the case of a packaged transistor. In the next chapter, the TRL technique used to calibrate an LP system is presented in details.

Chapter 3. Load-Pull (LP) techniques

In this chapter, the operation principle and the concept of LP systems will be explained. The active, passive and hybrid LP techniques and their main advantages and disadvantages will be covered. A real-time LP measurement testbed to characterize a GaN HEMT transistor under CW and multitone signals will be developed. The LP measurement results of the CGH40010F transistor from Wolfspeed, CREE will be presented.

3.1 Introduction

In all telecommunication systems, the priority is to send and receive data without loss of information and to accomplish this within the norms of the International Telecommunication Union (ITU), such as the emitted power level and the maximum allowed power in the side-bands. The design of Radio Frequency Power Amplifier (RFPA) in the broadcast system has been given special attention over the years due to the constant growth of wireless communication technology and the necessity to develop systems with greater bandwidth and linearity to avoid in-band distortion, loss of information, and spectral regrowth, which can interfere with other channels that share the same communication medium.

It has been demonstrated that the PA is more efficient when it works near to or beyond the 1 dB compression point (P_{1dB}), where it exhibits a nonlinear behavior and produces a distorted output signal increasing the spectral regrowth and reducing the linearity of the PA. Therefore it is not possible to simultaneously reach the optimal level of linearity and efficiency. Several complex RFPA architectures have been proposed in the literature to satisfy both conditions, such as Doherty, Chireix, Linear amplification using Nonlinear Components (LINC), and others. Figure 19 shows a simplified block diagram of an RFPA, which consists of an Input Matching Network (IMN), an Output Matching Network (OMN), and a transistor device. The matching network designs depend on the RFPA application. For example, they could be designed to amplify minimal signals with very low noise at the output (low noise amplifier) to maximize the Gain or maximum output power (PA).

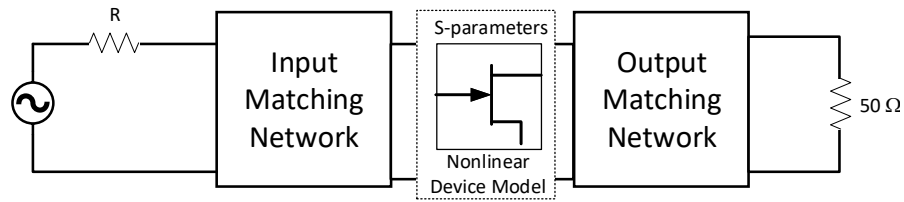


Figure 19. General block diagram of an RFPA.

Independently of the application, the IMN and OMN are made with lumped, distributed elements (transmission line) or a combination of both. Linear elements commonly characterize them. Therefore they are considered linear-time-invariant networks. On the other hand, the active device can be considered a linear or a nonlinear network, depending on the input signal level.

It is considered that the device is working in the linear region if the output signal represents an amplified version of the input signal, without new spectral components, but if the input signal level is large enough to generate appreciable harmonics, then the device is operating in a nonlinear region. Figure 20 illustrates the output signals when linear and nonlinear operations are applied to a one tone signal.

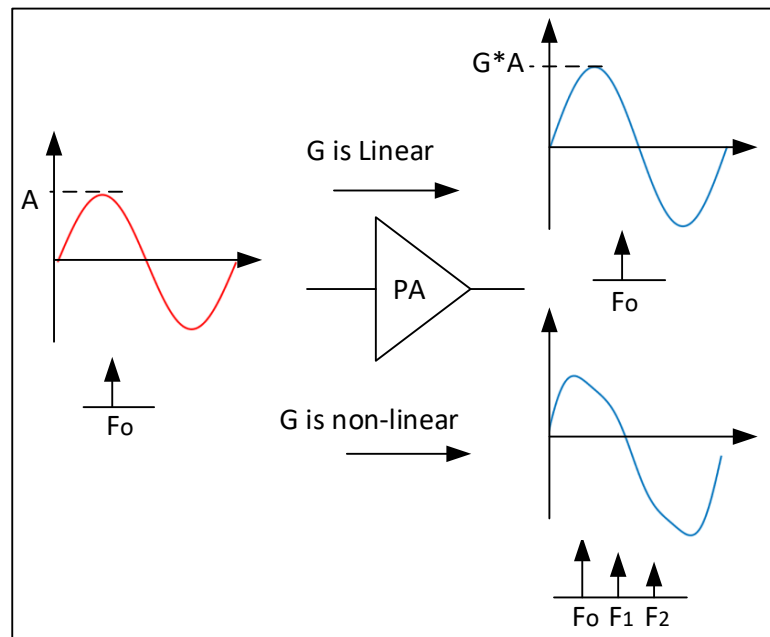


Figure 20. Linear and nonlinear behavior of RF PA.

For the RF PA designers, it is critical importance to have a model that describes

the nonlinear behavior of the transistor, under different bias conditions, across a wide-band frequency span. The success of the final RFPA design relies on the precision of the transistor described in the model. The S-parameters are used to represent the linear behavior under small signal stimuli. They are frequency and bias dependent but power level independent. The device load line, which represents the trajectory of the instantaneous current (i_{DS}) and voltage (v_{DS}) at a specific quiescent bias point (V_{DD} , I_{DD}) and a load termination (Z_L), are alternatively used to describe the device performance. In Ghannouchi and Hashmi (2013) the load line equation is defined as shown in equation (33) in linear operation for both real R_L and complex Z_L loads in class A operation (no harmonics):

$$i_{DS}(t) = I_{DD} - \frac{v_{DS}(t) - V_{DD}}{R_L} \quad \text{for real load } R_L, \quad (33)$$

$$i_{DS}(t) = I_{DD} - \text{Re} \left\{ \frac{V_{DS}(\omega) - V_{DD}}{Z_L(\omega)} e^{j\omega t} \right\} \quad \text{for complex load } Z_L(\omega). \quad (34)$$

When the load is real (R_L), the load line is a straight line (DC load line) as shown in Figure 21 with a red dash line, while for complex values (Z_L), the load line (RF load line) is a rotated ellipse (elliptic blue line in Figure 21). This happens at microwave frequency because of the parasitic capacitance, which introduces a phase shift between the Drain voltage and the voltage controlled current source, Salib *et al.* (1987).

Typical I-V curves characteristic of the Field-Effect Transistors (FET) are shown in Figure 21, where V_{DD} is the bias voltage and I_{DD} the bias current. It is appreciable that the load line is limited by the minimum voltage, also known as the knee voltage (V_{knee}), the maximum or breakdown voltage ($V_{breakdown}$) (maximum voltage swing of the device), the zero value current (I_{min}) and the maximum device's current (I_{max}) (maximum current swing of the device).

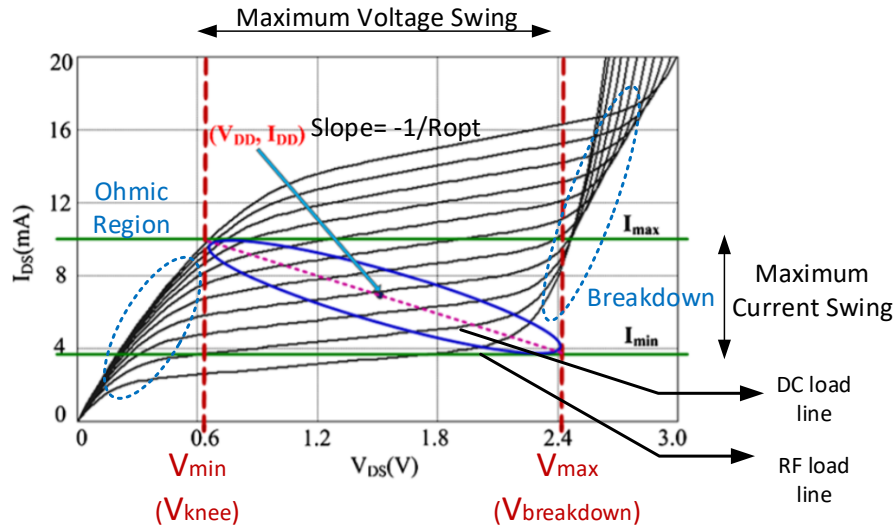


Figure 21. I-V curves, with the load line of a FET transistor

3.2 Conjugate and load line Match

Using the well known concept of conjugate match, the current generator of Figure 22, delivers the maximum output power into an external load when the load resistance is set to the conjugate of the generator impedance (the total reactance is zero, and the real part of both are equal).

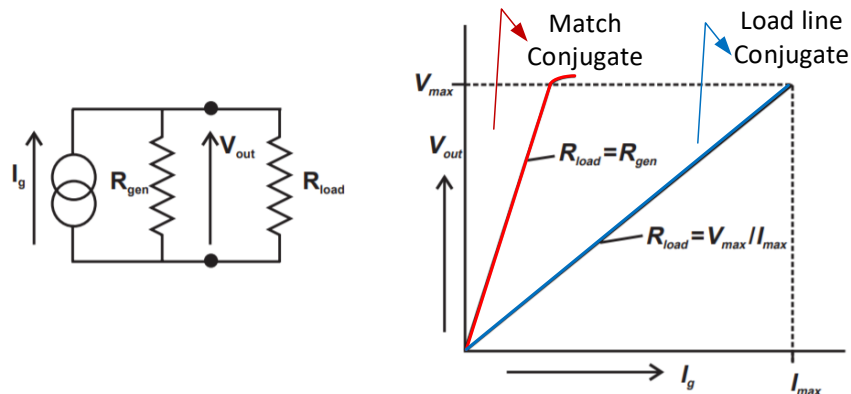


Figure 22. Conjugate and load line Match (from Cripps (1999)).

As an example, let us assume that the current generator of Figure 22 represents the output of the transistor and that in the saturation region it can be modeled by a current source with a current of 1 A and an output resistance of 100 Ω at a DC drain V_{DD} of

25 V. Applying the conjugate match theorem for maximum power gain, a load of 100Ω would be required. However if the voltage rating V_{max} of the device is 50 V, with such a load of 100Ω , the voltage appearing across the current generator terminals (active device) would then lead to an instantaneous voltage exceeding the maximum voltage in the upper swing as well as yielding negative drain voltages in the lower swing.

To obtain the maximum output power for a device, it is necessary to find the optimum load impedance (R_{opt}) that simultaneously increase the maximum voltage and current swings. This is known as the load-line match, Cripps (1999). In order to satisfy it, the slope of the load line will need to be reduced as shown in equation (35):

$$\frac{V_{max}}{I_{max}} = \frac{R_{gen}R_{opt}}{R_{gen} + R_{opt}}. \quad (35)$$

If the generator impedance verifies $R_{opt} \ll R_{gen}$, R_{opt} can be calculated as indicated in equation (36):

$$R_{opt} = \frac{V_{max}}{I_{max}}. \quad (36)$$

The load line match delivers the maximum output power possible by keeping the RF voltage and drain current swings within the specific limits of the transistor.

3.2.1 Impact of the load line on the output power of a nonlinear device

To describe the output power of the device as a function of the load line, a FET amplifier operating in class A as shown in Figure 23 is used as an example.. The amplifier is biased through the RF choke inductor L_c , which must have a very high reactance at RF frequency, with a bias voltage, V_{DD} and bias current, I_{DD} . C_o is the DC blocking capacitance.

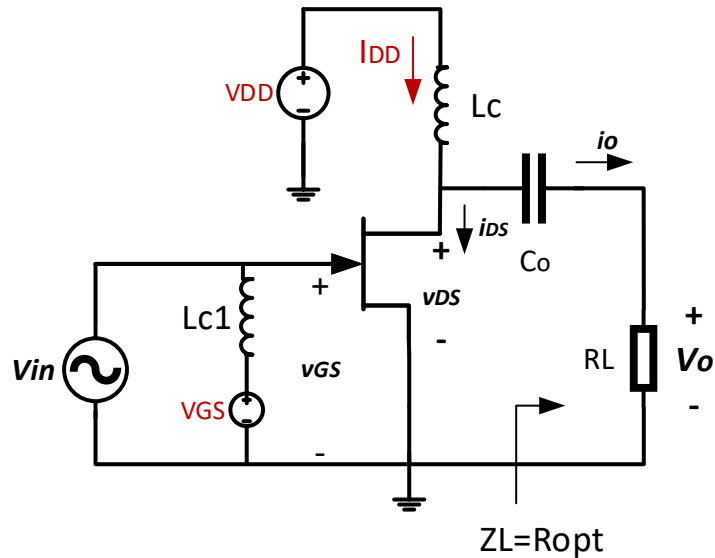


Figure 23. Typical schematic of a FET amplifier.

Considering that the class A amplifier is operating under the following assumptions:

1. zero output conductance.
2. zero turn on (or knee) voltage such that $V_{DD} = V_{max}/2$.
3. The drain-to-source voltage v_{DS} swings from 0 to $V_{max} = 2V_{DD}$, and the drain current swings from zero to I_{max} , with an amplitude $I_{max}/2$. The values of V_{DD} and I_{DD} guarantee that the transistor is always conducting; therefore the conduction angle is $\theta = 360^\circ$.
4. The device is always operating in the linear region, therefore the drain current waveform is proportional to the voltage v_{GS} and does not contain harmonic and intermodulation products.

The waveforms associated with the instantaneous drain-to-source voltage $v_{DS}(\omega t)$ and drain current $i_{DS}(\omega t)$ and output $v_o(\omega t)$ voltages are shown in Figure 24 assuming that the input voltage $v_{in}(\omega t)$ is a sinusoidal waveform and the load is a pure resistance R_L .

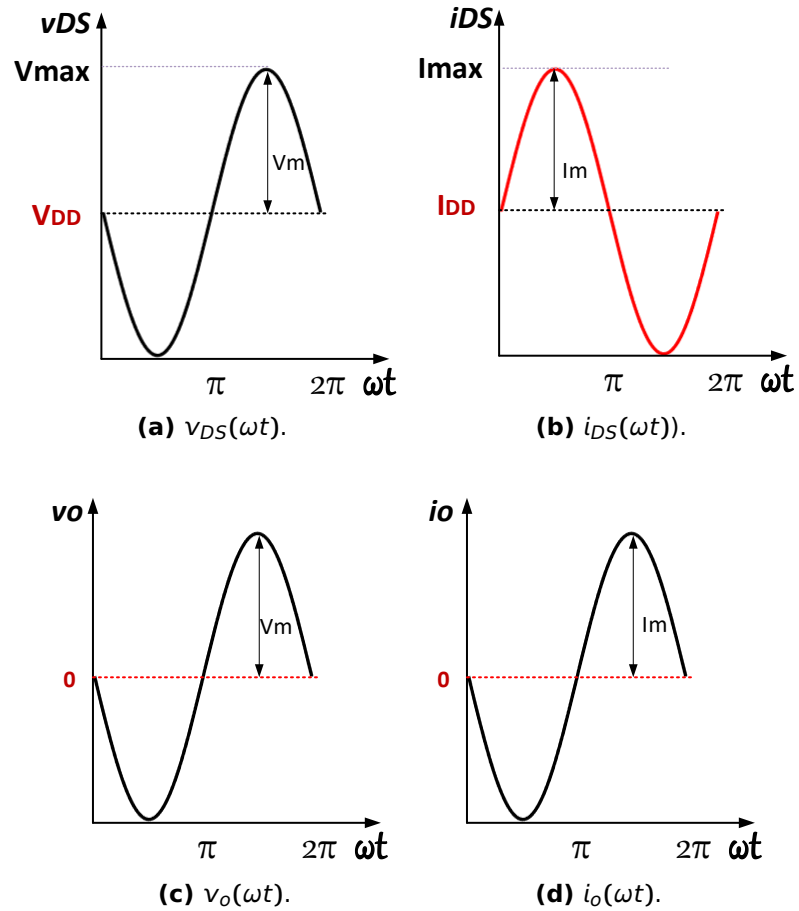


Figure 24. Waveforms in class A RF PA.

Their expressions are shown in equation (37):

$$\begin{aligned}
 v_{DS}(\omega t) &= V_{DD} - V_m \sin(\omega t), \\
 i_{DS}(\omega t) &= I_{DD} + I_m \sin(\omega t), \\
 v_o(\omega t) &= -V_m \sin(\omega t), \\
 i_o(\omega t) &= -I_m \sin(\omega t),
 \end{aligned} \tag{37}$$

where $V_m = V_{DD}$, and $I_m = I_{DD}$.

The instantaneous RF power delivered by the transistor to the pure resistive load

R_L shown in Figure 25 is given by:

$$\begin{aligned}
 p_o(\omega t) &= v_o(\omega t)i_o(\omega t) = (-V_m \sin(\omega t))(-I_m \sin(\omega t)) \\
 &= V_m I_m \sin^2(\omega t) \\
 &= \frac{V_m I_m}{2} (1 - \cos(2\omega t)),
 \end{aligned} \tag{38}$$

and the optimum output average power ($P_{o_{avg}}$) over a cycle is:

$$\begin{aligned}
 P_{o_{avg}} &= \frac{1}{2\pi} \int_0^{2\pi} p_o(\omega t) d\omega t = \frac{V_m I_m}{4\pi} \int_0^{2\pi} (1 - \cos(2\omega t)) d\omega t \\
 &= \frac{V_m I_m}{2} = \frac{V_m^2}{2R_L} = \frac{I_m^2 R_L}{2} \\
 &= \frac{V_{DD} I_{DD}}{2}.
 \end{aligned} \tag{39}$$

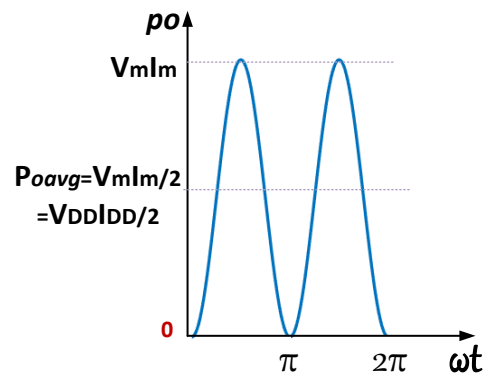


Figure 25. Instantaneous output power in class A amplifier.

From equation (38) it is noticed that the delivered average power to the load is half of the DC power. Knowing that the PA DE is given by equation (40), the DE of class A amplifier is 50 %.

$$\eta = \frac{P_{o_{avg}}}{P_{DC}} \cdot 100 = 50\% \tag{40}$$

Applying the concept of load line match, the R_{opt} is:

$$R_{opt} = \frac{V_{DD}}{I_{DD}} \tag{41}$$

Using equation (39), one can verify that the pure resistive load terminations pR_{opt} and R_{opt}/p produce the same power $P_{o_{avg}}/p$. In the case of lower resistive load R_{opt}/p

($\rho > 1$), the device can swing over the full current range I_{max} , while the voltage swing is only $2V_{DD}/\rho$. For the higher resistive load, ρR_{opt} , the drive level has to be backed off to reduce the current swing by the ratio of ρ , and keep the voltage swing at the maximum peak value of $2V_{DD}$, Cripps (1999). Figure 26 shows the drain current and voltage waveforms for the two resistive loads which yield the same average power $P_{o_{avg}}/\rho$.

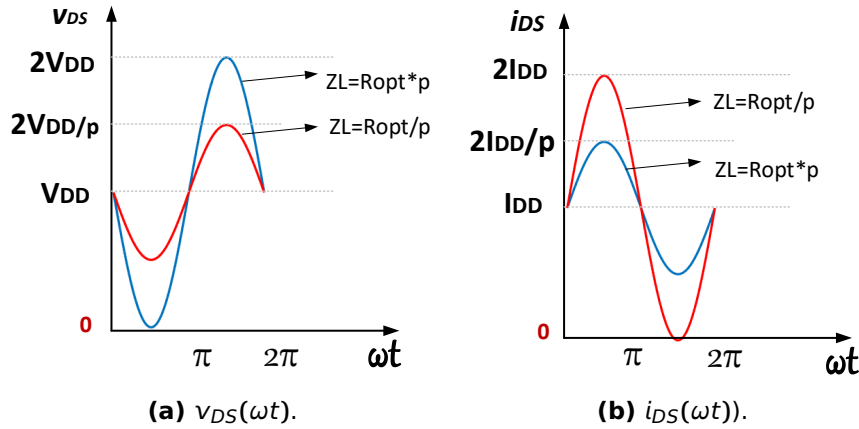


Figure 26. Drain waveforms in class A amplifier for different resistive loads, which produce the same output RF power.

When a reactance X_L is placed in series with the resistive load R_L/ρ , the output current remains given by $i_o(\omega t) = -I_m \sin(\omega t)$ while the output voltage is phase shifted by the load $v_o(\omega t) = -|V_\alpha| \sin(\omega t - \phi)$ with ϕ the phase difference between the current and the voltage waveforms. The average power over a cycle is then given by:

$$\begin{aligned} P_{o_{avg}} &= \frac{|V_\alpha| I_m}{2\pi} \int_0^{2\pi} \sin(\omega t - \phi) \sin(\omega t) d\omega t \\ &= \frac{V_\alpha I_m \cos(\phi)}{2} = \frac{R I_m^2}{2\rho} = \frac{P_{avg}(\rho = 1)}{\rho}. \end{aligned} \quad (42)$$

using $\cos \phi |V_\alpha| = R I_m / \rho = V_m / \rho$. Note that the angle ϕ verifies:

$$\cos \phi = \frac{V_m}{|V_\alpha| \rho} = \frac{R_L / \rho}{\sqrt{(R_L / \rho)^2 + X_L^2}}. \quad (43)$$

Keeping the swing of the drain voltage equal to the maximum value $|V_\alpha| = V_m$ we obtain:

$$\rho = \frac{1}{\cos \phi}.$$

From equation (42), this values of ϕ maintains then the average output power constant $P_{o_{avg}}(p = 1)/p$ while operating with the maximum drain voltage and current swings. Smaller swings of the drain voltage V_α can also be used to maintain a constant output power $P_{o_{avg}}(p = 1)/p$:

$$\frac{V_m}{p \cos \phi} \leq |V_\alpha| \leq V_m \text{ for } p \cos \phi > 1.$$

Figure 27 (a) shows the output voltage waveforms for various sets of amplitudes and phases (ϕ), that generate a constant average output power $P_{o_{avg}}/p$ when the drain current swing remains between zero and $2I_{DD}$.

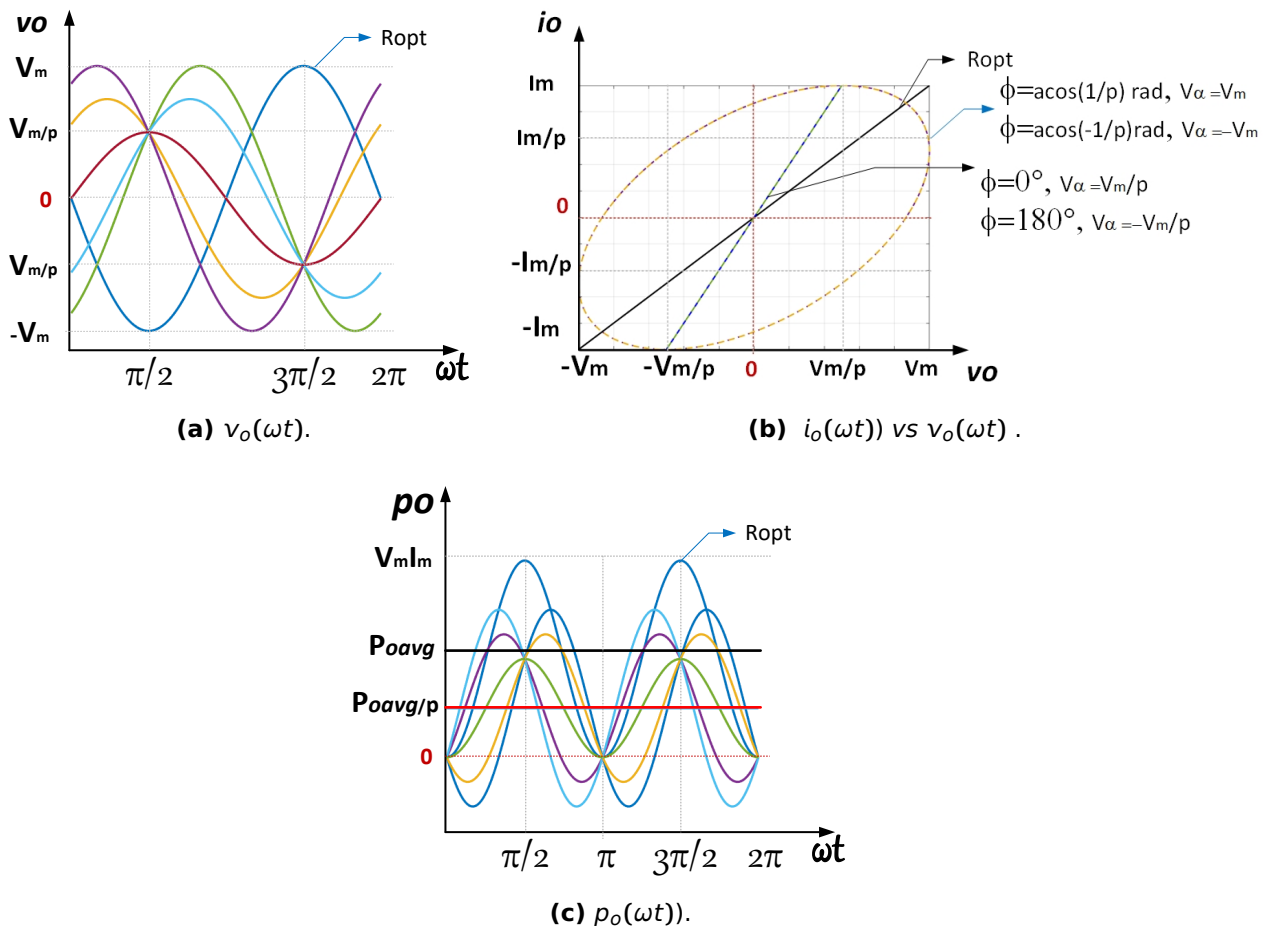


Figure 27. Output voltage waveforms in class A amplifier that generate the same average output power $P_{o_{avg}}/p$, with Drain current swing ($0-2I_{DD}$).

Figure 27 (b) shows the load line trajectories which are obtained assuming for:

1. The optimum average power ($P_{o_{avg}}$) where the load termination is pure resistive R_{opt} , and the current and voltage swings reach their maximum values (this behavior is shown with the black solid line).
2. A fraction of the optimum average power ($P_{o_{avg}}/p$), obtained with a pure resistive load termination R_{opt}/p , the output current swing reach its maximum value, while the voltage swing is limited to $|V_m/p|$ (this behavior is shown using a blue line)
3. A fraction of the optimum average power ($P_{o_{avg}}/p$), obtained with a reactance in series with a pure resistive load R_{opt}/p , which describes a rotate elliptical trajectories, (this behavior is shown with a XXXX line).

Figure 27 (c) displays the instantaneous output power waveforms and the average powers (red and black solid horizontal lines) for the cases mentioned before.

Table 2 summarize the permissible range of output voltage waveform amplitudes with their respective phases, for which $P_{o_{avg}}/p$.

Table 2. Output voltage amplitudes and their respective phases ϕ , which give $P_{o_{avg}}/p$

V_α	$\phi(rad)$
$-V_m/p$	π
$-V_m$	$\cos^{-1}(-1/p)$
V_m/p	0
V_m	$\cos^{-1}(1/p)$

The same analysis to obtain $P_{o_{avg}}/p$ is used, when the voltage swing reach the maximum level, and the current is reduced to $|I_m/p|$, which is achieved with a reactance in parallel with the pure resistive load pR_{opt} , the current waveform amplitudes satisfies:

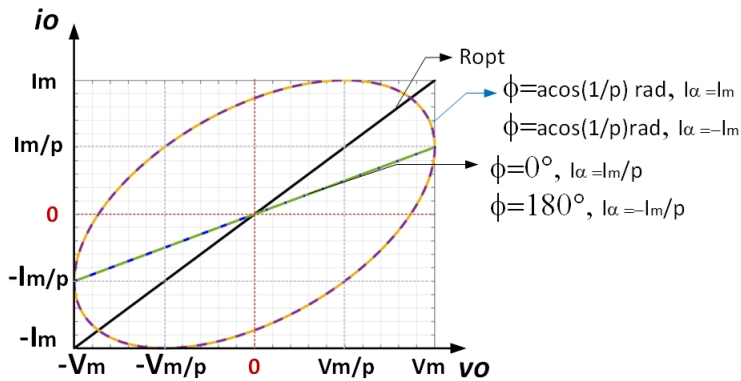
$$\frac{I_m}{p} \leq |I_\alpha| \leq I_m \quad (44)$$

Table 3 shows the output current amplitudes with their respective phases ϕ for which the average output power remains constant with value $P_{o_{avg}}/p$.

Table 3. Output current amplitudes and their respective phases ϕ , which give $P_{o_{avg}}/\rho$

I_α	$\phi(\text{rad})$
$-I_m/\rho$	π
$-I_m$	$\cos^{-1}(-1/\rho)$
I_m/ρ	0
I_m	$\cos^{-1}(1/\rho)$

Figure 28, shows the load line trajectories to obtain the optimum average output power (black solid line), and a fraction of it $P_{o_{avg}}/\rho$ (the rest of the curves).

**Figure 28.** Load line trajectories to obtain the optimum average output power.

3.2.1.1 Calculating the series reactance values, for which the average output power remains constant.

As explained in the previous section, there are a set of ϕ values for which the average output power remains constant with value $P_{o_{avg}}/\rho$, while the output voltage swing is limited to V_{max}/ρ and the output current swing over the entire range. This is achieved with a series reactance and a pure resistive load $R_{LO} = R_{opt}/\rho$. The circuit of Figure 29 (a), with the phasor diagram shown in Figure 29 (b), are used to calculate the reactance values.

From the phasor diagram of 29 (b) the ϕ values are given by:

$$\phi = \tan^{-1}\left(\frac{X_m}{R_{opt}/\rho}\right) \quad (45)$$

Selecting $\phi = \cos^{-1}(-1/p)$ and $\phi = \cos^{-1}(1/p)$ values from Table 2, and applying the trigonometric identity $\tan(\cos^{-1}(\sigma)) = \frac{\sqrt{1-\sigma^2}}{\sigma}$, the reactance values are:

$$X_m = \pm R_{opt} \sqrt{1 - 1/p^2} \quad (46)$$

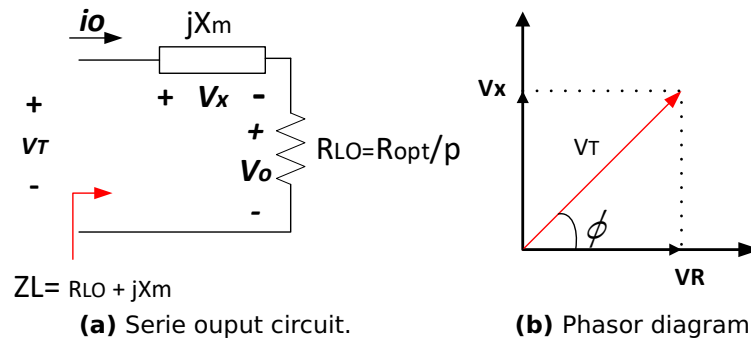


Figure 29. Class A amplifier with series reactance and pure resistive load $R_{LO} = R_{opt}/p$.

From equation (46), it is noticed that a series inductor, which give reactance values between zero and X_m and a pure resistive load $R_{LO} = R_{opt}/p$, maintain a constant average output power with value $P_{o_{avg}}/p$ over a cycle. Another solution is a circuit formed with series capacitance, for which the reactance values are between zero and $-X_m$. These values represent the black arc in the Smith Chart of Figure 31.

3.2.1.2 Calculating the shunts susceptance values, for which the average output power remains constant.

The circuit of Figure 30 (a) and its phasor diagram Figure 30 (b), are used to determine the shunts susceptance (B_m) values with a constant conductance $G_{HI} = 1/R_{HI}$, $R_{HI} = pR_{opt}$, for which the average output power remains constant with value $P_{o_{avg}}/p$. The ϕ values are calculating according to equation (47):

$$\phi = \tan^{-1} \left(\frac{i_G}{i_C} \right) = \tan^{-1} \left(\frac{B}{G} \right) \quad (47)$$

Selecting $\phi = \cos^{-1}(-1/p)$ and $\phi = \cos^{-1}(1/p)$ values from Table 3, the susceptance values are given by:

$$B_m = \pm G_{opt} \sqrt{1 - 1/p^2}, \quad (48)$$

where $G_{opt} = 1/R_{opt}$.

The values of susceptance between zero and B_m are obtained with a shunt capacitor,

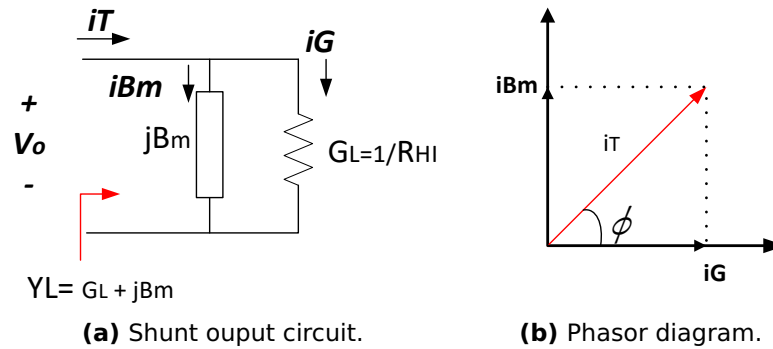


Figure 30. Class A amplifier with shunt susceptance and a conductance $G_{HI} = 1/pR_{opt}$.

while the negative values with a shunt inductor. These values are represented by the red arc in the Smith Chart of Figure 31. The black and red arcs of Figure 31,

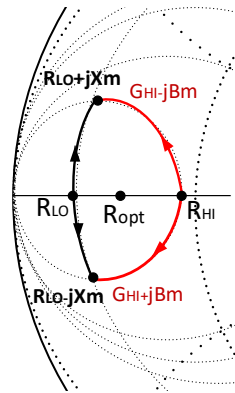


Figure 31. Constant power contour in Smith Chart.

form a closed contour with constant average power value of $P_{o_{avg}}/p$. The intersection points of both arcs satisfied that the impedances $Z_L = R_{LO} \pm jX_m$ it is the same as the

admittances $Y_L = G_{HI} \mp jB_m$, the demonstration is shows above:

$$\begin{aligned}
 Y_A &= \frac{1}{Z_L} = \frac{1}{R_{LO} \pm jX_m} \\
 &= \frac{R_{opt}/\rho \mp jR_{opt}\sqrt{1-1/\rho^2}}{R_{opt}^2} \\
 Y_A &= \frac{1}{\rho R_{opt}} \mp j \frac{1}{R_{opt}} \sqrt{1-1/\rho^2}, \tag{49}
 \end{aligned}$$

where $G_{HI} = \frac{1}{\rho R_{opt}}$, and $B_m = \mp \frac{1}{R_{opt}} \sqrt{1-1/\rho^2}$, therefore the admittance $Y_A = \frac{1}{Z_L}$, is equal to Y_L .

3.2.2 Transistor package effect on the constant power contours.

The constant power contours obtained before, are valid when the operation frequency is low enough to discard the effect of a device's package parasitics, case where the termination load is connected directly to the voltage controlled current terminals. When the encapsulated transistor is working in microwave frequencies, the device's output capacitance, or the package parasites, change the load at the reference plane of the current source, which causes the power contours to be frequency-dependent. The process to compensate the impedance load for removing these effect, and get a determined behavior at the current source plane, is known as de-embedding.

To study the impact of the device's output capacitance and the package parasitics (capacitive and inductive), the circuit of Figure 32 is used, where L is the inductance which model bond-wires used to connect the transistor's die to the package, and the shunt capacitance model the output and package parasitic capacitances.

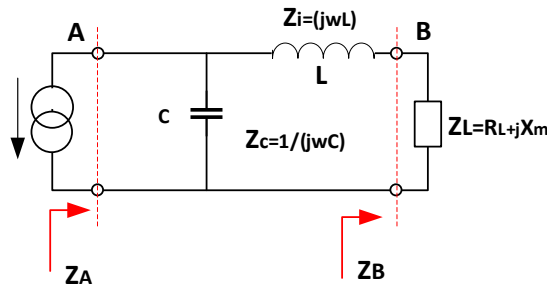


Figure 32. 2-port network used to emulate the effect of package on the constant power contours.

Applying circuit theory to the network shown in Figure 32, the impedance at the current source reference plane A (Z_A), is given by the following expression:

$$Z_A = \frac{Z_L + Z_i}{Y_c Z_L + (1 + Y_c Z_i)}, \quad (50)$$

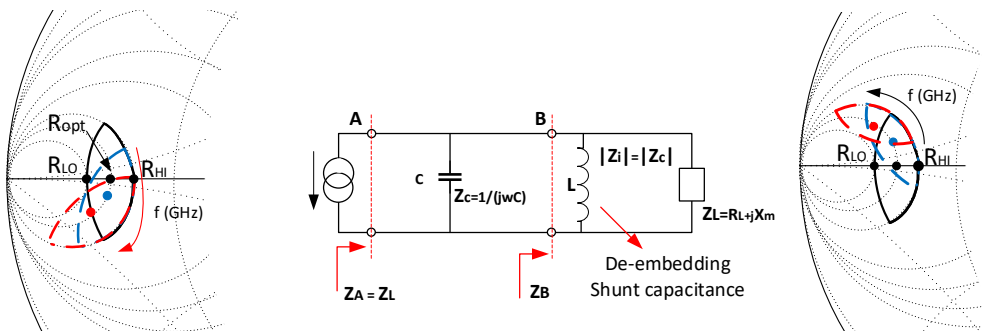
where $Y_c = j\omega C$, $Z_i = j\omega L$, $Z_L = R_L + jX_m$ is the load impedance.

Considering the analysis of two cases:

1. Only the shunt capacitance is take into account ($Z_i = 0$), the admittance Y_A at reference plane A is:

$$\begin{aligned} Y_A &= Y_L + Y_c \\ &= Y_L + j\omega C \end{aligned} \quad (51)$$

From equation (51), it is observed that for a constant value of C , the susceptance Y_A changes with the frequency, making the power contours frequency-dependent, and they will appear rotated around the circle of constant conductance ($G = 1/R_L$, $R_L = pR_{opt}$). Figure 33 (a) shows the rotation of the power contour versus frequency due to the impedance transformation that experiments Z_L at reference plane A.



(a) Power contour at A reference plane. **(b)** Shunt capacitance de-embedding. **(c)** Power contour at B reference plane.

Figure 33. Rotation of the power contour along the constant conductance circle ($G = 1/pR_{opt}$).

A shunt inductor with the same susceptance magnitude is placed at reference

plane B to compensate (de-embedding) the capacitance effects, therefore $Z_A = Z_L$. Figure 33 (c) shows the power contour at reference plane B of Figure 33 (b).

2. Considering only the series inductor, ($Z_c = 0$), the impedance at reference plane A will be transformed into $Z_A = Z_i + Z_L$, where $Z_i = j\omega L$.

For a constant value of L , the admittance of Z_A will change with the frequency; therefore, the power contour will appear to rotate around the circle of constant resistance $R_L = R_{LO} = R_{opt}/\rho$. Figure 34 (b), shows the circuit required to compensate the effect introduced by the series inductor L . The impedance transformation at reference plane B of Figure 34 (b), is $Z_B = Z_L - Z_c$. Figure 34 (c) shows the power contour rotation versus frequency, along the constant resistance circle $R_L = R_{opt}/\rho$, at reference plane B.

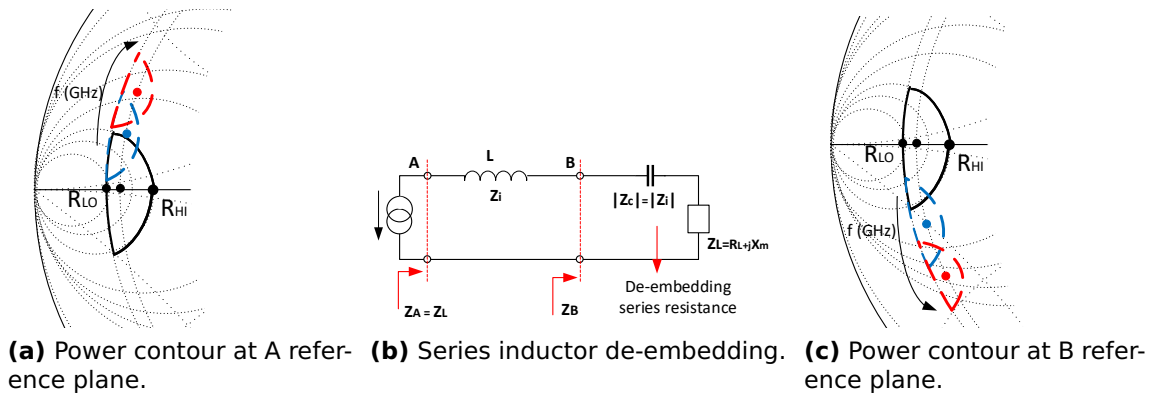


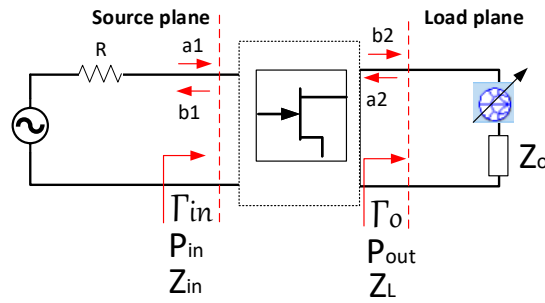
Figure 34. Rotation of the power contour along the resistance constant circle ($R_L = R_{opt}/P$).

3.3 Load-Pull systems

The previous section discussed the effect of different load lines on the output power of a nonlinear device. In practice, the LP is the technique used to physically change the reflection coefficient (Γ_o) at the output reference plane of the device while measuring different parameters such as input and output power (P_{in} , P_o), (PAE), (η_{DE}), ($ACPR$), and others. They are commonly represented in the Smith Chart as LP contours versus the variation of the output impedance of the device (Z_L),

The reflection coefficient (Γ_o) seen by the DUT is given by equation (52), where Z_o is the characteristic impedance of the system in which the DUT is going to be measured),

a_2 and b_2 are the incident and reflected waveforms at the output port of the DUT.



$$\Gamma_o = \frac{a_2}{b_2} = \frac{Z_L - Z_o}{Z_L + Z_o} \quad (52)$$

$$Z_L = Z_o \frac{1 + \Gamma_o}{1 - \Gamma_o}$$

Equation (52), shows that different values of (Γ_o) are obtained by sweeping the magnitude and phase of the ratio $\frac{a_2}{b_2}$, where b_2 is the device output waveform toward the load (Z_L), while a_2 is the waveform generated by the LP systems toward the device. LP are mechanisms to generate the waveform a_2 . They are classified according to the method by which the load is synthesized which is the same as how they generate the a_2 waveform.

The input power at the DUT port is given by equation (53).

$$P_{in} = |a_1|^2 - |b_1|^2$$

$$P_{in} = |a_1|^2(1 - |\Gamma_{in}|^2), \quad (53)$$

where a_1 and b_1 are the incident and the reflected waveforms at the DUT input port and Γ_{in} is the reflection coefficient at DUT input plane.

The output power at DUT port is given by the equation (54)

$$P_o = |b_2|^2 - |a_2|^2$$

$$P_o = |a_2|^2(1 - |\Gamma_o|^2) \quad (54)$$

The output impedance can be synthesized either using passive (passive tuners), active elements, or both. In the next section, the characteristics, advantages, and disadvantages of them will be discussed.

3.3.1 Passive LP

Passive tuner systems are the most common because of their simplicity and versatility. First, the impedance is generated, by changing the reflection coefficient of the impedance controlling element, such as a passive tuner Ghannouchi and Hashmi (2013). Figure 35 shows a common setup system used to measure the device under different load values, where a calibrated VNA captures the incident and reflected waveforms at the input and output reference plane of the device. For achieving the LP functionality, the tuner and signal generators, bias tees, isolators, drivers, couplers are used in the setup system.

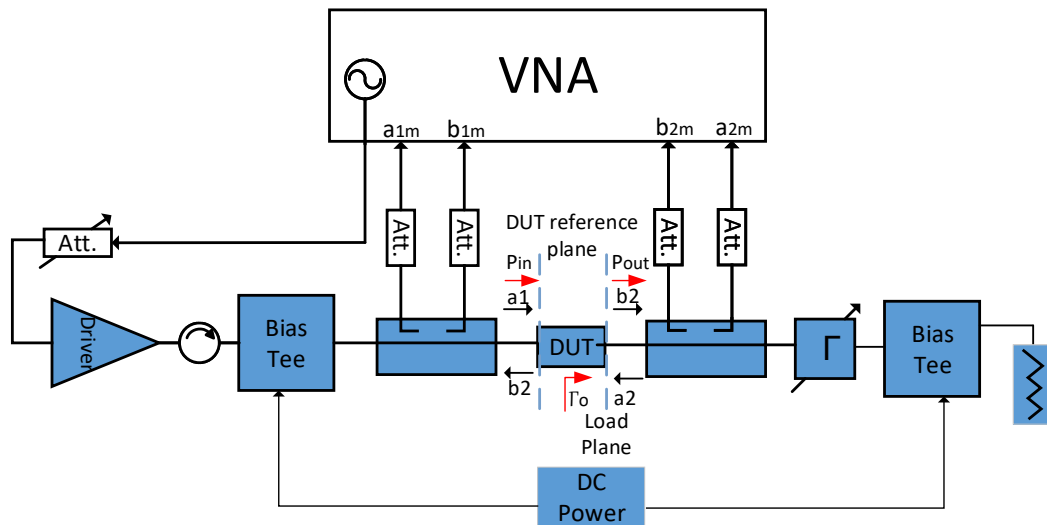


Figure 35. Setup to measure a nonlinear device with real-time LP system.

3.3.1.1 Electromechanical Tuner (EMT)

The impedance can be synthesized using the passive tuner of Figure 36 (a), which consists of a probe/ stubs/ slugs and a slotted transmission line, where the vertical movement of the probe changes the reflection coefficient magnitude ($|\Gamma_o|$), which increases as it gets closer to the transmission line. The horizontal movement of the probe changes the phase of Γ_o . This passive tuner is known as an EMT. They typically have a wide matching range.

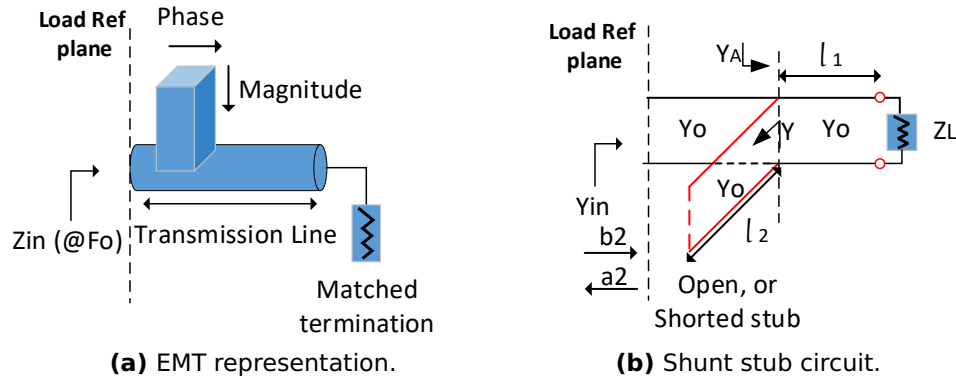


Figure 36. Electromechanical tuner (EMT).

To analyze the impedance changes with the vertical and horizontal movement of the probe, the circuit of Figure 36 (b) is used. It consists of a single open-circuited or short-circuited length (l_2) of transmission line (a stub), connected in parallel with the transmission feed line at a distance (l_1). The proper length of an open or shorted transmission line can provide any desired value of reactance or susceptance. These two degrees of freedom can be used to match an arbitrary load impedance to any feed line, Pozar (2004). The input admittance (Y_{in}) of Figure 36 (b) is given by:

$$Y_{in} = Y + Y_A, \quad (55)$$

where Y_A is the input admittance of a terminated transmission line of length l_1 , considering a lossless transmission line is:

$$Y_A = Y_o \frac{Y_L + jY_o \tan(\beta l_1)}{Y_o + jY_L \tan(\beta l_1)} \quad (56)$$

the admittance of a lossless transmission line ended in a short circuit is:

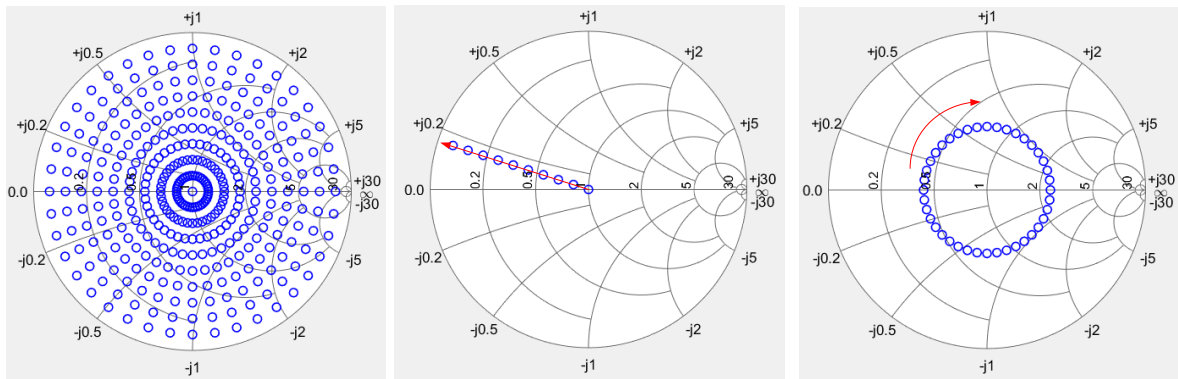
$$Y = -jY_o \cot(\beta l_2) \quad (57)$$

where $\beta = 2\pi/\lambda$, therefore Y , depends on the frequency, the length (l_2) and the characteristic admittance of the transmission line (Y_o), the input reflection coefficient (Γ_{in})

is given by:

$$\begin{aligned}\Gamma_{in} &= \frac{a_2}{b_2} = \frac{Y_o - Y_{in}}{Y_o + Y_{in}} \\ &= \frac{Y_o - (Y_A + Y)}{Y_o + Y_A + Y}\end{aligned}\quad (58)$$

From equation (58), it is observed that Γ_{in} depends on the frequency, the load admittance Y_L , the characteristic admittance of the transmission line (Y_o) and the length of the stub (l_2), the distance from the load to the stub (l_1). Keeping the operation frequency constant, and varying l_1 , and l_2 properly, the whole Smith Chart can be covered as Figure 37 (a) shows.



(a) A representation of an EMT in a matched state. **(b)** Vertical movement of the probe/stub. **(c)** Horizontal movement of the probe/stub.

Figure 37. Generic representation of the reflection coefficients generated with EMT.

Figure 37 (b), shows the reflection coefficients (Γ_{in}), generated by the EMT, for a constant frequency, while the stub/probe is moving vertically toward the feed transmission line, changing only the magnitude of Γ_{in} . Figure 37 (c) shows Γ_{in} when the probe is moving in the horizontal direction along the central conductor, which only affects the phase of it.

3.3.1.2 Electronic Tuner (ETS)

The electronic tuner can change the matching properties electronically. These electronic circuits can be based on either varactors or PIN diodes. The diode-based ETS synthesizes the reflection coefficient by varying the impedance state of several PIN

diodes connected in parallel and placed in a precise manner along a transmission line, Ghannouchi and Hashmi (2013).

The selection of the tuner will depend on their advantage for specific applications. For example, due to the miniature size of ETS, the lack of mechanical vibration, its often used on-wafer applications, but they have unpredictable impedance at low frequency, whereas the EMT is a low pass and presents 50Ω to the DUT; therefore, EMT is commonly used in on-wafer application for frequency below 0.8 GHz, after performing appropriate vibration tests.

The passive LP can deal with high power, and the modern LP can synthesize very low impedance, which is closed to the edge on the Smith Chart.

3.3.1.3 Non-real-time, and real-time LP systems

In order to reduce the losses introduced by cables and components between the DUT and the tuners, the ideal location of a passive tuner should be next to the DUT as shown in Figure 38, guaranteeing that it directly observes the maximum reflection coefficient synthesized by the tuners.

This measurement is known as a non-real-time LP system, where it is not possible to directly determine the impedance or output power at DUT reference planes. A priori characterization of the tuner is required, and a de-embedding procedure must be applied to shift the measurements reference planes to the DUT planes, while in the real-time LP system from Figure 35, the incident and reflected waveforms at the DUT ports are measured directly. Consequently, the output power is determined each time the reflection coefficient of the tuner changes.

The accuracy of the measurements obtained with the non-real-time LP systems will rely on the tuners' repeatability and stability. Nonetheless, they are used when a high reflection coefficient is needed. Their main disadvantage is that the systems are slower in terms of speed than the real-time LP systems shown in Figure 35, which on the contrary, will synthesize lower reflection coefficients than the maximum possible reach by the passive tuner.

However, several solutions to use the real-time LP system, when a high reflection coefficient is required, have been proposed in state of the art. For example, in Ferrero

et al. (2006), and Teppati *et al.* (2008), the authors designed an ultra-low loss directional coupler, which is placed at the DUT output port in a real-time LP system, synthesizing a high reflection coefficient without losing the tuner capabilities. These systems provide better performance in terms of accuracy, stability, repeatability, speed, and easier to implement than the rest of the tuners.

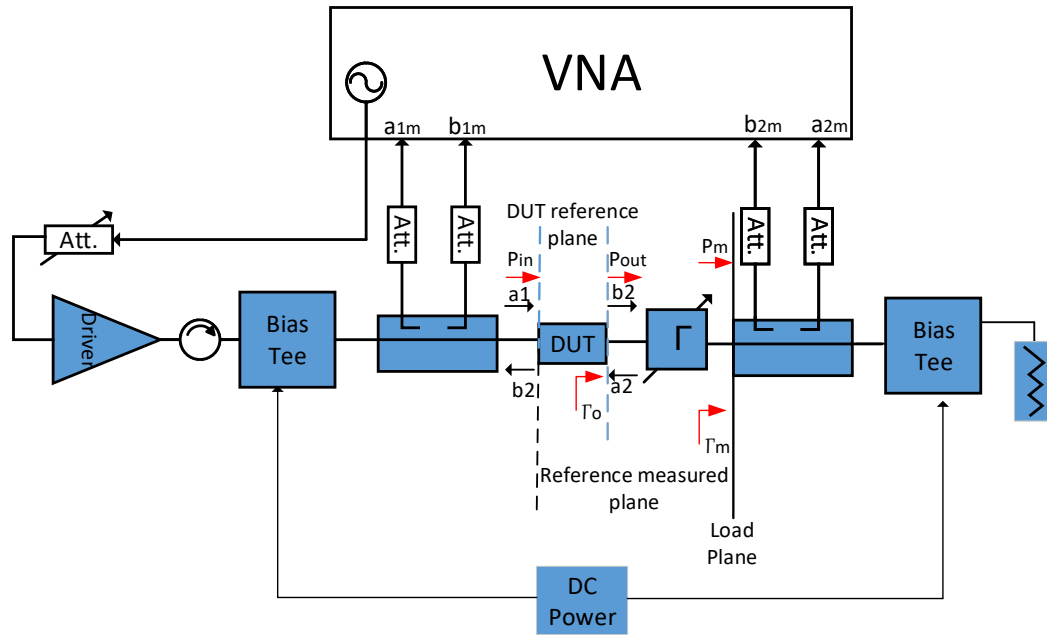


Figure 38. Non-real-time LP systems setup.

3.3.2 Active LP

The passive LP systems provide the impedance directly from the passive tuners, but they cannot synthesize a high reflection coefficient due to the losses introduced by the cables and components between the DUT and the passive tuners. This is a drawback for PA characterization or design, where a high reflection coefficient is required. The active LP system was first introduced by Takayama (1976), where two signals of the same frequency are simultaneously applied to the input and output of the DUT. Thus, overcome the inherent losses of a passive system by injecting a signal (a_2) into the DUT output plane (reflected waveform of the DUT), which is combined with the output signal (b_2) of the DUT, emulate a load. They can cover the full Smith Chart by adequately changing the phase and amplitude of a_2 .

There are three main active LP system configurations to generate a_2 : closed-loop,

feed-forward, and open-loop. In the closed-loop LP system, also known as feedback, the desired reflection coefficient is emulated by taking samples of the output signal and modifying them appropriately before feeding them back into the DUT. In the feed-forward or split-signal load-pull, the input feed signal is split into two parts, with one introduced at the input port of the DUT, the other one is forwarded to the LP, which changes the amplitude and phase of the reflected signal (a_2) to generate the desired reflection coefficient properly. Finally, the open-loop LP is very similar to the feed-forward, but instead of using the same source to generate the excitation signal for the DUT and its reflected waveform, the open-loop used two different sources to generate both signals.

3.3.2.1 Closed-loop active LP system

Figure 39 (a) shows a diagram that explains the concept of the reflection coefficient synthesis in an ideal closed-loop active LP system. Figure 39 (b) shows the block diagram of the closed-loop LP, where a circulator or coupler are used to send the output signal b_2 to a variable attenuator, which combined with the loop amplifier, adjust the reflected waveform amplitude ($|a_2|$). In addition, a phase shifter modifies its phase in order to emulate the reflection coefficient (Γ_o) at the output DUT plane.

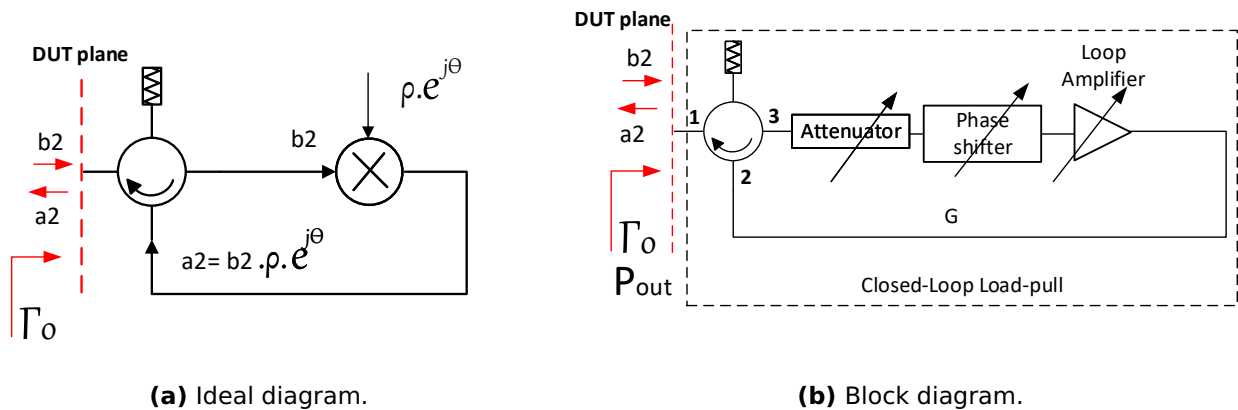


Figure 39. Closed-loop active LP system.

From Figure 39 (a) is noticed that the reflection coefficient Γ_o seen by the DUT at its output port is given by:

$$\Gamma_o = \frac{a_2}{b_2} = \frac{b_2 \rho e^{j\theta}}{b_2} = \rho e^{j\theta} \quad (59)$$

where a_2 is a phase shifted, amplified version of b_2 , and ρ and θ are the desired amplitude and phase of Γ_o , respectively. Equation (59) shows one of the most important feature of the closed-loop LP system: the independence of the drive level, thus keeping constant the emulated load.

Equation (60) is the Γ_o obtained when the circulator, which is part of the closed-loop LP system shown in Figure 39 (b), is considered ideal, (this means that a_2 and b_2 will not experiment change when passing through it) :

$$\Gamma_o = \frac{Gb_2}{b_2} = G, \quad (60)$$

where G is the complex Gain of the feedback loop, which can theoretically take any value, but high amplitudes should be avoided to prevent oscillations in the closed-loop LP, which can destroy the DUT being characterized and also damage to the measurement system.

A solution to prevent the oscillations in the LP system is keeping the magnitude of G below one ($|G| < 1$). Suppose G is higher than the directivity of the circulator (S_{23}), an attenuated version of the reflected waveform a_2 (leakage) will pass into the closed-loop LP, which can cause the oscillations. Therefore, the loop amplifier Gain should never exceed the directivity of the circulator. In addition, the condition (61) must be satisfied to avoid instability in the system.

$$|\Gamma_{DUT}||\Gamma_o| < 1 \quad (61)$$

3.3.3 Envelope LP systems

A new active LP system to avoid the oscillations that can take place in a closed-loop LP system is presented for the first time in Williams *et al.* (2004), where the closed-loop is performed in baseband. Therefore, the synthesized impedance is independent of the drive signal level. This system is named envelope LP system, and its scheme is shown in Figure 40. Where the emulated reflection coefficient (Γ_o) at the DUT plane is

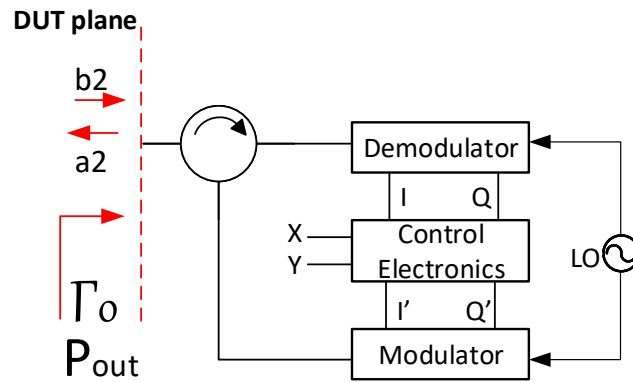


Figure 40. Envelope LP system.

fixed by the electronic control:

$$\Gamma_o = X + jY \quad (62)$$

It is noticed that:

$$\Gamma_o = \frac{a_2}{b_2} = \frac{I' + jQ'}{I + jQ}, \quad (63)$$

being I, Q the in phase and in-quadrature baseband components of the DUT output signal, and I', Q' , are the necessary baseband components of the injected signal a_2 , to obtain the desired reflection coefficient $X + jY$.

The required I' and Q' components are easily derivated from (62) and (63):

$$I' = X \times I - Y \times Q \quad (64)$$

$$Q' = Y \times I + X \times Q \quad (65)$$

The electronic circuit presented in Williams *et al.* (2004) is made with analog multipliers and op-amp to perform the equations (64) and (65), while two DC sources are used to generate the signals X and Y , therefore any load can be synthesized. Moreover, replacing DC sources with AWGs makes it possible to perform power and load changes for each measurement. Furthermore, Pin-Pout measurements can be done in one period of an amplitude-modulated signal used as a stimulus. At the same time, the emulated load is kept constant for the different input powers over the entire modulation bandwidth, considerably reducing the measurement time, making it suitable for the production environment.

In Williams *et al.* (2005a) the electronic circuit of the envelope LP system also re-

moves the DC offsets produced in the IQ modulator and demodulator, it obtains an expression that directly relates the reflection coefficient presented at the DUT output reference plane with the desired one and the transmission coefficients of the IQ modulator and demodulator. In Williams *et al.* (2005b), Williams *et al.* (2006), Alshali *et al.* (2019), the stability of the envelope LP is demonstrated, also good agreements between the theory and the results have been achieved.

3.3.4 Feed-forward and open-loop LP systems

Figures 41(a) and (b) show the feed-forward and open-loop LP systems, whose operating principles are the same, but the feed-forward LP system uses the same source to drive the DUT simultaneously, and the reflected wave a_2 at the output port of the DUT at a specified frequency, while the open-loop LP system uses independent sources to generate both waveforms. The feed-forward system was first introduced by Takayama (1976) to characterize a GaAs FET under large-signal.

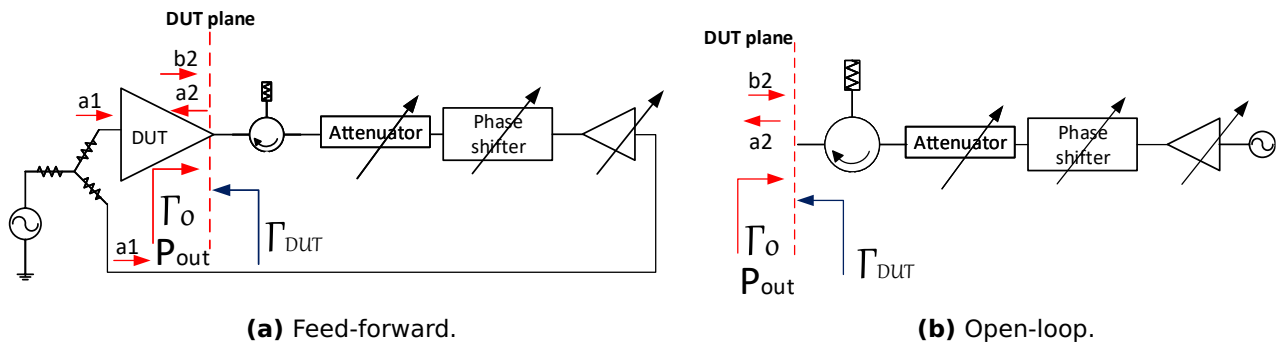


Figure 41. Active LP.

A large-signal transistor scattering parameters with a nonlinear behavior (as is the case of a transistor operating in class C) differ from the S-parameters extracted with a small signal. However, S_{11} and S_{21} are almost the same because the transistor operates normally (the signal is injected at the input port). Nevertheless, the S_{22} and S_{12} are measured by the reflection coefficient at the output port and transmission coefficient at the input port when the signal is injected at the output port (a_1 is equal to zero), which is not the regular operation of the DUT; therefore they are incorrect.

In Van Der Puije and Mazumder (1978) the large-signal characterization was done by simultaneously driving the input and injected signals into the DUT ports (the two

signal method). The definition of S-parameters can be expressed more conveniently to explain this method, in the form shown in equations (66) to (69).

$$\frac{b_1}{a_1} = S_{11L_s} + S_{12L_s} \frac{a_2}{a_1} \quad (66)$$

$$\frac{b_2}{a_1} = S_{21L_s} + S_{22L_s} \frac{a_2}{a_1} \quad (67)$$

$$\frac{b_1}{a_2} = S_{12L_s} + S_{11L_s} \frac{a_1}{a_2} \quad (68)$$

$$\frac{b_2}{a_2} = S_{22L_s} + S_{21L_s} \frac{a_1}{a_2} \quad (69)$$

From equations (66) to (69) it can be observed that if $|a_1|$ and $|a_2|$ are constant, b_i/a_j ; ($i, j = 1, 2$), represent a circle in the plane b_i/a_j ; ($i, j = 1, 2$) as a function of $\angle a_2/a_1$ (difference angle between the injected signals), and center in S_{ij} , therefore b_i/a_j can be measured using a VNA as a function of $\angle a_2/a_1$, and the S-parameters under large-signal (S_{ijL_s}) will be determined by locating the center of the circles, as shown in Figures 42 [a-d]. From Figures 41 (a) and (b) it is noted that the amplitude of a_2 can be adjusted to any value by the variable attenuator, while the phase is changed by the phase shifter, simulating different load reflection coefficients at the output port (equation (70) deduced from equation (69)).

$$\Gamma_o = \frac{1}{S_{22L_s} + S_{21L_s} \frac{a_1}{a_2}} \quad (70)$$

For the feed-forward LP system the equation (70), can be rewritten as:

$$\Gamma_o = \frac{1}{S_{22L_s} + \frac{S_{21L_s}}{G}} \quad (71)$$

$$a_2 = Ga_1, \quad (72)$$

where G is the complex Gain of the loop shown in Figure 41 (a).

It is evident from equations (70) and (71), that any load can be synthesized by changing the magnitude and the phase reflected wave a_2 or the complex Gain G for the feed-forward LP; the minimum reflection coefficient will be $\Gamma_{o_{min}} = 0$, which is reached

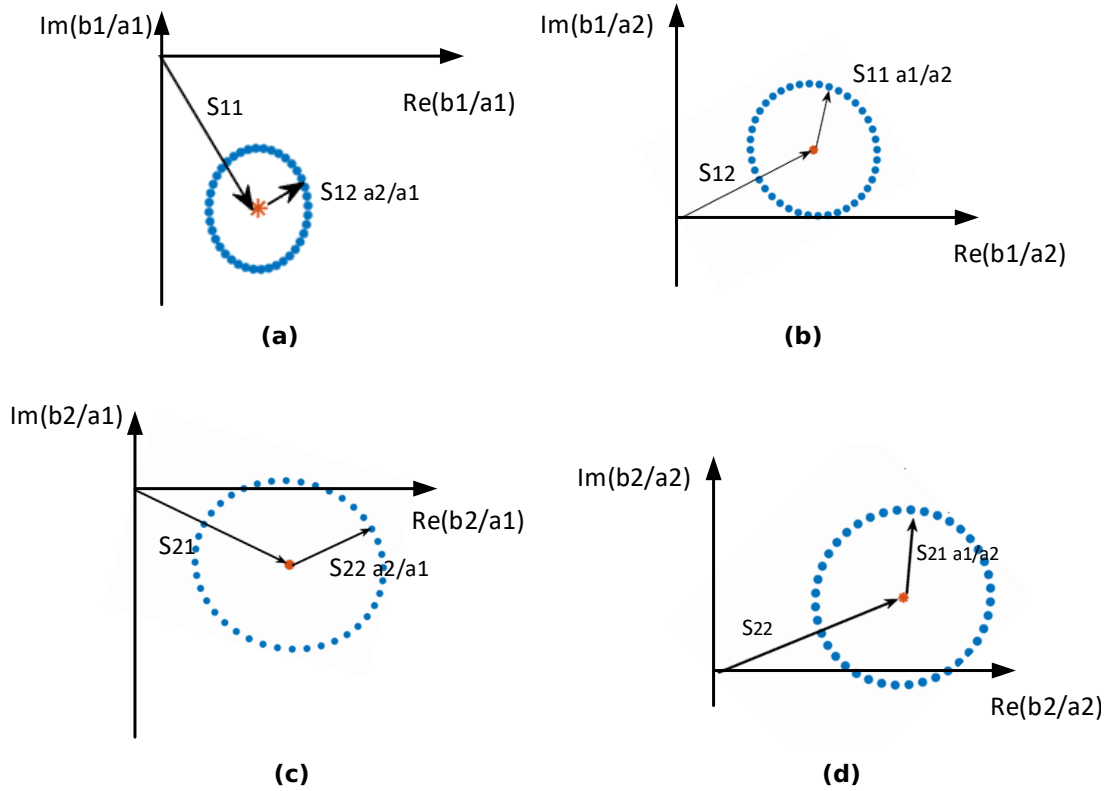


Figure 42. Circles in the plane bi/aj as function of $\angle a_2/a_1$ and center S_{ij} .

when the open-loop source is completely off $G = 0$ or $a_2 = 0$, while the maximum value $\Gamma_{o_{max}} = 1/S_{22}$ is reached when G or a_2 are very high, a DUT operating in stable condition always possess $S_{22} \leq 1$, therefore $\Gamma_{o_{max}}$ can cover the entire Smith Chart.

The reflection coefficient synthesizes with feed-forward and open-loop LP systems, which are shown in equations (70) and (71), respectively, also depends on $S_{ij_{L_s}}$ of the DUT, which changes with excitation, bias, and impedance environment at the ports. Therefore $S_{21_{L_s}}$ and $S_{22_{L_s}}$ will change with any variation of LP components, thereby necessitating the recalculation of G or a_2 , based on the selected active load-pull. Thus, the process to emulate a load with these active LP systems is an iterative algorithm, which makes it slow to converge, but they are suitable for high power application or when a high reflection coefficient is required (which is the case of harmonic termination for a transistor operating in class C).

The feed-forward LP system is stable as long as the complex Gain G remains less than the combination of $S_{12_{L_s}}$ of the DUT and the isolation of the splitter (Figure 41 (a)). Therefore the output and input of the active feed-forward LP are entirely isolated,

making it independent of the DUT $S_{22_{L5}}$, thus decoupling the stable operation of the active feed-forward load-pull system from the DUT stability criterion. On the other hand, the main advantage of the open-loop LP system is its absolute stability due to the absence of a loop attached to the DUT, eliminating any possibility of oscillations, which is the main disadvantage of closed-loop LP. Since there are no restrictions on the phase and magnitude of a_2 , it can be increased as much as needed.

The behavior of the reflection coefficients generated by the classic feed-forward and open-loop LP systems matched at 50Ω shown in Figures 41 (a), (b) are drawn in Figure 37 (a), where it is observed that the LP initialize at $\Gamma_o = 0$. Therefore the coefficients synthesized by them are distributed around the center point of the Smith Chart ($\Gamma_o = 0$, 50Ω impedance). For PAs with a substantial mismatch, it is mandatory to avoid certain phases of the reflection coefficients during the measurements, destroying them. Figure 43 shows the area in the Smith Chart where the synthesized reflection coefficients may lie to find the optimal output matching network and the region that must be avoided to prevent damage to the DUT.

Additionally, it is notable that the LP systems terminated with 50Ω , used to characterize transistors with a high mismatch, have some disadvantages:

1. Time and power consumed to find the optimal load. As observed from Figure 43, the hypothetical region where the appropriate reflection coefficient is located (green area) far from the Smith Chart center, therefore the reflection coefficients will cover almost the whole Smith Chart in order to reach the wanted load.
2. Failure to produce a fine grid in the region of interest, consequently the optimal reflection coefficient might not be found.
3. Due to the high magnitude required, a minimum change in the phase can damage the DUT. For example, figure 43 shows the region (red area) that must be avoided preventing damage to the DUT. Notably, the optimal and damaged areas reach the same high amplitudes of the reflection coefficient. Therefore only changes in the phase can cause movement from one region to another one.

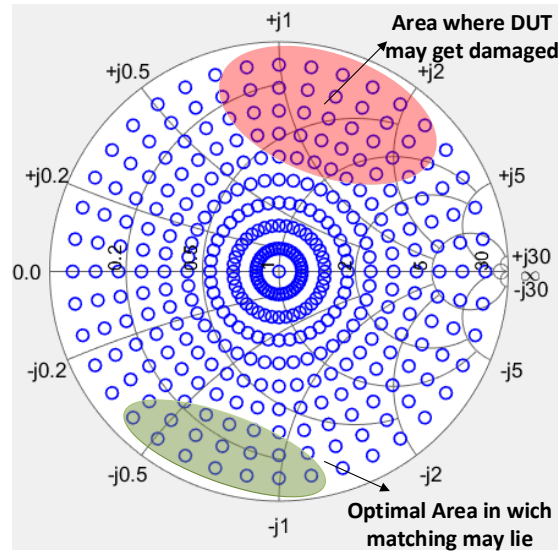


Figure 43. Example of optimal and avoidable areas in the Smith Chart to characterize an hypothetical transistor.

3.3.4.1 Improving the Feed-forward and open-loop LP systems

In Bouysse *et al.* (1994) a variant of the classical feed-forward and open-loop LP systems is presented. The new system consist of a sliding *short* connected to the central wire of a directional coupler and the 50Ω source to the coupled port as shown in Figure 44 (a). When the source E_g is off the reflected wave a_2 is:

$$a_2 = b_2 t^2 e^{2j(\theta+\psi)}, \quad (73)$$

where t , θ are the transmission coefficient and the delay of the central line of the coupler, ψ_i is the initial phase generated by the position of the sliding short, hence the Γ_{o_i} synthesized when $E_g=0$ is,

$$\Gamma_{o_i} = t^2 e^{2j(\theta+\psi_i)} \quad (74)$$

From equation (74) it is appreciable that the maximum value of Γ_{o_i} , is equal to the square of the transmission coefficient of the coupler used, the initial phase will be $2(\theta + \psi_i)$, the phase can be changed to any position of the blue circle shown in Figure 44 (b) by moving the sliding short.

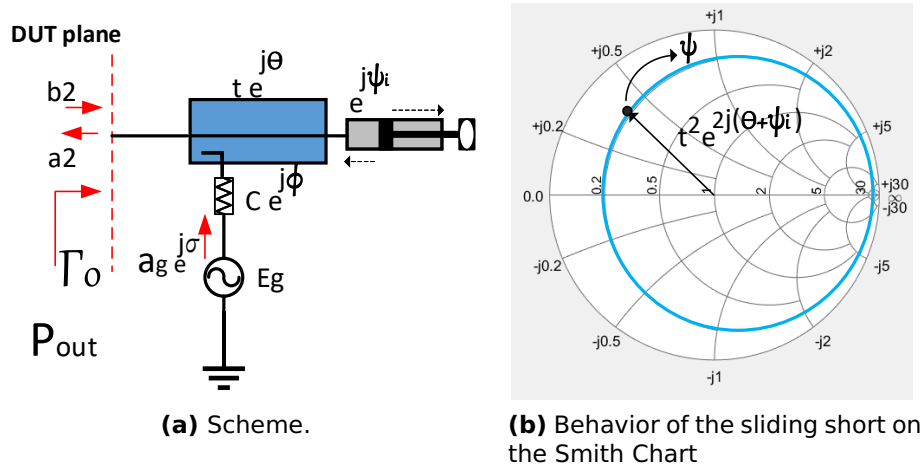


Figure 44. Enhanced feed-forward LP system.

When the source E_g is turned on the reflected wave a_2 is defined as:

$$a_2 = a_g C e^{j(\phi)} + b_2 t^2 e^{2j(\theta + \psi_i)} \quad (75)$$

where C and ϕ are the coupling factor, and the delay of the directive coupler, respectively, and a_g is the signal generated by the source E_g . Consequently, the reflection coefficient at the DUT output looking towards the load is shown in equation (76)

$$\begin{aligned} \frac{a_2}{b_2} &= \frac{a_g C e^{j(\phi + \sigma)} + b_2 t^2 e^{2j(\theta + \psi_i)}}{b_2} \\ \frac{a_2}{b_2} &= \frac{a_g C e^{j(\phi + \sigma)}}{b_2} + t^2 e^{2j(\theta + \psi_i)} \\ \Gamma_o &= \delta\Gamma + \Gamma_{o_i} \end{aligned} \quad (76)$$

where $\delta\Gamma$ are the reflection coefficients locus on Γ_{o_i} (see Figure 45), whose phases and amplitudes are changed by the magnitude a_g and phase σ of the signal generated by the source E_g . An important advantage of this new configuration of the feed-forward LP system is that it requires less power than the classic one. Knowing that the reflection coefficient obtained with the classic feed-forward LP is $\Gamma_o = \frac{a_2}{b_2}$, and using equation (76), the power ratio (R) between the sources of each system to generate the reflected

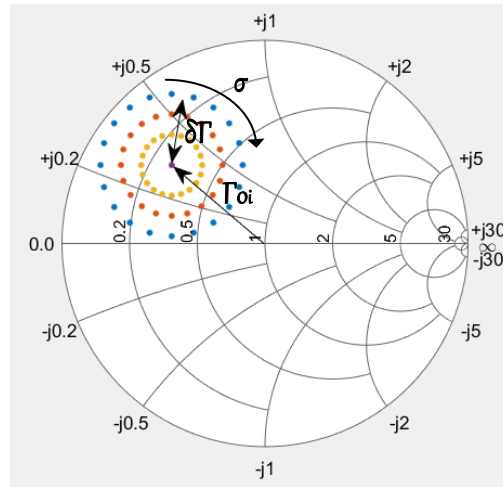


Figure 45. Behavior on the Smith Chart of the enhanced feed-forward LP system.

wave a_2 is given in equation (77):

$$\begin{aligned}
 a_g &= \frac{a_2 - \Gamma_{o_i} b_2}{C}, \quad a_2 = \Gamma_o b_2 \\
 \frac{a_g}{a_2} &= \frac{a_2 - \Gamma_{o_i} b_2}{\Gamma_o b_2 C} = \frac{\Gamma_o - \Gamma_{o_i}}{\Gamma_o C} \\
 R &= \frac{|a_g|^2}{|a_2|^2} = \frac{|\Gamma_o - \Gamma_{o_i}|^2}{|\Gamma_o|^2 |C|^2}
 \end{aligned} \tag{77}$$

Figure 46 shows the percentage of the power needed by the source of the enhanced feed-forward LP system compared with the classical system when a high reflection coefficient $\Gamma_o = 0.99$ is required. $R(\%)$ is computed for different coupling factors (from -12 dB to -3 dB). It is observed that minimizing the distance between Γ_o and Γ_{o_i} , will reduce the power required by the source E_g , where Γ_{o_i} is proportional to the transmission coefficient of the coupler (equation (74)). Therefore a higher value of Γ_{o_i} will require a coupler with lower losses.

From Figure 46 it is observed that by selecting a coupler with 6 dB of coupling factor and a transmission coefficient of -0.70 dB (which gives $\Gamma_{o_i} = 0.85$), the enhanced feed-forward LP system just uses a 7.96 % of the power needed by the classic LP system.

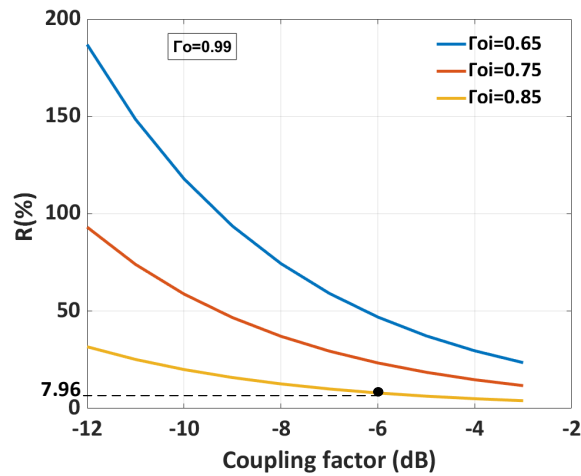


Figure 46. Comparing the power consumed by the classic and enhanced feed-forward LP systems.

3.3.5 Harmonic LP system

The LP system architectures shown above are used to emulate a desired reflection coefficient at the DUT output reference plane at the fundamental frequency, and the harmonic terminations are set to 50Ω or sometimes to an unknown and uncontrollable impedance. It is crucial to study the impact of the load terminations at harmonic frequencies to obtain optimum performance. It is well known that the efficiency of a device can be improved if a high reflection coefficient at $2f_o$ and $3f_o$ with appropriated phases are presented at the output of the device. These load terminations will reflect the associated RF power into the DUT. In Stancliff and Poulin (1979) a system capable of measuring and tuning the impedances at the fundamental and second harmonic of a microwave device is presented. Impedances are synthesized using a closed active tuner formed by a variable attenuator and line stretcher, allowing to change the signal's amplitude and phase, amplified and injected back to the DUT output through port three of a circulator-filter configuration. The stability of the tuner is guaranteed if the gain of the amplifier is less than the isolation between ports two and three of the circulator and less than the return losses of the DUT added to the tuner loop insertion loss. The power at the load is obtained indirectly by measuring the linear power difference between the incident and reflected waves at DUT output.

In Ghannouchi *et al.* (1991) an active LP system to characterize a Metal Semiconductor Field-Effect Transistors (MESFET) under different fundamental frequency, second, and third harmonic terminations is presented. The constant power contours at

f_0 and $2f_0$ in the complex plane of the reflection coefficient at f_0 (Γ_o) for chosen terminations at $2f_0$ (Γ_{2f_0}) and $3f_0$ (Γ_{3f_0}) are shown. It is experimentally demonstrated for the first time that the efficiency of the MESFET PA can be optimized by tuning the third harmonic impedance while keeping fixed the fundamental and second harmonic terminations for a given output power. Figure 47 shows the multiharmonic LP system, where the input excitation signals at f_0 , $2f_0$ and $3f_0$ are injected simultaneously through a three-way power combiner, this is a feed-forward active LP system, as can be observed from Figure 41 (a).

The measurement setup consists of two wideband six-port junctions located at the input (SP1) and output (SP2) of the device. At each output of SP2 a wideband three-way unequal power divider, with three band-pass filters centered, respectively, at f_0 , $2f_0$, $3f_0$ are used, the output of these filters are connected to a four channel power meter.

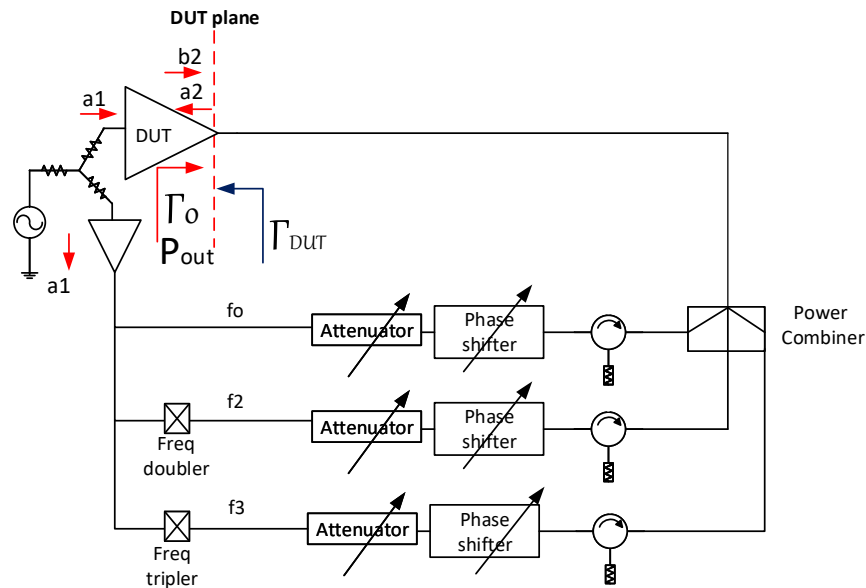


Figure 47. Multiharmonic active LP system using feed-forward configuration.

In Benedikt *et al.* (2000) a system with the capabilities to perform harmonic active LP and to measure the time domain waveforms of devices (LDMOS) up to 30 W is presented. The harmonic active LP is a feed-forward architecture, where a common CW generator is introduced into three branches; each one contains a variable amplifier and a phase shifter to emulate any impedance in the Smith Chart at f_0 , $2f_0$ and $3f_0$. A triplexer is used to inject the three signals simultaneously into the device output.

The measurement system has two couplers located at the input and output of the DUT to split the incident and reflected waves at both ports, which are measured with a Microwave Transition Analyzer (MTA). The time domain voltage and current waveforms are obtained by vector corrected the magnitude and phase measurements up to their fifth component at the reference plane of the device (package level). To provide a correct interpretation to the measurements at the intrinsic DUT planes (output current plane), the parasitic reactive elements of the packaged device and the output capacitance are removed from the time domain current and voltage waveforms measured by the system (this process is well known as de-embedded).

In Benedikt and Tasker (2002) an open, active harmonic LP (Figure 48) system is used to synthesize high reflection coefficients at harmonic frequencies as it is required to improve the amplifier efficiency.

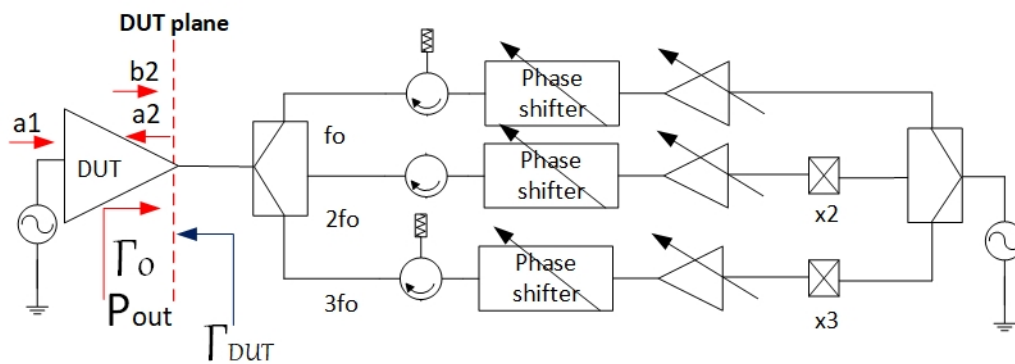


Figure 48. Open harmonic active LP system configuration.

The LP system is used in a time domain measurement setup, allowing to observe the voltage and current waveforms in the time domain at the intrinsic plane of the device as mentioned in Benedikt *et al.* (2000). Furthermore, the open-loop configuration guarantees the stability of the LP system for all reflection coefficients. This testbed can handle high power over a wideband using bias tees, two commercial 90° hybrids connected back to back.

The active harmonic LP requires an unpractical amount of power to synthesize a high reflection coefficient when the DUT to be characterized presents a low output impedance.

In Aboush *et al.* (2004), Aboush *et al.* (2005b), Aboush *et al.* (2005a) a Klopfenstein impedance transformer from 50Ω to 10Ω is used to reduce the power required for the harmonic active LP. The measurement setup is explained in Benedikt *et al.* (2000), Benedikt and Tasker (2002), and it is calibrated using a SOLT calibration until the coaxial connector and TRL shifts the reference planes into the extrinsic DUT planes. The Klopfenstein transformer provides a constant impedance over a broadband frequency without resonance, and its design equations are presented in Klopfenstein (1956).

3.3.6 Real-time multitone LP System

It has been demonstrated that the PA is more efficient when it works near or beyond the 1 dB compression point (P1dB), where it exhibits a nonlinear behavior and produces a distorted output signal increasing the spectral regrowth. Moreover, digital modulation techniques like Quadrature Amplitude Modulation (QAM) are very sensible to any change in phase or amplitude produced by the nonlinearity effects of the PA causing loss of information.

Different figures of merit characterize the PA linearity, e.g., Amplitude to Amplitude Modulation (AM-AM), Amplitude to Phase distortion (AM-PM), 3^{rd} , 5^{th} , Intermodulation Order (IMD), Carrier to Intermodulation (C/I), these are the most common measurements registered in the literature. These nonlinear effects can be compensated through some linearization scheme such as Digital pre-distortion (DPD). In Qiu *et al.* (2011) a linearity characterization of a millimeter Wave-GaN HEMTs is carried out using Vector Signal Generator (VSG), VSA, and Spectrum Analyzer. In Teyssier *et al.* (2014), Kahil *et al.* (2016) the characterization is done using multitone signals generated by an AWG with IQ modulation capabilities and Large-Signal Network Analyzer (LSNA). In Gillet *et al.* (2018) a Nonlinear Vector Network Analyzer (NVNA) fully calibrated is used with Unequal Space Multitone (USMT) and the VNA spectrum option to characterize the PAs or transistors, Gillet *et al.* (2018) represents an extension of Laurent *et al.* (2016) and Simb lie *et al.* (2017). The USMT guarantees that the frequencies of the intermodulation products be different from the input signal frequencies; this allows to know the exact power of each intermodulation product.

Other very used measurements for the PA designers are the source and LP mea-

measurements to find the optimum impedance at the fundamental frequency in the input and output of the DUT and the load harmonic terminations to get the desired waveform in the reference planes of the PA in order to increase the efficiency.

In this work, a testbed to characterize the linearity of transistor or PA under CW and multitone signals with different load conditions using a FOCUS Multi-Purpose Tuner (MPT) is presented. The baseband tones are generated through Universal Software Radio Peripheral (USRP) and an RF daughterboard. The generated signal is fed into PSG E8267D in order to up-convert the signal. The static AM-AM and AM-PM characteristics at the fundamental frequency, carrier to intermodulation, and LP measurements are obtained by measuring the incident and reflected waves from the DUT using the classical hardware of a VNA. In our research, we used a PNA-X 5245A, without the necessity of any nonlinear measurement options as in the case of Gillet *et al.* (2018) that uses an NVNA, and therefore the calibration procedure is more extensive.

3.4 The proposed testbed

This section describes the proposed testbed to characterize the DUT. Figure 49 shows a complete description of the setup.

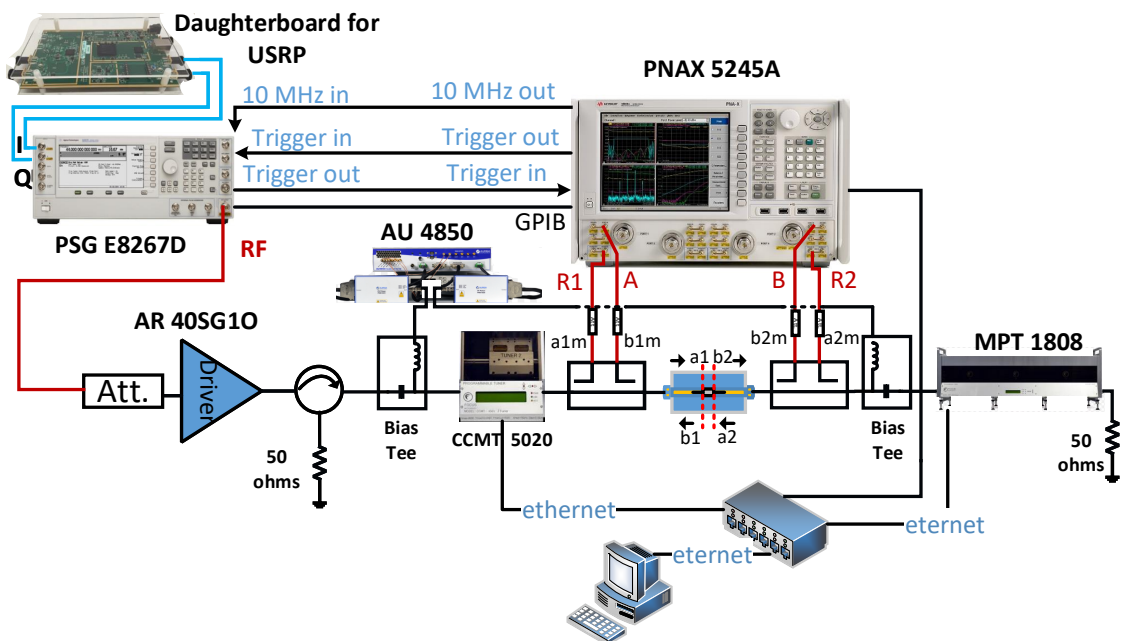


Figure 49. Testbed for linearity characterization.

It is important to highlight that this configuration can handle high power. It consists of an RF daughterboard and a USRP board used to generate the baseband tones. The tones are fed into the PSG E8267D to up-convert the signal. The PSG is configured as an external source in the VNA, and the synchronization between both is done using trigger signals and the 10 MHz clock signal. In addition, to protect the driver (AR 40SG10), a 20 dB attenuator is added to its input and an isolator to its output; this guarantees that the input level is less than 0 dBm, and no reflected signal is feedback into the output of the driver. External directional couplers with a coupling factor of 40 dB are used to measure the incident and reflected waves from the DUT. This fact implies that port one of the PNA-X is configured to bypass the internal coupler and measure the incident and reflected waves using an external coupler. For security, external attenuators are used in the PNA-X receiver inputs to avoid their saturation. The attenuation value must guarantee a signal level below -20 dBm (this is the value recommended by Keysight to guarantee that the receivers work in their linear region). A computer-controlled microwave tuner (FOCUS iCCMT 5020) and a FOCUS MPT 1808 generate the input and output impedances at the fundamental frequency at DUT planes. The whole system is controlled from a PC using the ethernet connection, while the USRP board is controlled by another PC that runs the GNU Radio Companion (GRC) development tool.

3.4.1 System calibration

In order to measure the static AM-AM, AM-PM, C/I, power contours, input and output spectrum measurements, and the optimum load impedance in the DUT planes, a previous calibration is necessary. A relative and power calibration is done to shift the reference planes to the DUT plane as shown in Pulido-Gaytán *et al.* (2016).

When the DUT is non-insertable a TRL calibration is required to obtain the error boxes (T_A and T_B), see Figure 50.

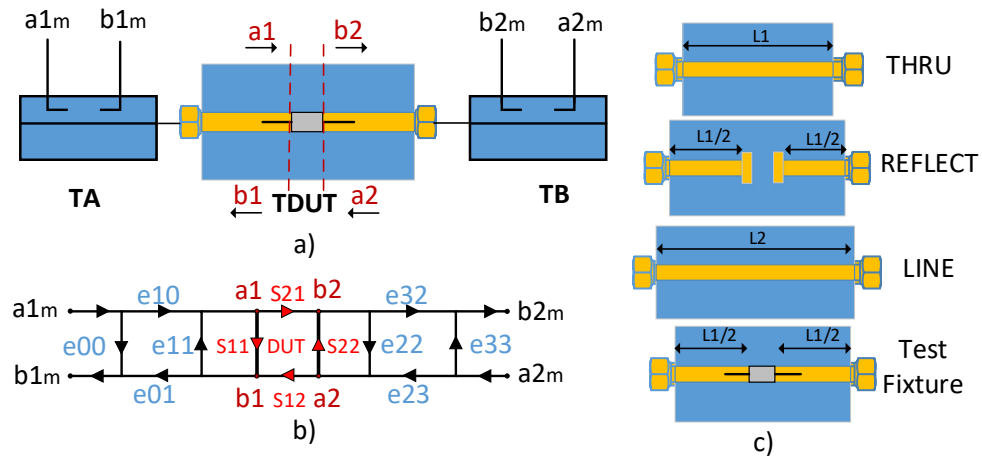


Figure 50. TRL calibration. a) PNA-X configuration, b) error matrices, c) calibration standards.

The measurements results can be defined as the multiplication T-parameters matrices: T_A , T_{DUT} and T_B , where T_{DUT} is the T-parameter of the DUT and can be computed as:

$$T_m = T_A T_{DUT} T_B \quad (78)$$

$$T_{DUT} = T_A^{-1} T_m T_B^{-1} \quad (79)$$

Once the error boxes (T_A , T_B) are computed as indicated in Appendix 1, a set of Short-Open-Load and power calibrations are done to obtain the unknown T_z error box Ferrero *et al.* (2006). This error box appears when the incident and reflected output waves (b_t and a_t respectively) are measured by the input receivers, as seen in Figure 51. These calibrations correct receiver response errors and remove cable and fixture effects as demonstrated in Pulido-Gaytán *et al.* (2016).

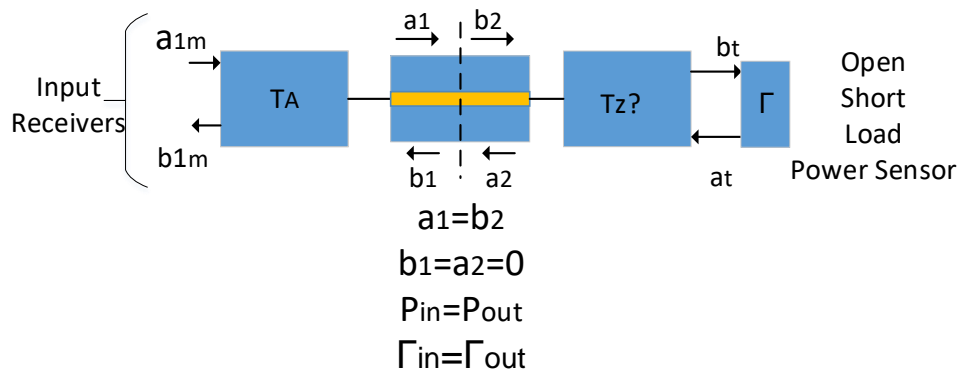


Figure 51. Short-Open-Load (SOL) and absolute calibrations.

$$\begin{bmatrix} b_1^m \\ a_1^m \end{bmatrix} = D_x T'_M \begin{bmatrix} a_1 \\ b_1 \end{bmatrix} \quad (87)$$

a_{1_m} and b_{1_m} are obtained from equation (87) :

$$a_1^m = D_x (m_{11}b_1 + m_{12}a_1) \quad (88)$$

$$b_1^m = D_x (m_{21}b_1 + m_{22}a_1) \quad (89)$$

a_1 and b_1 can be expressed as indicated equations (90)-(91):

$$a_1 = D_x \left(\frac{b_1^m - m_{11}b_1}{m_{12}} \right) \quad (90)$$

$$b_1 = D_x \left(\frac{a_1^m - m_{22}a_1}{m_{12}} \right) \quad (91)$$

An expression for a_1 is obtained by evaluating equation (91) into (90):

$$a_1 = \frac{m_{11}a_1^m - m_{21}b_1^m}{D_x(\Delta_M)} = a_1^m \left(\frac{m_{11} - m_{21}\Gamma_{in}^m}{D_x(\Delta_M)} \right) \quad (92)$$

Using equations (84)-(86), Γ_{in} is obtained:

$$\Gamma_{in} = \frac{b_1}{a_1} = \frac{m_{12} - \Gamma_{in}^m m_{22}}{\Gamma_{in}^m m_{21} - m_{11}} \quad (93)$$

where Γ_{in}^m is the input raw reflection coefficient measured by the VNA.

The input power is deduced by evaluating equations (92)-(93) in equation (80)

$$P_{in} = (a_1^m)^2 \left(\frac{|m_{11} - m_{21}\Gamma_{in}^m|^2}{|D_x|^2 |\Delta_M|^2} \right) \left(1 - \frac{|m_{12} - \Gamma_{in}^m m_{22}|^2}{|\Gamma_{in}^m m_{21} - m_{11}|^2} \right) \quad (94)$$

Δ_M is the determinant of matrix T'_M .

In Appendix 2 the calibration procedure to obtain the term $(D_x)^2$ from equation (94), Γ_{out} , P_{out} , and G is detailed.

3.4.2 Signal generation

Characterization of the transistors or PAs under multitones conditions were performed using a Low Frequency Transmitter (LFTX) daughterboard from Ettus Research. The LFTX can generate a tone from 1 to 30 MHz, two or more tones of different frequencies, or an I/Q signal simultaneously and is programmed using a software defined radio development tool (GNU radio) running on Linux Operation system (OS).

The multitones are generated using a procedure similar to these employed to generate an Orthogonal Frequency-division Multiplexing (OFDM) symbol; this means using the Inverse Fast Fourier Transform (IFFT) technique (which is available as a function block in GRC). Since each tone represents a subcarrier, defining a frequency spacing and a vector with a value of one in the positions where we want to generate multiples of the first subcarrier generated when the IFFT is applied to this vector.

$$x(n) = \frac{1}{N} \sum_{k=0}^{N-1} \mathbf{X}(k) \exp\left(\frac{j2\pi nk}{N}\right) \quad (95)$$

$$x(n) = \mathbf{W}^H \mathbf{X}(k), \quad k, n = 0, 1, 2, \dots, N-1 \quad (96)$$

Equation (95) shows the IFFT formula, while equation (96) shows the equivalent in matrix notation. The IFFT can be represented as the product of the vector $\mathbf{X}(k)$ and a complex matrix \mathbf{W} defined in equation (97), where N is the number of bins on the IFFT. In OFDM $\mathbf{X}(k)$ is a vector of complex symbols which are the result of a digital modulation as Binary Phase Shift Keying (BPSK), Quadrature Phase Shift Keying (QPSK), M-ary Quadrature Amplitude Modulation (MQAM). The IFFT can be represented as the

product of a vector $\mathbf{X}(k)$ and a complex matrix \mathbf{W} .

$$\mathbf{W} = \begin{pmatrix} 1 & 1 & 1 & \dots & 1 \\ 1 & e^{-j\frac{2\pi}{N}} & e^{-j\frac{4\pi}{N}} & \dots & e^{-j\frac{2\pi(N-1)}{N}} \\ \vdots & \vdots & \vdots & \ddots & \vdots \\ 1 & e^{-j\frac{2\pi(N-2)}{N}} & e^{-j\frac{4\pi(N-2)}{N}} & \dots & e^{-j\frac{2\pi(N-1)(N-2)}{N}} \\ 1 & e^{-j\frac{2\pi(N-1)}{N}} & e^{-j\frac{4\pi(N-1)}{N}} & \dots & e^{-j\frac{2\pi(N-1)(N-1)}{N}} \end{pmatrix} \quad (97)$$

Figure 53 shows the GNU radio blocks that describes the process needed to generate the baseband tones.

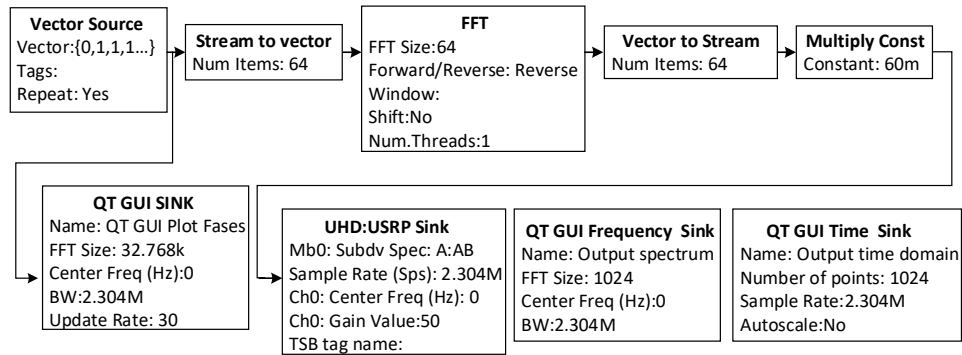


Figure 53. GNU radio blocks to generate the baseband tones.

3.5 Measurement Results

In the following subsections the measurement results obtained from one tone signal and multitone signal are discussed.

3.5.1 One tone measurement

In this section, the GaN FET CGH40010F is the DUT, and the experimental results correspond to the characterization of the DUT at 2.0 GHz. Figure 54 shows the output powers at the fundamental frequency and the second harmonic, carrier to second harmonic, and Gain. These measurements are useful in the development of the memoryless nonlinear models Schreurs *et al.* (2008). It is important to highlight that these measurements are done in the transistor plane, using the standard VNA, not requiring any additional options regarding the nonlinear measurements as reported in Gillet

et al. (2018). Figures 55 and 56 show the static AM-AM, and AM-PM, respectively, at different bias points.

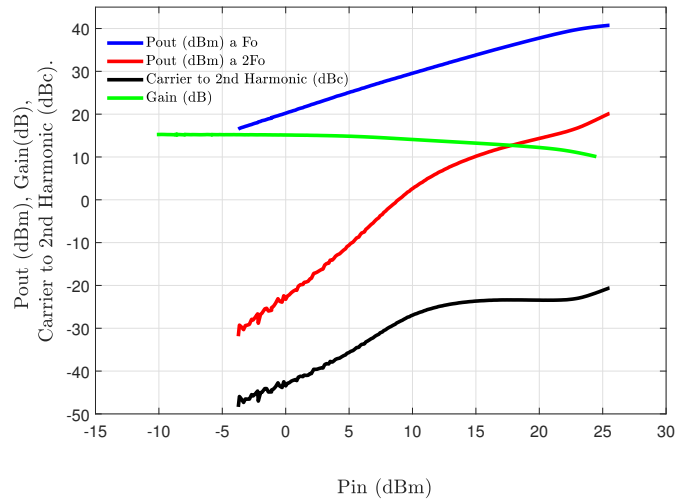


Figure 54. AM-AM, Gain and 2nd harmonic distortion of CGH40010F transistor.

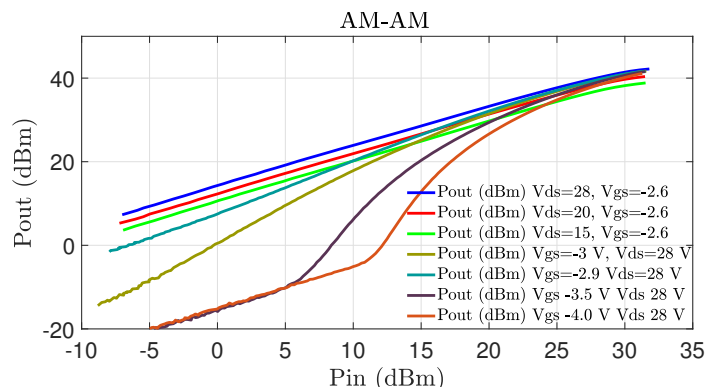


Figure 55. AM-AM for different quiescent points of CGH40010F transistor.

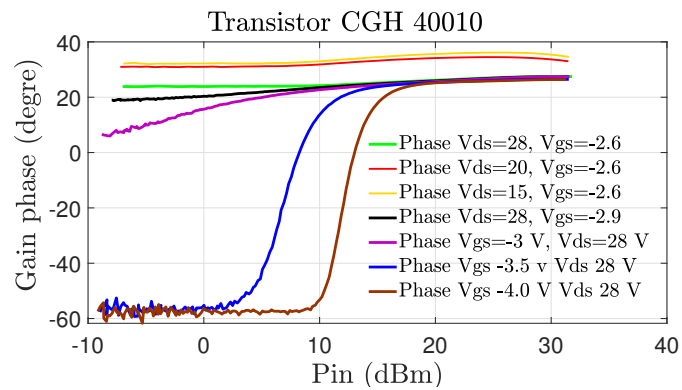


Figure 56. AM-PM for different quiescent points of CGH40010F transistor.

Figure 57 shows the output power contours of CGH40010F at 2 GHz, the optimum

impedance found in this frequency ($17.18+9.18i \Omega$), with a quiescent point $V_{GS} = -2.6 \text{ V}$, $V_{DS} = 26 \text{ V}$.

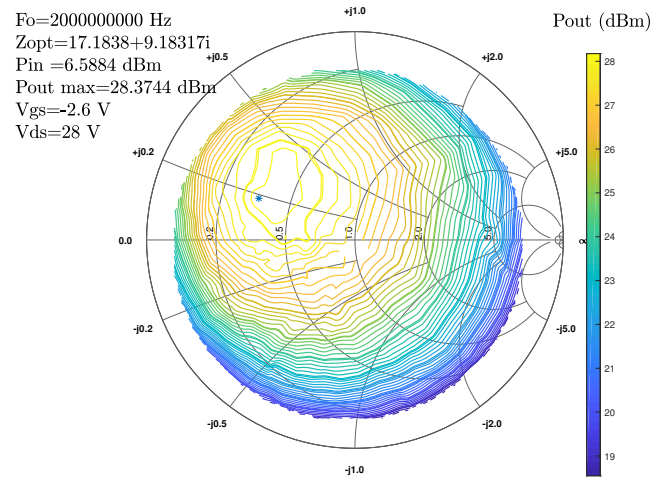


Figure 57. Power contour CGH40010F transistor.

3.5.2 Carrier to intermodulation with two tones

One of the measurements used for characterizing the linearity of the transistor is the carrier to third intermodulation order (C/IM_3 (dBc)), measured according to Gillet *et al.* (2018). In equation (98) P_{tones} is the total power of the fundamental tones, and P_{IM_3} is the power of the third order intermodulation.

$$\frac{C}{IM_3} = 10 \log_{10} \left(\frac{P_{tones}}{P_{IM_3}} \right) \quad (98)$$

Figure 58 shows the C/IM_3 contours using two tones located at 2.0 GHz and $2.0 \text{ GHz} + 15 \text{ kHz}$. The maximum value of C/IM_3 (26.06 dBc) is obtained when an impedance of $18.33 + 21.03i \Omega$ is presented at the frequency of the first tone (2 GHz).

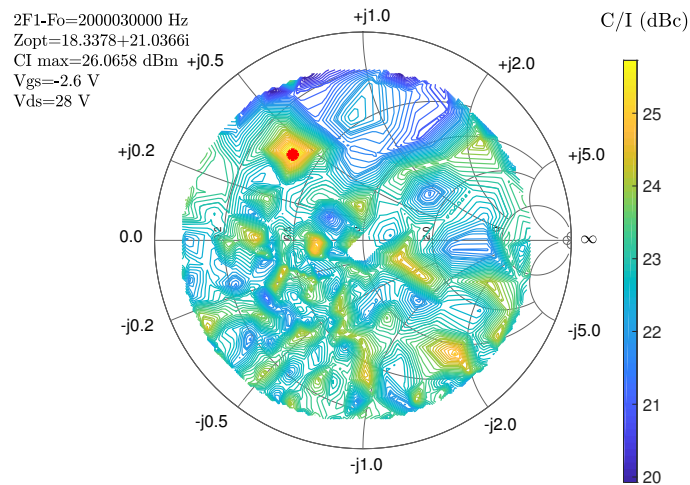


Figure 58. Carrier to Intermodulation (dBm).

3.5.3 Multitone Load-pull results

For LP measurements with multitone, we use ten tones separated 35.875 KHz and centered at 1.999839 GHz. Figures 59 and 60 show the input and output spectrum of the transistor CGH40010F, respectively, when the optimum impedance at 1.999999125 GHz is presented at the output of the transistor.

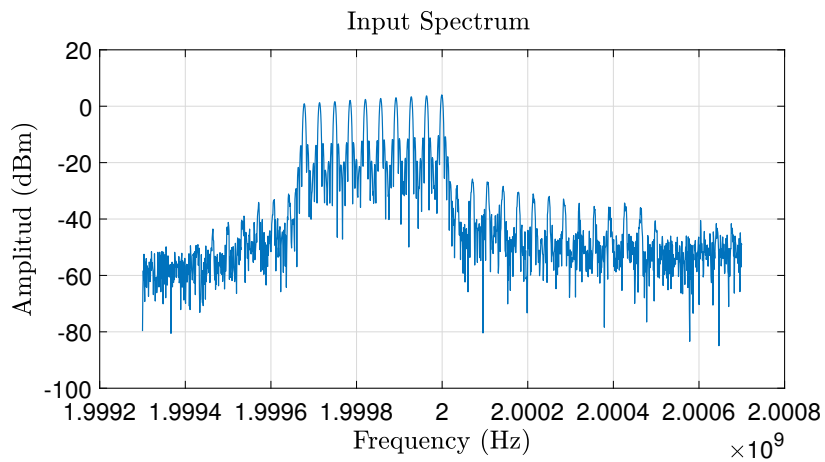


Figure 59. Input spectrum of the DUT.

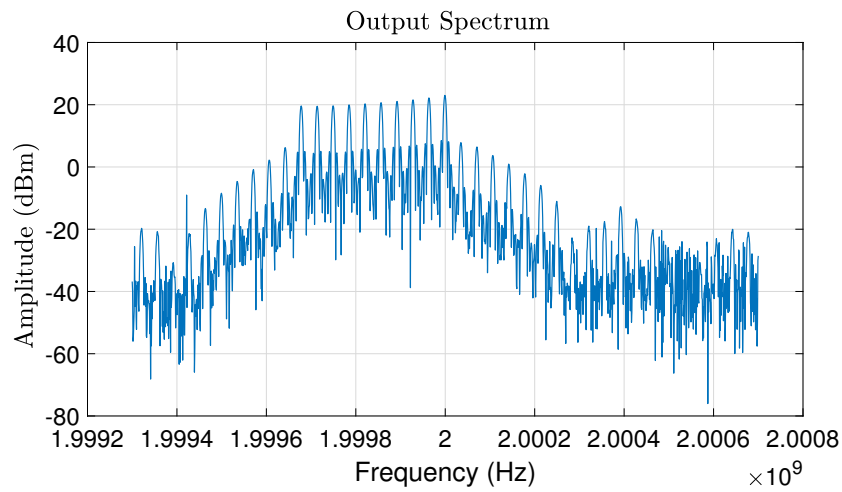


Figure 60. Output spectrum of the DUT.

Figure 61 shows the total output power contours and the optimum loads in each tone when the optimum load at 1.999999125 GHz is applied. The total input and output powers are 15.74 dBm and 30.83 dBm, respectively. A large zoom is done to observe the different optimum impedances at each tone.

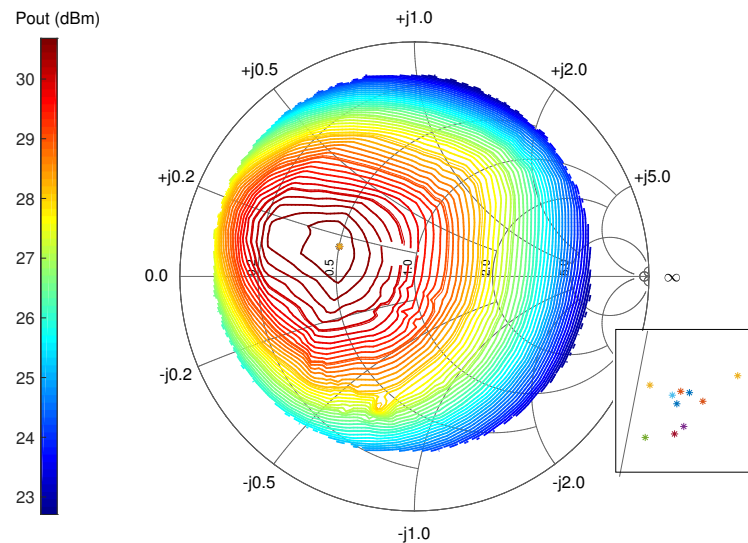


Figure 61. Power contours and optimum impedances with multitone signals.

Table 4 shows the total input and output power when the optimum load is presented to the transistor at the indicated frequency.

Table 4. Input/Output power and optimum impedances.

f (GHz)	Pin (dBm)	Pout (dBm)	Zopt (Ω)
1.999678875	15.74	30.84	25.07+7.26i
1.999713875	15.74	30.84	25.07+7.28i
1.999749750	15.74	30.84	25.02+7.28i
1.999784750	15.74	30.84	25.09+7.22i
1.9998215	15.74	30.84	25.03+7.19i
1.999856500	15.74	30.84	25.06+7.27i
1.999892375	15.74	30.84	25.08+7.21i
1.999928250	15.71	30.84	25.09+7.28i
1.99996325	15.74	30.84	25.11+7.27i
1.999999125	15.74	30.84	25.16+7.32i

This testbed does not require an AWG or to purchase the multitone option for a generator. The calibration presented allows to obtain all measurements in the DUT reference plane, thus giving designers access to the linearity performances of the devices. The PNA-X-5245A does not require extra options like a Spectrum Analyzer (SA), making our measurement system less expensive. Furthermore, GRC is an open source software that runs on Linux OS.

Chapter 4. Calibrated digital predistortion using a VNA as the receiver

This chapter will explain how to turn a VNA into a VSA to acquire and demodulate OFDM waveforms, facilitating the PA behavioral modeling and the DPD linearization of a power amplifier. The dynamic characterization and linearization of the commercial PA ZFL-2500 from Mini-Circuits will be exposed.

4.1 Motivations

The motivation for this approach is to use the same VNA and calibrated tested for both (1) the CW nonlinear response (NVNA) and (2) the modulated vectorial response (VSA) of a device without breaking contact. The feasibility of this approach hinges on the fact that a VNA operated in the receiver mode with a fixed LO can provide the test engineer with both the amplitude and phases for each tone of a periodic modulated signal. In the present Spectrum Analyzer (SA) configuration, the tone amplitudes are calibrated, whereas the acquired tone phases are highly stable but not calibrated. In this chapter, a procedure is developed to perform the phase calibration with a Vector Signal Generator (VSG) to enable an effective VSA operation. To demonstrate the efficacy of this phase calibration, the behavioral modeling and the linearization of the ZFL-2500 PA from Mini-Circuits is demonstrated for a 5 MHz Long Term Evolution (LTE) signal using a VNA and no other receivers. The dynamic AM-AM, AM-PM, and spectral regrowth of an LTE waveform are measured for the PA at 2.3 GHz before and after predistortion. The Normalized Mean Square Error (NMSE), ACPR, Error Vector Magnitude (EVM), and Bit Error Rate (BER) are used as figures of merit to characterize the overall deviation between the expected and measured data.

4.2 Description of the testbed

A schematic and a photograph of the testbed setup used for the PA characterization and linearization are shown in Figure 62. The measurement procedure and testbed are described next. An LTE signal with a periodicity of 1 ms (one subframe) is generated in

Matlab using the *LTE Test Model Tool* with a bandwidth of 5 MHz, a sampling frequency of 7.68 MHz, and a Peak to Average Power Ratio (PAPR) approximately of 10.2 dB. The Dynamic range (DR) of this signal is around 25 dB. To increase the DR, the signal is oversampled to 30.72 MHz and filtered with a Finite duration Impulse Response (FIR) filter with a passband of 2.25 MHz, eliminating 10 % of the guard-band included in the LTE signal to better observe the spectral regrowth. As a result, the signal has a bandwidth of 4.5 MHz and 55 dB of DR.

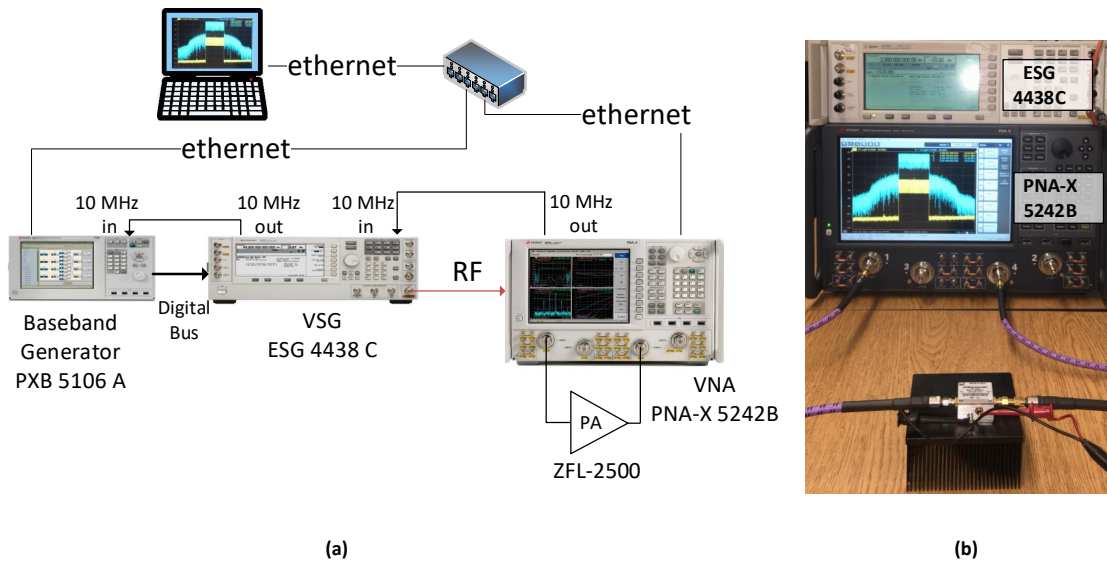


Figure 62. (a) Schematic and (b) picture of the testbed used for the measurements.

The enhanced LTE signal is downloaded to the baseband generator (PXB 5106A) with a resolution of 16 bits and sent via a digital bus to the VSG (E4438C) for up-conversion to the carrier frequency of 2.3 GHz. The RF signal is inserted in the rear panel of VNA (PNA-X) and sent to the input of the PA connected in port 1 of the instrument. The receivers R1 and D are used to measure the input and output of the amplifier, respectively. All the instruments are phase locked to the 10 MHz reference provided by the VNA to ensure phase synchronization. Both the PXB and PNA-X are controlled by a set of Matlab functions, which (1) generate the required digital waveforms in the format required for the instruments, (2) download the test waveforms to the PXB, and (3) upload the waveforms captured by the PNA-X to the Matlab environment for further processing.

The SA measurement class of the VNA is configured to operate with a span of 20 MHz centered at 2.3 GHz and a Resolution Bandwidth (RBW) of 84 Hz (12 ms mea-

surement). In addition, the multitone option signal was configured with a waveform periodicity of 1 ms, the reference tone was set to the center frequency, and a vector averaging of 60 was used to reduce the noise and increase the DR. To remove the error boxes of each receiver, power, and a SOLT calibration were performed at the reference planes of the PA.

4.2.1 Processing the acquired data from the PNA-X

To obtain the dynamic AM-AM, AM-PM and to linearize the PA, some DSP of the received signals is required. A simplified flowchart of the DSP used is shown in Figure 63.

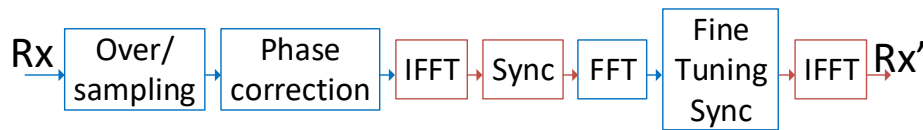


Figure 63. DSP flowchart for the received signals.

The first step adds zeros in the frequency domain to the original signal generated in Matlab (Tx) and the received signal from the PNA-X (Rx) to guarantee that both signals have the same Fast Fourier Transform (FFT) length. Indeed, due to the sampling frequency of 30.72 MHz and its 1 ms period, the Tx signal has 30720 samples, whereas the Rx signal has 20000 samples because of the SA configuration described above.

The Rx' and Tx' baseband signals are next synchronized in the time domain. A phase calibration correction is then carried out in the receivers R1 and D of the PNA-X. An OFDM signal of 20 MHz is introduced in the rear panel of the PNA-X in port 2 to accomplish it. The phase calibration correction is computed in the frequency domain as the difference $\phi_{\text{CAL}}(i)$ for each tone i of radial frequency ω_i between the phases of the received 20 MHz signal (using receiver R2) and the expected VSG 20 MHz signal:

$$\phi_{\text{CAL}}(i) = \phi_{\text{raw}}(i) - \phi_{\text{VSG}}(i) + (\omega_i - \omega_{\text{LO}})\Delta\tau + \Delta\phi_0.$$

The group delay difference $\Delta\tau$ and LO phase offset $\Delta\phi_0$ are obtained when the VSG and VNA signals are synchronized. This phase correction factor can then be subtracted from the received input and output signals of the amplifier.

In order to characterize the repeatability of this phase calibration, 11 measurements were performed with an OFDM signal of 20 MHz. Figure 64 shows the phase calibration correction computed for the 11 different measurements of the OFDM signal. The average standard deviation over the 20000 tones was 0.42 degrees with a maximum standard deviation of 3.7 degrees.

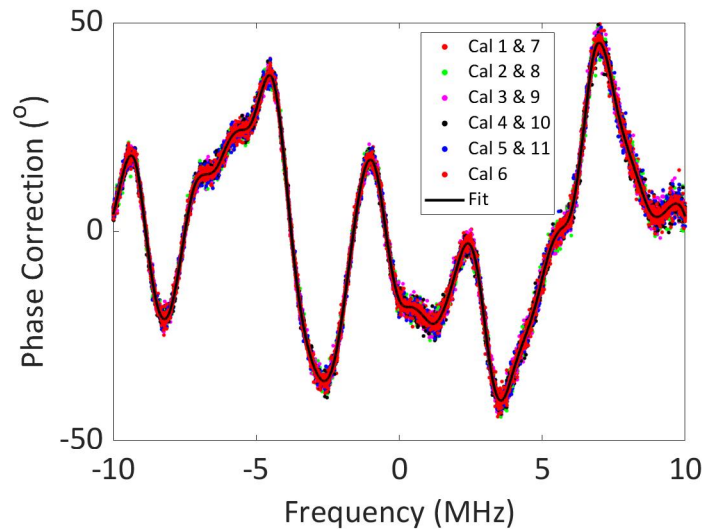


Figure 64. Phase calibration ϕ_{CAL} corrections obtained for 11 different measurements.

4.3 Measurements with LTE signal and linearization

The amplifier ZFL-2500 has a linear Gain of 28 dB and an output power of 16 dBm at the 1 dB compression point. An LTE signal of 5 MHz with a PAPR of 10.2 dB and average input power of -20.5 dBm was used to characterize its dynamic response. A DPD linearization is then applied to linearize the PA.

4.3.1 Linearization results

The ZFL-2500 amplifier was linearized by predistorting the input signal $x(n)$ using the technique of indirect learning. Here n is the discrete time index. The input data $x(n)$ were modeled in terms of the output data $y(n)$ using generalized memory Gain functions G_m with a memory depth M of 3:

$$x(n) = \sum_{m=0}^{M-1} G_m(|y(n-m)|^2)y(n-m). \quad (99)$$

The memory Gain functions $G_m(|y|^2)$ are implemented using a cubic-spline basis with 25 segments as in Narahariseti *et al.* (2015). A total of 78 coefficients were used. The nonlinearities and memory effect of this device are shown in the AM-AM and AM-PM curves in Figure 65, as well as DPD results.

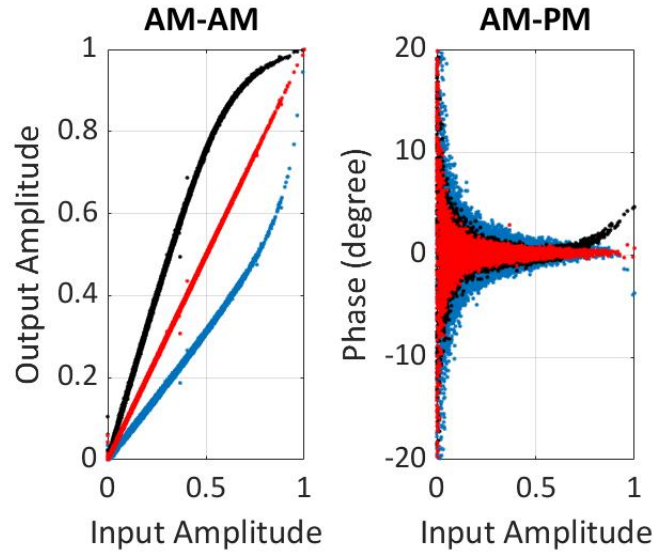


Figure 65. Dynamic AM-AM and AM-PM curves of ZFL-2500 amplifier without DPD (black), its inverse (blue), with DPD (red).

The spectra of the output signal of the amplifier before and after the predistortion are shown in Figure 66.

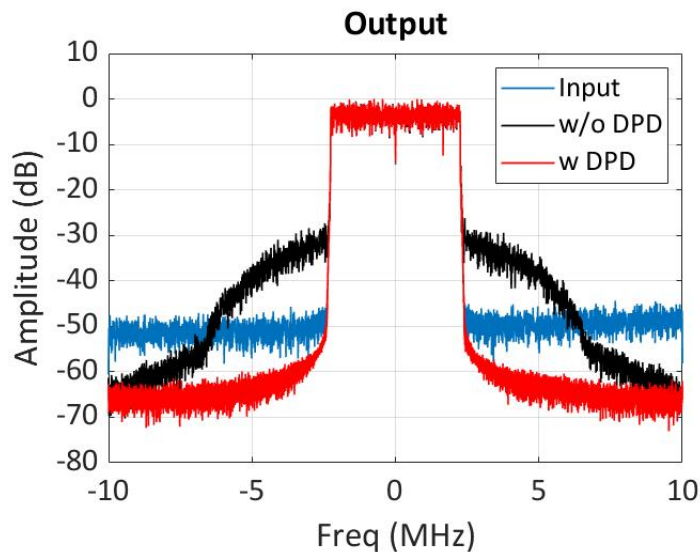


Figure 66. Spectra of ZFL-2500 amplifier before and after DPD.

4.3.2 Figures of merit

The AM-AM and AM-PM characteristic plots presented in Figure 65 cannot be generated if the phase calibration is not performed. The time synchronization shown in Figure 63 must also be repeated after the phase calibration is applied, as the envelope is strongly dependent on the tone phases. Note that the synchronization performed is based on the peak amplitude of the cross-correlation as shown in equation (100) without any windowing, since the modulation is periodic.

$$[x \star y](m) = \mathbf{x}(n)^T \cdot \mathbf{y}(n - m) \quad (100)$$

The 64 QAM constellations obtained from the 20 MHz OFDM signal before (red dots) and after (blue dots) the calibration correction and the synchronization are applied to the raw data, are shown in Figure 67 (a). The constellations obtained from 5 MHz OFDM signal with no circular prefix at the PA input and the PA output before and after DPD are shown in the constellation diagram in Figure 67 (b), (c) and (d) respectively. The resulting calibrated OFDM complex RF envelope acquired using the VNA allows one to quantify the nonlinearities of the PA in (1) the time domain with the NMSE, (2) the IQ domain with the EVM and (3) the digital domain with the BER. These figures of merit for the 5 MHz QAM-64 constellation of Figure 67 are given Table 5.

4.3.3 Testbed proposed to measure multiple input power amplifiers

Nowadays, VNAs and Nonlinear Vector Network Analyzer (NVNA) to directly evaluate the nonlinearity of PAs are becoming more popular. Examples of these testbeds are reported in Teyssier *et al.* (2014) and Gillet *et al.* (2018), where the nonlinear characterization of the DUT is done using an USMT signal. The receivers used are sampler-based and mixer-based NVNAs, respectively. The USMT allows to measure the actual power of each intermodulation product, owing to the tone spacing selected such that the third order intermodulation products do not overlap with one another or the input signal frequencies.

Dual-input PAs receive special attention from the PA designers to investigate the enhanced average efficiency and the wide bandwidth they can achieve. In El-Deeb

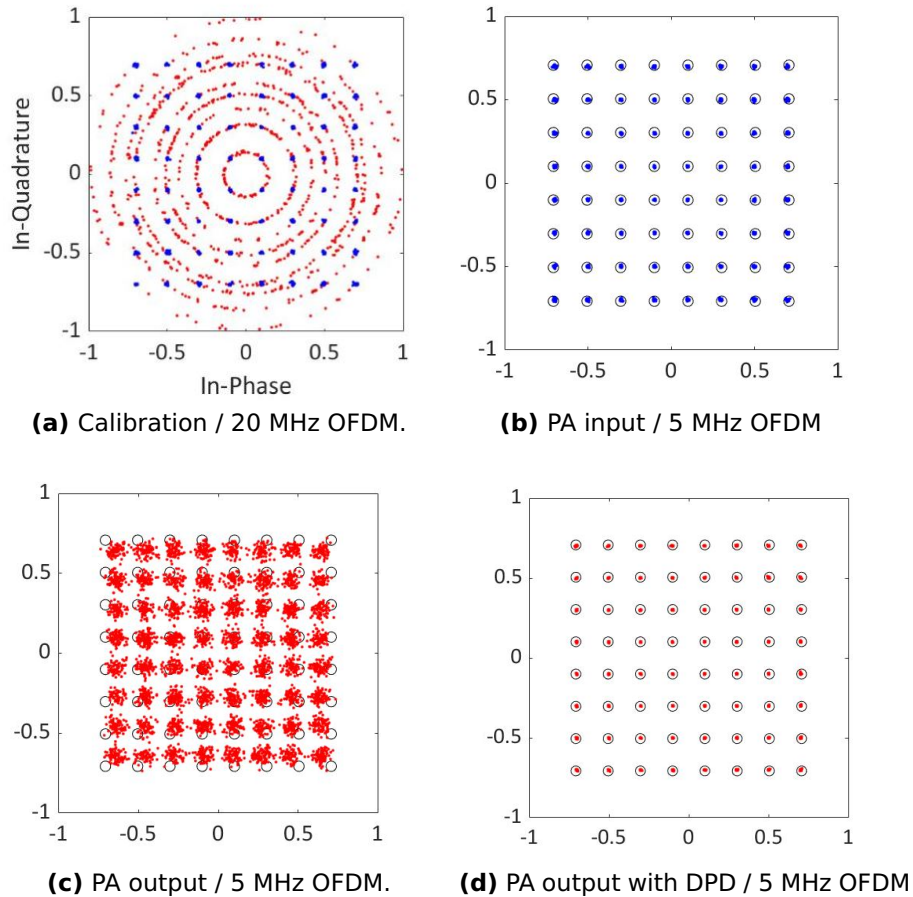


Figure 67. Constellations (a) for a thru: raw (red dots) and calibrated (blue dots) with 20 MHz OFDM, and for the PA input (b) (blue dots) and output with DPD (c) and without DPD (d) for 5 MHz OFDM (red dots).

et al. (2011) the design and characterization of a multiple input RF PA are presented, where the incident and reflected signals of the DUT are captured with channel one of a multiharmonic MTA HP70820A, while channel two is used as the phase reference by receiving a sample of the RF source. In Nguyen and Barton (2017) a linearity characterization of a Chireix PA is performed for one and two tones using a VSA. The low and high IMD of the third order are inspected under different gate bias conditions. In Reveyrand *et al.* (2019) an automatic calibration method for multi-port large-signal measurements is presented, where the validation of the testbed is done using a dual-input PA and Load Modulated Balanced Amplifier (LMBA).

In Liang *et al.* (2019b) and Liang *et al.* (2019a), the design and characterization of a dual-input Hybrid Doherty Outphasing PA (HD-OPA), which provides a high efficiency between peak and backoff together with a high peak-to-backoff fundamental drain

Table 5. Figures of Merit for the OFDM Measurements.

Measurement Conditions	PAPR (dB)	$ACLR_{L,H}$ (dBc)	NMSE (dB)	EVM (%)	BER (%)
PA Input	10.47	-48.65,-47.15	-38.78	1.49	0
Output w/o DPD	5.42	-28.92,-29.09	-1.96	12.41	26.8
Output w DPD	10.53	-61.70,-59.99	-43.37	0.988	0

voltage ratio, is investigated. The CW measurements of HD-OPA were performed using a LSNA, and the dynamic response was verified with a different testbed using a Field Programmable Gate Array (FPGA). The same DUT will be used in this work with the same new proposed characterization testbed.

In this section, a VNA testbed completely automatized and fully calibrated in magnitude and phase is introduced and demonstrated for characterizing dual-input out-phasing PAs with both CW and modulated signal without breaking electrical contact with the DUT. This measurement setup represents an extension of the work reported in Niubo-Aleman *et al.* (2019) where a testbed using a VNA as a receiver was used to characterize and linearize a *single input* commercial PA using modulated signal (LTE/OFDM). In that original work, the signal bandwidth for the modulated measurement was limited by the 30 MHz bandwidth of the VNA receiver thus limiting the demonstration to signals with 5 MHz OFDM signals. In this new work, the phase calibration theory and phase stabilization technique has been upgraded, and the signal bandwidth for the modulated measurement is no longer limited by the 30 MHz bandwidth of the VNA receiver. The phase calibration is now demonstrated with 120 MHz acquisition bandwidth to characterize the HD-OPA considered. Finally, compared to Niubo-Aleman *et al.* (2019) the new testbed is now able to fully characterize and linearize dual-input Out-phasing Power Amplifier (OPA) which are very sensitive to the input differential phase calibration.

To demonstrate the usefulness of this testbed, the static and dynamic AM-AM and AM-PM curves of the HD-OPA working at 2.08 GHz are obtained before and after linearization for 10 MHz and 20 MHz OFDM signals. The NMSE, the Adjacent Channel Leakage Ratio (ACLR), and the constellation EVM are used as figures of merit to verify the performance of the linearization algorithm using this new testbed.

4.4 Description of the testbed

Figure 68 shows the testbed used in this work to characterize OPAs. The dual-input modulated baseband signals are synthesized in Matlab and then downloaded to an AWG (M8190A) which generates the RF signals using Digital-Upconverter (DUC). This guarantees that the two modulated RF channel outputs are synchronized and phase-coherent. Thus, the IQ modulation is done digitally, removing all the distortions arising when using an external analog IQ modulator. To reach the expected input power levels, the RF modulated signals are fed into two drivers. Two isolators are placed at the output of the drivers to prevent damages caused by any accidental significant power reflection coming from the DUT. The PNA-X provides the 10 MHz reference to the AWG. The incident waveforms of the main and peaking PAs are measured at the R1 (a1) and R2 (a2) VNA receivers, and the reflected waveforms at the A (b1) and B (b2) VNA receivers. The output signal is measured at the C (b3) receiver. The measurements are acquired using the SA option of the VNA and its capability to compute the phase of each tone. This feature combines with the High DR of the receivers, and the wide span of the instrument (10 MHz - 50GHz) turns a PNA-X into a powerful VSA with five receivers. Two low loss external bidirectional couplers (LLC18-7, Maury Microwave) are used to take samples of the waveforms at the OPA inputs while the directional coupler (CA18, Marki) is placed at the output to handle the high power levels. External attenuators are also placed at the receiver inputs to prevent their saturation and guarantee the correct extraction of the OPA nonlinear behavior. All the instruments are controlled via ethernet using Matlab running on a remote PC.

The testbed of Figure 68 is proposed to characterize the HD-OPA firstly under continuous waves regimen, based on a Look-Up-Table (LUT) which is obtained during the simulations in the ADS. For the correct performance of the phase detection, a onetime calibration of the LO in IF is done, while the IF Gain calibration is carried on to correct the IF filter responses, which will be explained in subsequent sections. A power and vector calibrations using the well known SOLT method are also required to shift the reference planes to the inputs and output of the DUT.

The two channels of the AWG M8192A with the Digital-Upconverter (DUC) option are used to generate the RF input signals. With this option, the IQ modulation is done internally by software, removing all the distortions caused by an external analog IQ

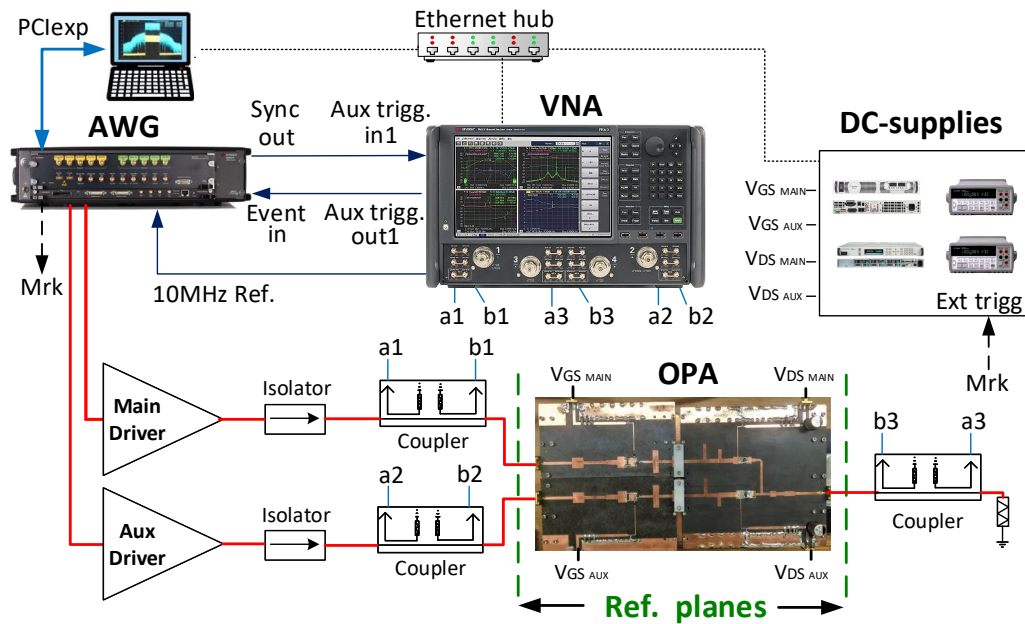


Figure 68. Proposed Vector Signal Network Analyzer (VSNA) testbed for the characterization and linearization of dual-input outphasing PAs.

modulator. The DUC includes the interpolation of IQ sample pair from a low input data rate to the sampling rate of the instrument, making efficient utilization of the sample memory. The carrier frequency is generated by a Numerically Controlled Oscillator (NCO). The control data is in time aligned with the sample data, allowing changing settings like the phase, amplitude, and frequency of the carrier at run-time. Each channel of the AWG has its NCO, suitable to sweep the power and phase independently in each one.

To get the behavior of the HD-OPA, a sequence table made up of different segments is implemented in each channel, in such a way that each entry or segment of the table causes a change of 10-degree difference between the inputs, sweeping from 20 to 130 degree for each input powers of interest. The original waveform is generated in Matlab with a source sample frequency of 600 MHz. The AWG is configured with a sampling frequency of 7.2 GHz, an interpolation factor x3 which gives a Digital to Analog Converter (DAC) sample rate of 2.4 GHz (this is the speed at which samples in the output waveform are converted). A timing resampling mode is selected to increase the source sample to the DAC sample rate (2.4 GHz). Finally, the output waveform and the LO are sampling with the same sample frequency selected. The 10 MHz clock signal of the PNA-X is shared with the AWG. The RF signals are fed into two drivers to provide the required level of input powers.

The DC supply system consists of an N7600B with three DC power supply modules, used to generate the gate voltages of each PAs and the drain voltage for the main PA. The power supply N5751A is used to set the drain voltage for the auxiliary PA. Two Digital Multimeter (DMM) 34410A of high precision are placed to measure the drain currents of the Main and Peaking PAs separately.

The Figure 69 shows the connection that guarantees a synchronous measurement system. The AWG is set to trigger mode, and each entry on the table of the AWG

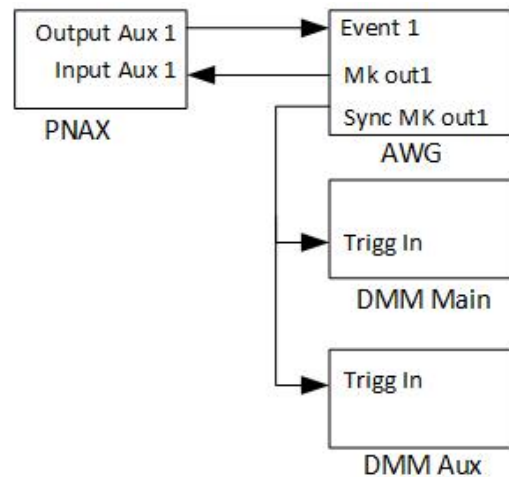


Figure 69. Synchronization system connection.

sequence mode is put to single advance mode, which means that a positive pulse is mandatory to jump to the next segment in the table; the PNA-X will generate it through the Output Aux1 rear BNC connector connected to the Event In in the AWG before acquiring measurements. In addition, the handshake in the PNA-X is selected; a sweep will be done when a pulse is received at the Input Aux1 BNC connector. Each jump in the table will generate a pulse at the start of the sequence at the Mk out1 and Sync Mk out1 connectors, which are used to trigger the PNA-X and the DMMs previously configured to accept several external triggers equal to the total segments in the AWG sequence.

4.4.1 Standard VNA calibration

A 3-port VNA calibration is first performed to characterize dual-input OPAs at the three reference planes (green dashed lines) shown in Figure 68. The 3-port calibration is done using the PNA-X internal software, at the PA center frequency of 2.08 GHz, for

a 120 MHz frequency span with 5 kHz tone spacing. A three-port relative calibration is performed to remove the error boxes present in the PNA-X receivers, using the SOLT method as reported in Ferrero and Pisani (1992). Also, a power calibration at the reference planes is done to correct the losses in the RF path. The SA option of the PNA-X uses this calibration. This option internally calculates the phases at each tone of the measured periodic signals in the fundamental band. Note that no phase reference nor hardware trigger is required during the measurements, as is the case for the NVNA.

4.4.2 Calibration of the VSNA

In this work, the IF phase-calibrated receivers of the VNA are used to realize a 5-channel VSA effectively. This testbed is referred to short in this thesis as the VSNA. The VSNA requires a modulated RF source for the preliminary phase calibration of its five channels. A calibrated two-channel AWG is used as a transfer standard for the VSNA phase calibration in this work.

To test the calibrated AWG used as a phase reference, an OFDM signal with 24,000 tones modulated with a 4-QAM scheme, a bandwidth of 120 MHz, and a period of 200 μ s was used. The AWG signal was acquired with a VSA (UXA N9040B). After time alignment of the measured VSA data, a phase standard deviation and a maximum phase of 0.023° and 0.06° over the 120 MHz measurement span were obtained for both AWG channels with a maximum amplitude deviation of 0.009 dBm.

The reference AWG was used to calibrate the five VSNA receivers ($r = 1 \dots 5$) involved in the PNA-X measurement system. The same 4-QAM OFDM signal with 24,000 tones and 120 MHz generated by the AWG is used.

The phase calibration correction is calculated in the frequency domain for each channel r , as the phase difference $\phi_r^{\text{CAL}}(i)$ for each tone i of radial frequency ω_i between the received VSNA signal and the input AWG OFDM signal after the time alignment, delay $\Delta\tau_r$ and LO phase $\Delta\phi_{\text{LO},r}$ are extracted:

$$\phi_r^{\text{CAL}}(i) = \phi_r^{\text{raw}}(i) - \phi_{\text{AWG}}(i) + (\omega_i - \omega_{\text{LO}})\Delta\tau_r + \Delta\phi_{\text{LO},r}. \quad (101)$$

Note that internally, the VNA uses five different LO center frequencies across the 120 MHz signal bandwidth used here due to its receiver's 30 MHz bandwidth limitation. In

the latest version of the SA option of the PNA-X, this process is transparent to the user. Otherwise, the LO phase can be quickly recovered during time align for every 30 MHz subbands. In Niubo-Aleman *et al.* (2019) the measurements were limited to 30 MHz. In this work, a bandwidth of 120 MHz matching the spec of the dual-input HD-OPA DUT is used to demonstrate that the signal bandwidth is not limited by the receiver bandwidth. It is essential to highlight that the testbed is appropriate to measure 5G signals. GHz bandwidth has been reported using such a PNA-X to calculate the input-output EVM in Verspecht *et al.* (2019).

The $\phi_r^{\text{CAL}}(i)$ are nearly the same for all the five receivers of the VNA used. Thus the phase calibration correction can be expended as:

$$\phi_r^{\text{CAL}}(i) = \phi_{\text{avg}}^{\text{CAL}}(i) + \delta\phi_r^{\text{CAL}}(i) \quad (102)$$

where $\phi_{\text{avg}}^{\text{CAL}}(i)$ is the average phase correction over the five receivers of the VNA and $\delta\phi_r^{\text{CAL}}(i)$ is the residual phase correction for each channel r . The average values $\phi_{\text{avg}}^{\text{CAL}}$ are now removed by the SA option during the measurement, and only the residual phase and amplitude corrections need to be performed to obtain accurate measurements in the time domain. The average phase correction $\phi_{\text{avg}}^{\text{CAL}}(i)$ over the 30 MHz bandwidth of the VNA receiver was reported in Niubo-Aleman *et al.* (2019). We focus here instead over the residual phase correction $\delta\phi_r^{\text{CAL}}(i)$ obtained for the three receivers R1 (a1), R2 (a2), and C (b3) for $r = 1, 2$ and 3 respectively over now 120 MHz bandwidth.

Figure 70, shows in the frequency domain, (a) the normalized amplitude difference in dB between the original and measured signal and (b) the phase calibration factor $\delta\phi_r^{\text{CAL}}$ when the LO phase offset and group delay are extracted by synchronizing the AWG and VSNA received signals. The maximum values of the phase correction ϕ_r^{CAL} required by three receivers considered are 2.12° , 1.64° , 1.35° , while the maximum amplitudes of the Gain correction are: -0.34 dB, -0.29 dB, -0.26 dB, respectively. In order to characterize the repeatability of the IF phase calibration, ten measurements were performed. The standard deviations of the phase correction ϕ_r^{CAL} averaged over the 24,000 tones are found to be 0.025° , 0.046° , 0.060° for the three VSNA receivers, respectively.

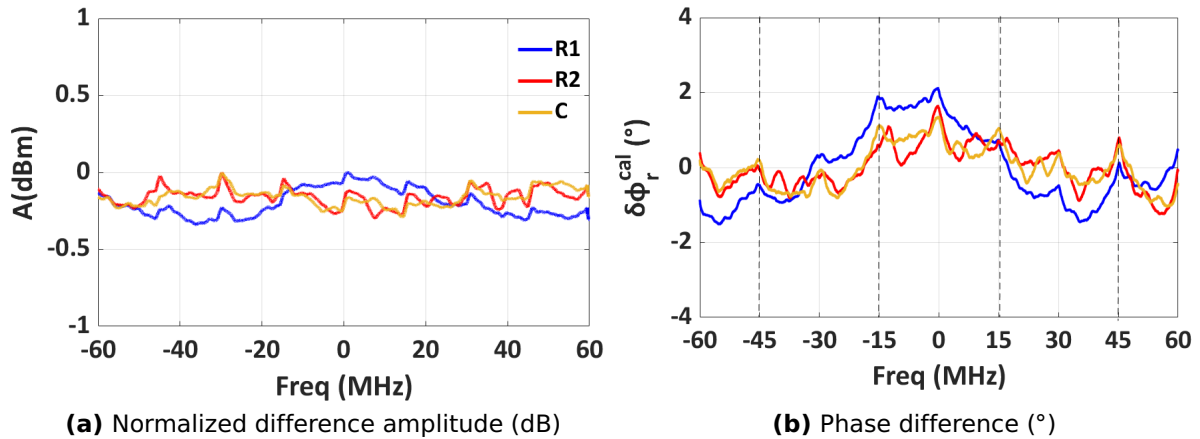


Figure 70. Amplitude and phase calibration factors of VSNA (PNA-X) receivers R1,R2 and C.

From Figure 70 (b), the pattern of the residual phase stitching over the five 30 MHz subbands is observed in the 120 MHz selected frequency span for each of the three channels.

Once the calibration factor $\phi_r^{\text{CAL}}(i)$ has been simultaneously acquired for all channels r , the VSNA is ready for characterizing a multi-channel nonlinear DUT. Applying the phase correction $\phi_r^{\text{CAL}}(i)$ to the raw data acquired by the VSNA, yields the corrected channel phase ϕ_r^{VSNA} for each tone i of radial frequency ω_i :

$$\phi_r^{\text{VSNA}}(i) = \phi_r^{\text{raw}}(i) - \phi_r^{\text{CAL}}(i) + (\omega_i - \omega_{\text{LO}})\Delta\tau'_r + \Delta\phi'_{\text{LO},r}. \quad (103)$$

It is important to note that new group delay $\Delta\tau'_r$ and LO phase offset $\Delta\phi'_{\text{LO},r}$ need to be extracted for each new measurement when synchronizing the AWG and VNA signals. This time synchronization process is only needed to remove the phase rotation in the constellation, which would lead otherwise to incorrect high constellation EVM values. However, the same phase correction factors $\phi_r^{\text{CAL}}(i)$, determined during IF calibration, apply to all subsequent measurements at the frequencies ω_i in channel r .

Zero paddings oversample the signal acquired by the PNA-X in the frequency domain. The sampling frequency used for the AWG is 600 MHz, and the effective sampling frequency of the data collected by the VSNA is 120 MHz when using a 120 MHz span. A flowchart summarizing the post-processing calibration performed by the VSNA on the raw data is given in Figure 71.

To verify the VSNA calibration, a different 20 000 tone OFDM signal with 16-QAM

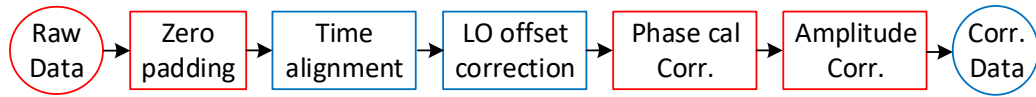


Figure 71. Flowchart of the VSNA post-processing applied to the raw data of each channel to obtain the corrected multi-channel measurement data.

instead of 4-QAM and 100 MHz bandwidth and centered at 2.08 GHz, was measured with the VSNA using the same frequency span of 120 MHz. Table 6, shows the EVMs (% , dB) obtained for the received signal before and after applying the post-processing steps, depicted in Figure 71, to the measured signal. The associated IQ constellations are drawn in Figure 72.

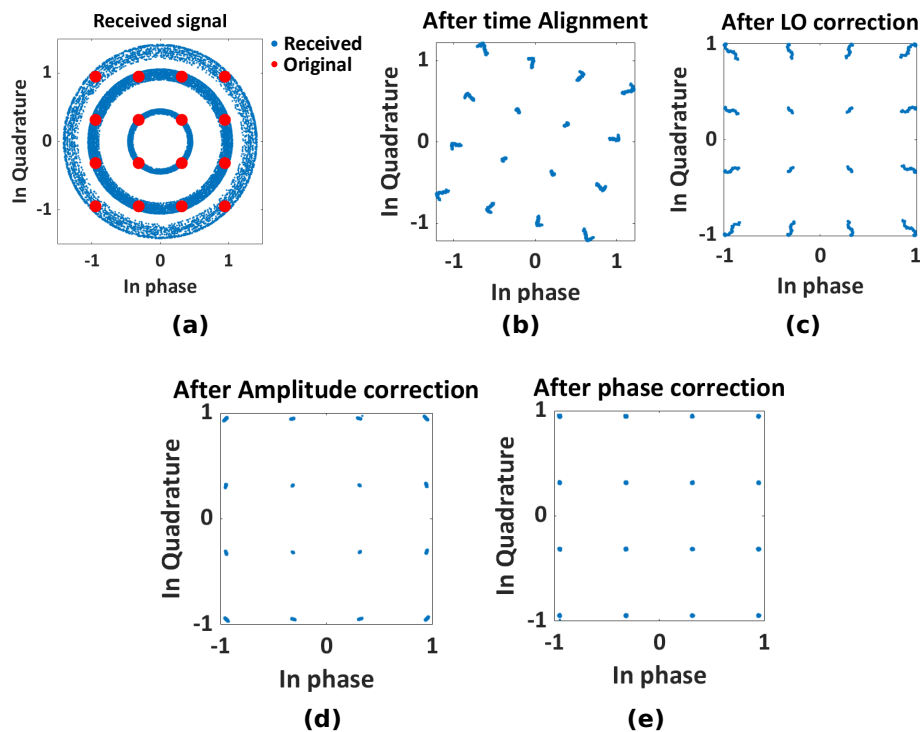


Figure 72. Verification of the VSNA calibration for a 100-MHz 16-QAM signal using the IQ constellations: (a) received and obtained after successively applying the VSNA (b) time alignment, (c) LO phase offset, (d) amplitude and (e) residual phase corrections.

From Table 6 it is noticed that the time alignment is among the slightest correction. However, it is mandatory to apply it in the first step; without it, the subsequent corrections would not be effective. In Figure 72(a), the original IQ-constellation is depicted in red dots, while the received IQ-constellation by the VSNA receiver is represented with blue dots. An EVM of 0.55 % (-45.19 dB) and NMSE of -44.94 dB were obtained after applying the residual amplitude and phase corrections.

Table 6. EVM values in % and dB obtained for an OFDM signal of 100 MHz with 16 QAM at each step of the calibration

	EVM (%)	dB	Correction (dB)
Received Signal	122	1.72	
Time alignment	53.88	-5.37	7.09
$\Delta\phi_{LO,r}$	4.70	-26.56	21.18
Amplitude corr.	1.06	-39.49	12.93
Phase corr.	0.55	-45.19	5.69

It should be noted that the IF calibration error has been reduced in this work as the phase shift contributed by the IF filter of the PNA-X receiver (characterized in Niubo-Aleman *et al.* (2019)) has now been integrated as part of the equipment calibration.

4.4.3 Extending the measurement frequency span of the VSNA until 500 MHz.

For the linearization of nonlinear PAs, it is required to measure the output spectral regrowth. A good practice is to acquire the signals using a measurement frequency span at least five times the bandwidth of the signal. For 5G broadband PAs using a 100 MHz signal, a measurement frequency span of 500 MHz is required.

To use the VSNA receivers for the dynamic characterization and linearization of these PAs, it is necessary to calibrate the receivers in the whole frequency span. To accomplish this, a 500 MHz, 64 QAM OFDM signal, with a 1 GHz sampling frequency and tone spacing of 5 kHz (100 000 tones), PAPR 10.78 dB and an average power of 18.87 dB is used.

Figure 73(a) and 73(b) show the amplitude and phase corrections extracted for each receiver in a frequency span of 500 MHz.

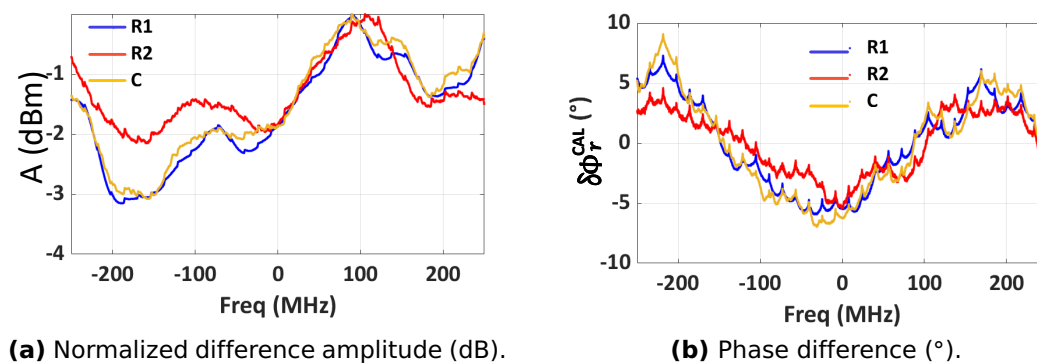


Figure 73. Amplitude and phase corrections using a 500 MHz signal.

Figure 74 depicts the original (red circles) and received (blue pluses) IQ constellations after applying to the measured signal at each of the post-processing steps shown in Figure 71. An EVM of 0.48 % and an NMSE of -46.50 dB were obtained. To calculate the measurement standard deviation, ten measurements were performed, yielding a Signal to Noise Ratio (SNR) of 46.49 dB.

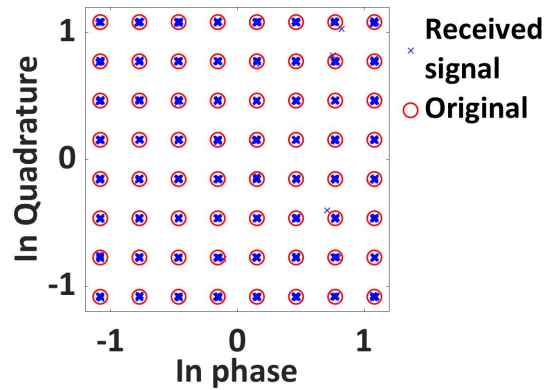


Figure 74. IQ-constellation of the received signal after corrections for a 64 QAM 500 MHz signal.

Figure 75 gives a visual presentation of the relative phase error contributions. It shows the original 52 subcarrier phases for a 64-QAM OFDM signal with a bandwidth of 500 MHz, tone spacing of 5 kHz, and 100 000 subcarriers. The red circles are the

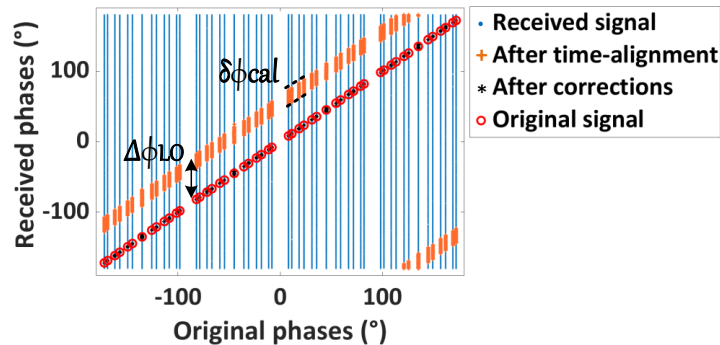


Figure 75. Phases of the subcarriers in the frequency domain vs the original ones.

original phases while the blue dots are the received ones, the orange thick pluses represent the phases after time alignment, and the black stars the final phases after the residual calibration. From Figure 75, it is noticed that after performing the time alignment, the subcarrier phases are offset from the original ones by a constant value. This offset is introduced by the phase difference ($\Delta\phi_{LO}$) between the phased-locked local oscillators of the VSNA and the AWG.

Table 7 shows the EVM (in dB) obtained at each step of the post-processing calibra-

tion of Figure 71 for the 500 MHz OFDM signal.

Table 7. EVM values in % and dB obtained for an OFDM signal of 500 MHz with 64 QAM at each step of the calibration

	EVM (%)	dB	Correction (dB)
Received Signal	114	1.14	
Time alignment	87.81	-1.13	2.27
$\Delta\phi_{LO,r}$	12	-18.41	17.28
Amplitude corr.	6.54	-23.69	5.28
Phase corr.	0.47	-46.56	22.87

4.4.4 Measurements performed with the PNA-X-VSNA and VSA

Figure 76 shows the testbed simplified, used to measure different OFDM signals with the PNA-X-VSNA and VSA. It is noticed that the actual power arriving in the PNA-X receivers will be around 40 dB lower than the power sensed by the VSA due to the coupling factor and the attenuator used to protect the PNA-X receivers and assure working in the linear region.

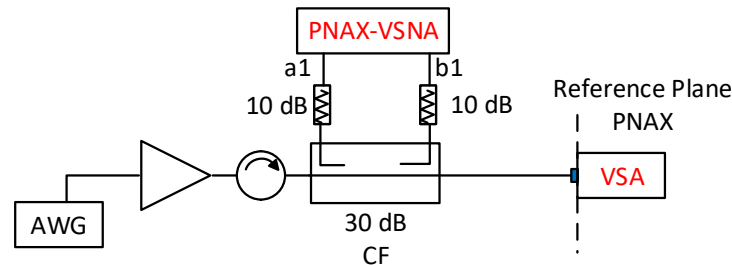


Figure 76. Testbed to measure different OFDM signal with PNA-X and VSA.

For the extraction of the phase and amplitude calibrations required to correct the signals measured with both instruments, a 4-QAM OFDM signal with 120 MHz, 5 kHz of spacing tone (24 000 tones), PAPR 10.25 dB, average power 3.40 dBm was measured ten times with each instrument, which is named calibration signal.

The average value of the phase and amplitude corrections extracted for both instruments are saved and used to correct signals with different bandwidths.

Figures 77 (a) and (b) show the flowcharts to obtain the phase and amplitude corrections of both instruments (PNA-X-VSNA, and VSA) and the process to measure and correct an OFDM signal different from the one used for the instrument characterization, respectively.

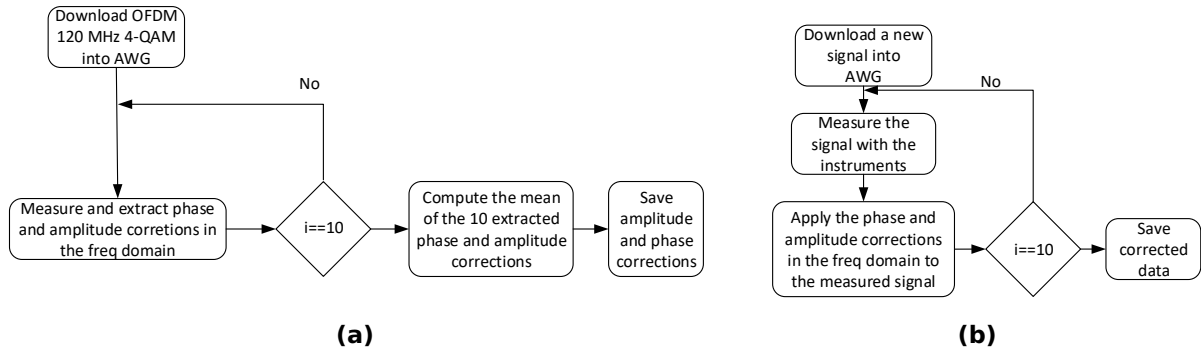


Figure 77. Flowcharts, (a) To extract the phase and amplitude calibrations, and (b) to measure and correct a new signal.

For the statistical analysis of the phase and amplitude corrections extracted with the PNA-X-VSNA and VSA, the variance (σ^2), standard deviation (σ), mean value (μ) and expected value ($E[\]$) of a random variable $Z(i, freq)$ with i observations, taken at the frequency $freq$, are computed as indicated in equations (104-??):

$$\sigma^2(Z(i, freq)) = E[|(Z(i, freq) - E(Z(i, freq)))|^2] \quad (104)$$

$$\sigma(Z(i, freq)) = \sqrt{\sigma^2(Z(i, freq))} \quad (105)$$

$$\mu = \frac{1}{N} \sum_{i=1}^N Z(i, freq) \simeq E(Z(i, freq)) \quad (106)$$

The maximum values of the standard deviation for the complex correction extracted ten times with the VSA and PNA-X-VSNA are 0.13 and 0.024, respectively.

The dispersion can be reduced either by increasing the power level of the signal or the number of acquisitions per frequency (the average at each frequency will reduce the noise).

The maximum values of the standard deviation of the complex correction for ten measurements obtained with the PNA-X-VSNA, using the same OFDM signal as before but increasing the average power level from 3.40 dBm to 8.60 dBm is 0.0041.

The equation of the SNR for a measured signal is shown below:

The instantaneous voltage measured $y(t)$ is shown in equation 107, where $x(t)$ is the

original signal and $n(t)$ the noise.

$$y(t) = x(t) + n(t) \quad (107)$$

The instantaneous power is given in 108;

$$|y(t)|^2 = x(t)^2 + n(t)^2 + 2x(t)n(t) \quad (108)$$

Therefore, with the assumption that $x(t)$ and $n(t)$ are uncorrelated, the average power is given in 109, where E is the expected value.

$$\overline{|y(t)|^2} = E(y(t)^2) = \overline{x(t)^2} + \overline{n(t)^2}, \quad (109)$$

Then the SNR in dB is calculated as:

$$SNR = 10 \log_{10} \left(\frac{\overline{x(t)^2}}{\overline{n(t)^2}} \right) = 10 \log_{10} \left(\frac{\overline{|y(t)|^2}}{\overline{n(t)^2}} \right) \quad (110)$$

The analysis for complex signals are depicted below:

$$y = (x_r + n_r) + j(x_i + n_i) \quad (111)$$

The complex power of the received signal

$$y^2 = (x_r + n_r)^2 - (x_i + n_i)^2 + 2j[(x_r + n_r) \times (x_i + n_i)] \quad (112)$$

The absolute power of the received signal

$$|y^2| = (x_r + n_r)^2 + (x_i + n_i)^2 \quad (113)$$

The average power of the received signal :

$$\overline{|y(t)|^2} = E[(x_r + n_r)^2 + (x_i + n_i)^2] = (\overline{x_r^2} + \overline{x_i^2}) + (\overline{n_r^2} + \overline{n_i^2}) \quad (114)$$

From equation 114 it is noticed that, the average power level of the signal is the sum of the average square of the real and imaginary components of the noise and the original signal, when they are uncorrelated ($E(x \times n) = 0$).

The average power of the noise is :

$$\overline{|n(t)|^2} = E[(y'_r - x'_r)^2 + (y'_i - x'_i)^2] = (\overline{x'^2_r} + \overline{x'^2_i}) + (\overline{y'^2_r} + \overline{y'^2_i}) - 2(\overline{y'_r x'_r} + \overline{y'_i x'_i}) \quad (115)$$

Where $y'_{r,i}$ and $x'_{r,i}$ are the real and imaginary components of the received and original signal normalized to their respective mean square values.

From equation 115 it is observed that $\overline{|n(t)|^2} = 0$ if $y = x$.

The SNR (dB) expressed in terms of the real and imaginary components of the original and received signal is given in equation 116

$$SNR(dB) = 10 \log_{10} \left(\frac{E(|x'|^2)}{E(|y' - x'|^2)} \right) = 10 \log_{10} \left(\frac{\overline{x'^2_r} + \overline{x'^2_i}}{(\overline{x'^2_r} + \overline{x'^2_i}) + (\overline{y'^2_r} + \overline{y'^2_i}) - 2(\overline{y'_r x'_r} + \overline{y'_i x'_i})} \right) \quad (116)$$

The equation 116, is used to compute the SNR (dB) for the signals measured with the VSA and PNA-X-VSNA.

The SNRs (dB) values obtained with the commercial VSA, and the PNA-X-VSNA for the OFDM calibration signal, with an average power of 3.40 dBm, are 29.80 dB, 44.26 dB, respectively. The Root Mean Square (RMS) EVM in percentage of a received signal is computed as the square root of the average square of the error between the measured and the reference symbols when they are normalized to their respective average symbol power, as equation (117) shows.

$$EVM_{RMS} = 100 \sqrt{\frac{(\overline{I^2} - \overline{I_r^2}) + (\overline{Q^2} - \overline{Q_r^2})}{(\overline{I_r^2} + \overline{Q_r^2})}} \quad (117)$$

$$EVM_{dB} = 20 \log_{10}(EVM_{RMS}) \quad (118)$$

where I and I_r are the In phase components of the measured and reference symbols normalized to the mean square amplitude of the symbol, while Q and Q_r , are the quadrature components. The average EVMs obtained with the VSA and PNA-X-VSNA are 3.08% (29.80 dB), 0.61% (44.26 dB).

Different OFDM signals were downloaded to the AWG and measured ten times, with

the scheme shown in figure 76. Then, for the amplitude and phase corrections of the received signals with the PNA-X-VSNA and VSA, the corrections extracted with the calibration signal (Figures 77 (a), (b)), were applied to them.

Table 8 shows the bandwidth, number of tones, PAPR, and average power of the signals measured (all signals have a spacing tone of 5 kHz and used 16-QAM modulation).

Table 8. Characteristics of the OFDM signals measured with VSNA and VSA

BW (MHz)	Number of tones	PAPR (dB)	Avg Power (dBm)
10	2000	9.43	4.31
20	4000	9.24	4.07
100	20 000	10.78	3.25
120	24 000	11.40	2.49

Table 9 shows the average value of the SNR and EVM obtained after applying the calibration corrections. They exhibit a weak dependence on the signal bandwidth with a slight EVM increase with the signal bandwidth. The VSNA exhibits a smaller EVM and larger SNR by about 10 dB each, respectively, than the VSA for all signal bandwidths.

Table 9. Average EVM and SNR obtained with the VSNA and VSA

BW	VSNA / VSA							
	10 (MHz)		20 (MHz)		100 (MHz)		120 (MHz)	
avg SNR (dB)	43.29	29.76	43.02	29.40	40.94	28.52	41.08	27.50
avg EVM (dB)	-45.15	-35.91	-44.68	-34.38	-40.81	-29.12	-40.61	-27.37
avg EVM (%)	0.55	1.60	0.58	1.90	0.91	3.49	0.93	4.28

Chapter 5. Multiple input single output PAs

This chapter will explain the necessity to improve the PA DE at backoff power and the different techniques used to accomplish it. It will expose the most used PA configurations working under the load modulation principle. It will develop a synchronous multiport testbed using the SA option of the VNA to characterize dual-input single-output PAs. The calibration and post-processing required to demodulate the signal correctly will be detailed. It will extract the static and dynamic behaviors of the Hybrid Doherty Outphasing PA (HD-OPA) designed in the Microwave Lab at The Ohio State University with the proposed testbed. It will compare the measurement results with the Harmonic Balance simulation results. Moreover, its linearization using indirect learning architecture will be performed.

5.1 Introduction

The DE of a single-stage PA depends on the conduction angle of the drain or collector current, which is established by the quiescent point, and relies on the harmonic termination design, as are the cases of class J and F PAs.

In modern communication systems, advanced modulations are developed to use the bandwidth and reduce interference efficiently. The OFDM is one of the most commonly used, but the resulting modulated waveform has high PAPR. As a result, the single-stage PA can exhibit a high efficiency at peak power but not at backoff power, where the PA operates most of the time. Figure 78 shows the Probability Density Function (PDF) of different communication standards versus backoff power and the normalized drain efficiency of a conventional class AB PA. From Figure 78 it is noticed that for an LTE signal with a PAPR around 13 dB, a class AB PA will exhibit a DE approx of 24 %, while for an 802.11b signal with PAPR of 7 dB, the DE will be around 40 %. It is also observed that only for the Global System for Mobile Communications (GSM) standard (where the PAPR is near 0 dB), the high DE of a conventional class AB is reached. Figure 78 demonstrates that a single-stage PA will exhibit an undesired low DE value at backoff for modulated signals with high PAPR.

For a given bias point, the power device works at its maximum efficiency when the

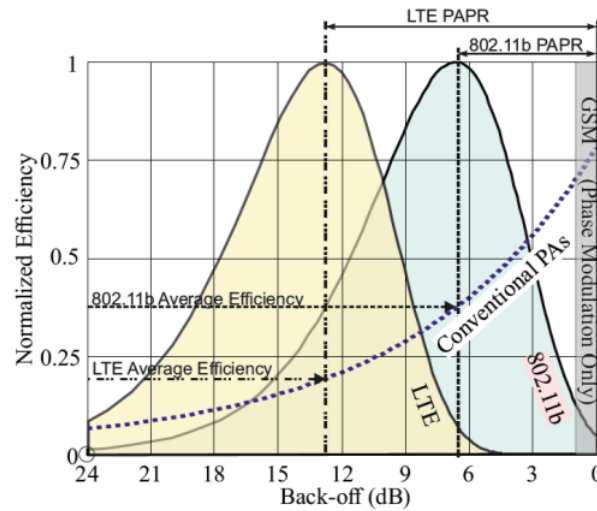


Figure 78. PDF of different communication standards versus backoff power.

voltage swing and the output current are maximized, which is displayed as the load line. These swings depend on the load RL (inverse of the load line slope) and the bias voltage of the drain VDD. Therefore, there is a load line for a given power level and drain current where the amplifier provides its maximum efficiency. Then it is noticed that to ensure high DE at any possible level of backoff; the load line must be changed depending on the input power, which is possible either by modulating the charge or the polarization as it is shown in figures 79 (a-b)

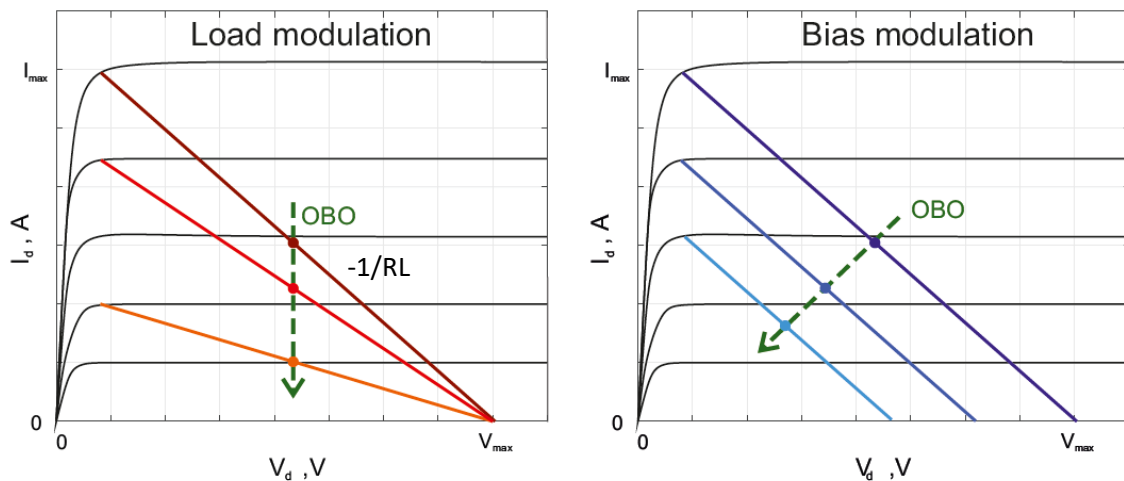


Figure 79. Techniques to enhance the DE at backoff power.

5.2 Load Modulation techniques

The major PA architectures that used the approach of load modulation are described below.

5.2.1 Single input Doherty PA

In Doherty (1936) the design of a two-stage PA to enhance drain efficiency in the backoff power under the load modulation principle is presented. The simplified diagram of a Doherty PA is shown in figure 80. It consist of a main PA working in class B or class AB, a peaking or auxiliary PA working in class C, two 90° transformers located at the input and output of the PA, and a power splitter to equally divide the input power (classical Doherty PA).

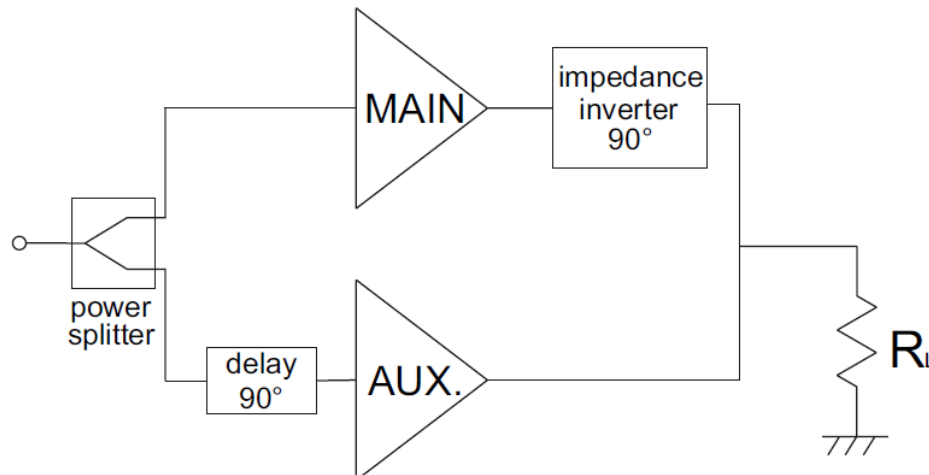


Figure 80. Single input Doherty PA diagram.

5.2.1.1 Operating principle

The impedance inverter located at the main PA output must guarantee the correct load modulation, which is in common-mode with the two amplifiers. The 90° delay at the auxiliary PA input is used to compensate for the phase shift generated by the immittance transformer ($\lambda/4$) located at the output of the main amplifier. To determine the impedance seen by the main and auxiliary PA (Z_M , Z_A , respectively), the simplified

schemes of figures 81 (a-b) are used, where $R_L = \frac{R_{opt}}{2}$, and R_{opt} the optimal impedance of a class AB or B PA.

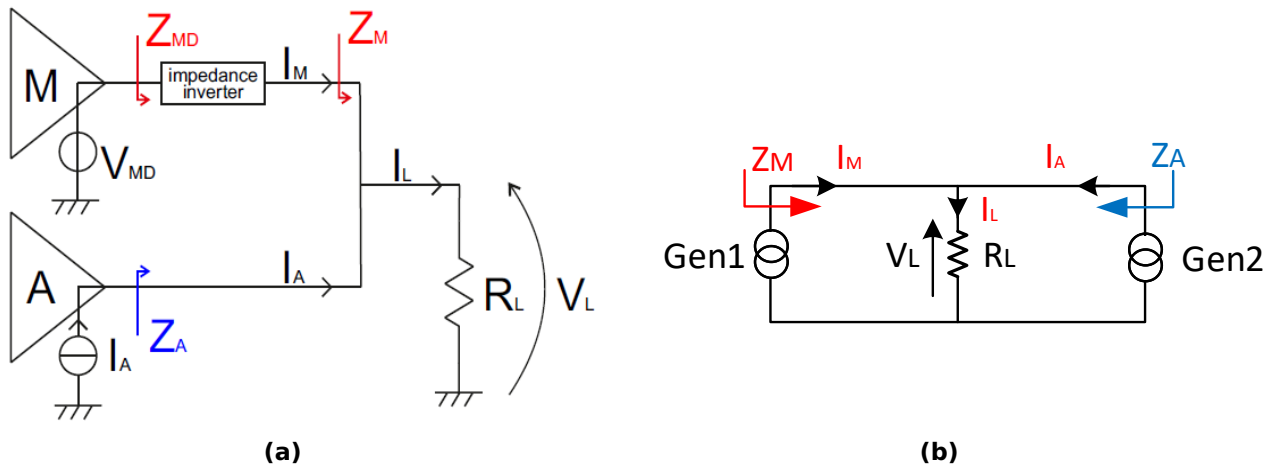


Figure 81. Simplified Doherty PA diagram.

$$V_L = (I_M + I_A)(R_L)$$

$$Z_M = \frac{V_L}{I_M} = (R_L) \left(1 + \frac{I_A}{I_M} \right) \quad (119)$$

$$Z_A = \frac{V_L}{I_A} = (R_L) \left(1 + \frac{I_M}{I_A} \right) \quad (120)$$

Z_M , Z_A are obtained from equations 119 and 120, respectively, where it is appreciated that when the auxiliary PA is theoretically off ($I_A = 0$) $Z_M = R_L$, and $Z_A = \infty$. When it turns on, it injects current into the load (R_L), contributing to the total power and modulating the impedance seen by the main PA. When both currents (I_M , I_A) are equal $Z_M = Z_A = 2R_L = R_{opt}$.

In the Doherty scheme, the main amplifier is designed to maintain its maximum swing in the voltage between the backoff power level and peak power, and therefore it is possible to maintain the maximum efficiency in this entire region. The $\lambda/4$ inverter, together with the current of the auxiliary amplifier, makes the main PA maintain the maximum voltage swing in the range of power levels between backoff and peak power.

5.2.2 Dual-input Doherty PA

A variant of the classic Doherty was presented in Darraji *et al.* (2016), where the power divider of the scheme shown in Figure 81 is replaced by two independent inputs RF sources (Figure 82). This option offers the possibility of carrying out an adaptive power divider, allowing the levels of the input signals to be adjusted so as not to waste backoff power and obtain a significant efficiency improvement. However, as can be seen, this scheme is more complex and expensive, and it is only used in macro base stations for medium and high power.

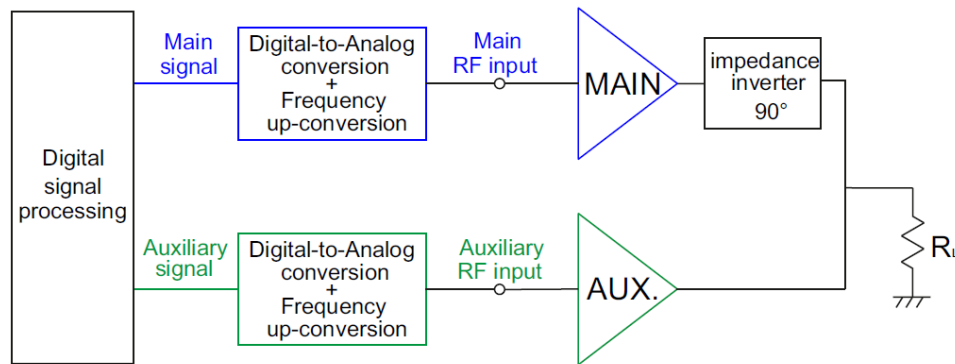


Figure 82. Dual-input Doherty PA.

5.2.3 Chireix PA

The Chireix configuration is another option to improve backoff efficiency and was proposed in 1935 by its inventor Chireix (1935). The two amplifiers are replaced by two ideal voltage sources for its analysis, with equal magnitudes and out of phase, connected in differential mode to a load R as shown in the figure below. The impedance seen by each amplifier Z_1 and Z_2 , shown in equations (121) and (122) are dependent on the phase difference (θ) between both input signals of the PA.

$$I_R = \frac{V_2 - V_1}{R} = \frac{V(e^{j\theta} - e^{-j\theta})}{R} = \frac{2jV \sin(\theta)}{R}$$

$$Z_1 = \frac{V_1}{I} = \frac{R}{2}(1 - \cot(\theta)) \quad (121)$$

$$Z_2 = \frac{V_2}{I} = \frac{R}{2}(1 + \cot(\theta)) \quad (122)$$

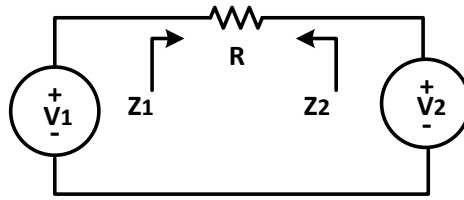


Figure 83. Simplified scheme of Chireix PA.

It is observed that the real part of the impedance remains constant with a value equal to $R/2$ for all outphasing values (θ), while the imaginary part changes as θ vary. For $\theta = 0^\circ$ both amplifiers see an open, while for 90° it is purely resistive. For other phase values, the impedances have a significant imaginary part, which brings about a reduction in backoff DE. An improvement is to introduce two reactive elements in parallel with the sources to decrease this reactive behavior.

5.3 Hybrid Doherty Outphasing PA (HD-OPA)

Another design variant to improve backoff efficiency is proposed in the paper, Liang *et al.* (2019b). The diagram of the Doherty Chireix hybrid amplifier with two inputs is shown in Figure 84. This configuration consists of the main amplifier operating in class F and the auxiliary in class C, which operates in Doherty mode at low powers and outphasing mode at high power. This hybrid amplifier is based on the changes in the phase difference between the input signals as the input power varies to maintain the correct operation of the load modulation.

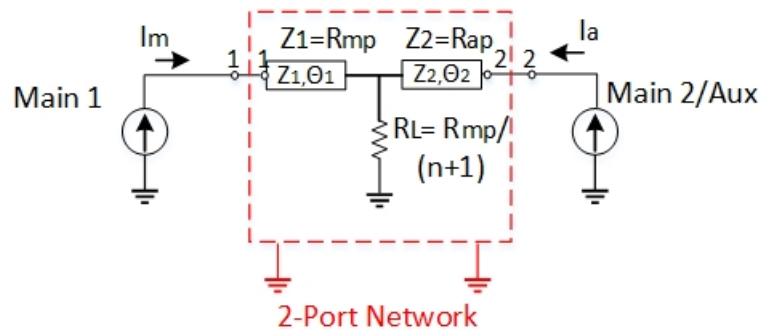


Figure 84. Hybrid Doherty-Chireix outphasing PA scheme

In the following subsections, the static and the dynamic characterizations of this

hybrid Chireix-Doherty PA are performed.

5.3.1 HD-OPA characterization

Figure 85 shows the HD-OPA, whose design and operating principle is reported in Liang *et al.* (2020). The main and peaking PAs are operating in class F and class C, respectively. This PA uses two GaN HEMTs transistors CGH40010 10-W from Cree Inc. The PA passive circuits are built on a Rogers RT Duroid 5880 substrate with $\epsilon_r = 2.1$. The designed frequency is 2.1 GHz.

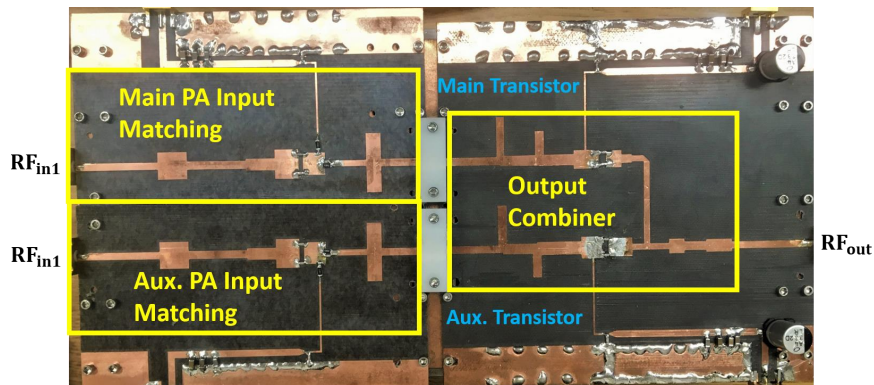


Figure 85. Hybrid Doherty Outphasing PA Liang *et al.* (2019b) used to demonstrate the multi-channel application of the VSNA.

5.3.2 Input signal alignment required for OPA characterization

For the characterization and linearization of dual-input OPAs, additional measurement and synchronization steps are required to align the two CW modulated RF signals applied at the input reference planes of the VSNA testbed (see green dashed lines in Figure 78). Indeed the operation of dual-input OPAs is critically dependent on the outphasing angle θ between the input signals as well as the absolute amplitudes (input powers) of the two input signals.

The two channels in the AWG are already internally synchronized and phase locked, which eliminates the synchronization issue. However, as shown in Figure 78, they are connected to the inputs of the DUT (HD-OPA) via different driver PAs, isolators, and cables. These different devices operated in their linear mode exhibit different power gains, RF phases, and group delays. A set of measurements and tuning is needed to

fully characterize and compensate for any difference in input powers, RF phases, and group delays of the signals applied at the two OPA inputs.

Given that the five receivers in the VSNA (PNA-X) are phase locked and perform the data acquisition in synchronicity, the VSNA can be used to perform the source alignment and thus measure and compensate for any difference in RF phases and group delays in the input signals. Indeed the LO phases $\Delta\phi_{LO}^r$ and the group delays $\Delta\tau^r$ measured for each channels r are found to be locked to one another owing to the PNA-X architecture.

Also, to ensure the correct absolute power levels applied at the inputs of the dual-input PA in CW measurements, adjustments to the average power level provided by the two channels of the AWG are needed and performed using the VSNA. This is done by sweeping the AWG power until the difference between the expected input power level and the measured values becomes less than 0.3 dB.

5.3.3 CW measurements used to acquire the OPA LUT

The HD-OPA, which operates in a mixed model, is to be driven at its two inputs by two RF signals with specific outphasing angle and input power levels for each output power level. The relationships between the OPA output power and the input power levels and outphasing angle θ are stored in a LUT, which is used for the subsequent operation of the OPA with modulated signals. A preliminary LUT is determined during the OPA design, but it benefits from being optimized through CW swept measurements after the OPA fabrication to account for fluctuations in device characteristics, transistor model accuracy, and circuit fabrication imperfections. The final LUT selected by the PA designer usually involves a tradeoff between linearity, gain and output power.

For the CW measurements used to determine the optimal LUT, the VSNA testbed is configured to operate with a frequency span of 10 Hz centered at 2.08 GHz and a resolution video bandwidth (RBW) of 1.25 kHz. The averaging factor is set to 50 to reduce the noise floor and improve each receiver's DR. In this mode, the VSNA operates like a VNA except that the calibrated amplitudes and phases of the incident and reflected waves are acquired at the five receivers instead of their ratios (hot S-parameters).

Figure 86 presents a flowchart of the steps followed to measure the PA with the CW stimuli. The main amplifier is biased with 25 V DC Drain voltage and 55 mA DC

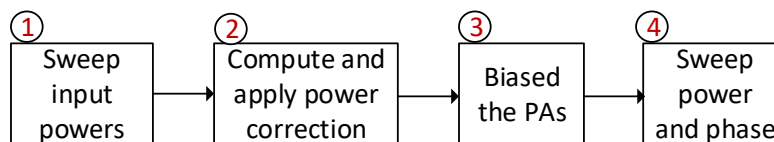


Figure 86. Flowchart for CW measurements.

quiescent current, while for the peaking PA, the DC bias voltages for the gate and drain are set to -4.1 V and 25 V, respectively. To compute the DE and the PAE, the DC Drain currents are automatically measured each time the outphasing angle and power levels are changed while the incident and reflected waveforms are simultaneously recorded from the VSNA receivers at 2.08 GHz.

The DE obtained at each point of the sweeps are displayed in Figure 87.

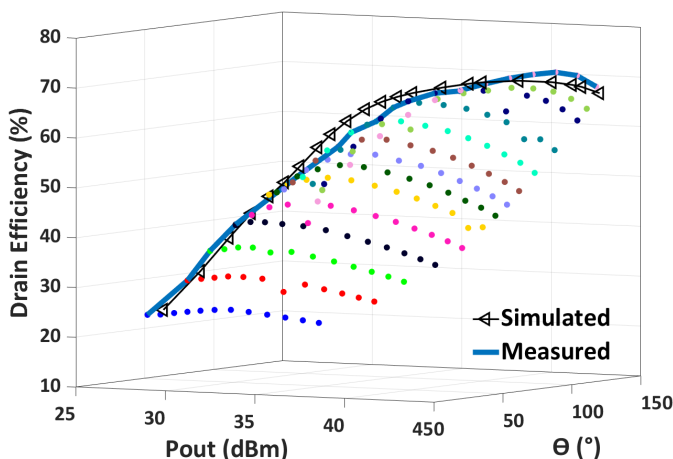


Figure 87. Drain efficiency (%) versus P_{out} (dBm) and outphasing angle ($^{\circ}$).

The dots with the same color correspond to the DE values associated with the variation of the outphasing angle θ from 20° to 130° while keeping the same input power. A single group of swept incident power and input phase offset measurements consisting of 12 phases and 14 incident power levels (for a total of 168 measurements) was typically conducted in less than 4 minutes.

The blue line in Figure 87 is the selected response which achieves the highest drain efficiency behavior for the PA for each output power, while the black line is the best DE obtained when performing the harmonic balance simulations of the HD-OPA using

Keysight ADS.

The associated input power levels $P_{in,1/2}$ and outphasing angle θ (blue line in Figure 87) required to drive the HD-OPA for each targeted output power P_{out} , are stored in the LUT given in Table 10.

Table 10. LUT of the HD-OPA for maximum efficiency.

P_{out} (dBm)	$P_{in,1}$ (dBm)	$P_{in,2}$ (dBm)	θ (degree)	ϕ_{OPA} (degree)
27.38	13.71	11.36	21.04	-51.83
29.51	16.21	13.87	22.50	-51.22
31.03	17.95	15.69	19.15	-52.68
32.21	19.41	17.03	22.33	-50.81
34.29	21.91	19.83	32.82	-43.14
34.83	22.56	20.73	32.91	-41.59
36.36	23.83	22.28	42.88	-35.39
38.68	25.60	24.93	52.72	-28.54
40.25	26.73	26.94	62.23	-24.56
42.76	28.40	29.82	100.69	-16.62
43.26	28.39	29.81	110.69	-16.34
43.69	28.39	29.81	120.69	-16.10
43.99	28.38	29.80	130.69	-16.10

The highest efficiency value of 72.05 % is obtained when the output power is equal to 43.26 dBm, which is 1.15 % bigger than the DE obtained from simulation (black line). The measured and simulated saturation efficiencies are 68.58 % and 68.84 %, respectively. The measured 9-dB backoff efficiency is approximately 53% (2 % smaller than the simulation). In summary, the highest backoff efficiency is exhibited from the simulation, while the highest power level and DE value are obtained during the measurements.

Figure 88 shows the optimal outphasing angles obtained from the simulation (black circles) and the measurements (pink plus), for which the maximum DE of the PA is reached.

A good correlation between them is observed. It is worth noting that for low output powers (below backoff), the optimal outphasing angle is best kept constant. The optimal outphasing angle begins to change at an output power of 34 dBm, approximately corresponding to the 9 dB backoff. Since the peaking PA working in class C turns off for output power levels lower than 35 dBm. In this power region, only the main PA remains operating. Figure 89 shows the DC powers $P_{in,1}$ and $P_{in,2}$ in Watts consumed

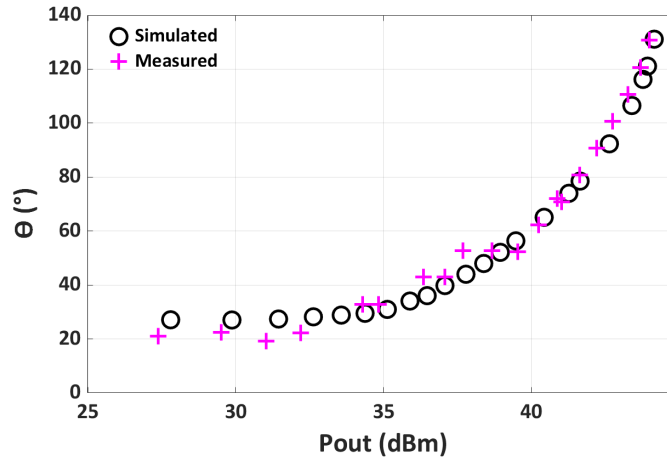


Figure 88. Optimal simulated and measured outphasing angles θ ($^{\circ}$) versus P_{out} (dBm) at ω_0 .

by each PA.

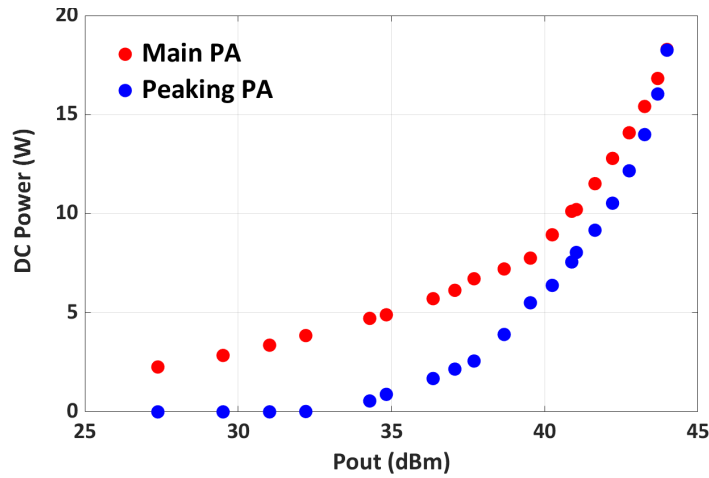


Figure 89. Optimal measured DC Power (W) versus P_{out} (dBm) for the main (red circles) and peaking (blue square) PAs at ω_0 .

An evaluation of the bandwidth of the HD-OPA can also be performed by calculating the drain efficiency versus output power at different frequencies within the 120 MHz span considered in this work. The DE (%) is plotted versus P_{out} (dBm) from 2.0 to 2.12 GHz in Figure 90. Also plotted is the fractional dissipated power ($1 - DE$) (%)

One of the benefits of the testbed is acquiring the reflected waveforms at the input ports of the PA. This permits the user to compute the effective power Gain and the PAE using the input powers at both ports defined as:

$$P_{in,1}(\omega_0) = \frac{1}{2} [|a_1(\omega_0)|^2 - |b_1(\omega_0)|^2],$$

$$P_{in,2}(\omega_0) = \frac{1}{2} [|a_2(\omega_0)|^2 - |b_2(\omega_0)|^2],$$

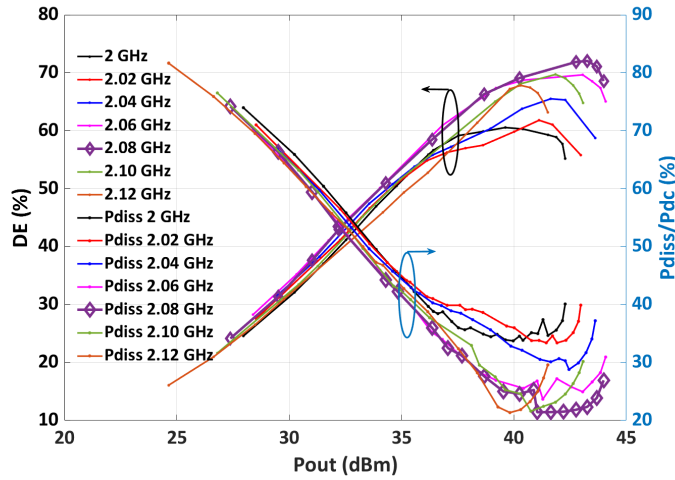


Figure 90. Drain efficiency (%) and dissipated power (%) versus P_{out} (dBm) within the 120 MHz frequency span of this HD-OPA.

where $a_i(\omega_0)$ and $b_i(\omega_0)$ refer to the incident and reflected waves measured at the input reference planes $i = 1$ or 2 at the center radial frequency ω_0 .

The effective power Gain is calculated as described by equation (123), where P_{out} and $P_{in,i}$ are the output and input powers, respectively:

$$G_{OPA}(\text{dB}) = 10 \cdot \log_{10} \left(\frac{P_{out}}{P_{in,1} + P_{in,2}} \right), \quad (123)$$

$$G_{OPA}^{\text{SYS}}(\text{dB}) = 10 \cdot \log_{10} \left(\frac{P_{out}}{\frac{1}{2} (|a_1|^2 + |a_2|^2)} \right). \quad (124)$$

Note that the alternate G_{OPA}^{SYS} in equation (124) is the overall power Gain of the OPA-plus-isolator system, given that isolators are placed between the driver PAs and the two inputs of the HD-OPA (see Figure 78).

Figures 91 (a-g) show the, $G_{OPA}(\text{dB})$, (red dots) G_{OPA}^{SYS} (blue dots), obtained for frequencies between 2 GHz and 2.12 GHz, for different outphasing angles versus output power. From Figure 91 (c) and (d), it can be noted that the input matching network exhibits a better behavior at these frequencies (2.04 GHz and 2.06 GHz), where the reflected waveforms at the inputs are almost zero.

Figure 92 shows the two defined OPA gains at the selected frequency (2.08 GHz), computed with the incident (blue dots) and input powers (red dots).

Where the purple circles represent the Gain of the OPA when the highest DE of Fig-

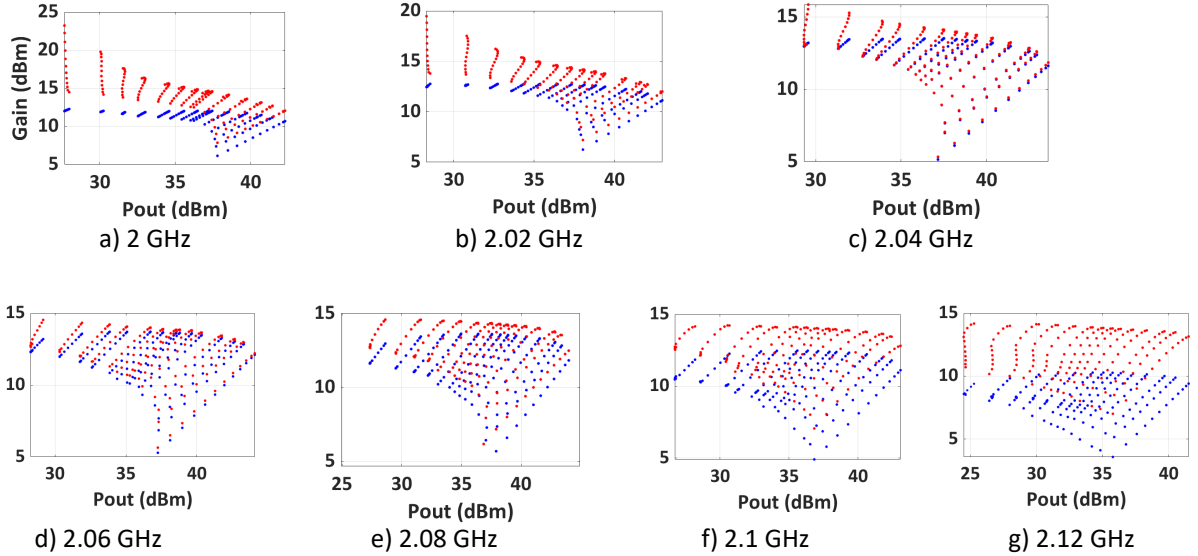


Figure 91. Gain (dB) versus P_{out} (dBm) for different frequencies.

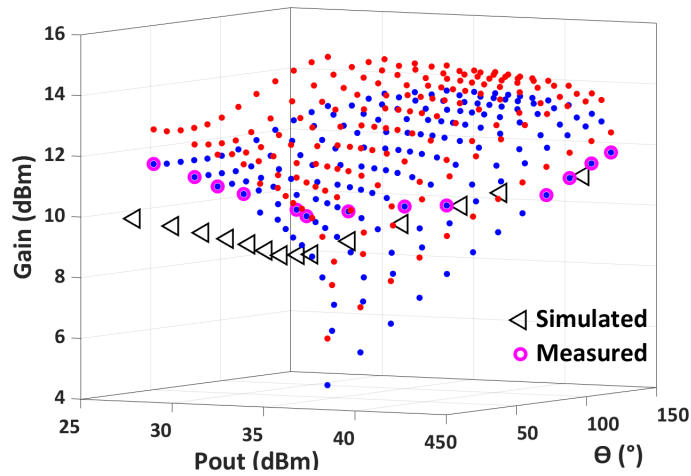


Figure 92. Gain (dB) versus P_{out} (dBm) and Outphasing angle θ ($^{\circ}$).

ure 87 is selected. The black triangles depict the Gain obtained from the simulation. The discrepancy between measurement and simulation can originate from differences between the input impedances of the nonlinear transistor model and the actual transistors used in the design.

Since both the incident and reflected powers at the OPA inputs are available, the PAE can also be calculated. The PAE of the dual-input OPA is given in terms of the RF Gain as indicated in equation (125):

$$\text{PAE}(\%) = \frac{P_{out} - P_{in,1} - P_{in,2}}{P_{DC,1} + P_{DC,2}} = \frac{P_{out} \left(1 - \frac{1}{G_{OPA}}\right)}{P_{DC,1} + P_{DC,2}}, \quad (125)$$

where $P_{DC,1}$ and $P_{DC,2}$ are the DC power consumed by the main and peaking PAs, respectively. The PAE of the dual-input PA is plotted versus P_{out} (dBm) and the outphasing angle ($^\circ$) in Figure 93. The blue line is the experimental response which achieves the highest PAE while the black is the best PAE obtained from harmonic balance simulations.

The PAE provides a more realistic figure-of-merit of the PA in terms of power consumption. This is one of the advantages of using the proposed multi-channel VSNA configuration when characterizing a dual-input HD-OPA. The proposed multi-channel

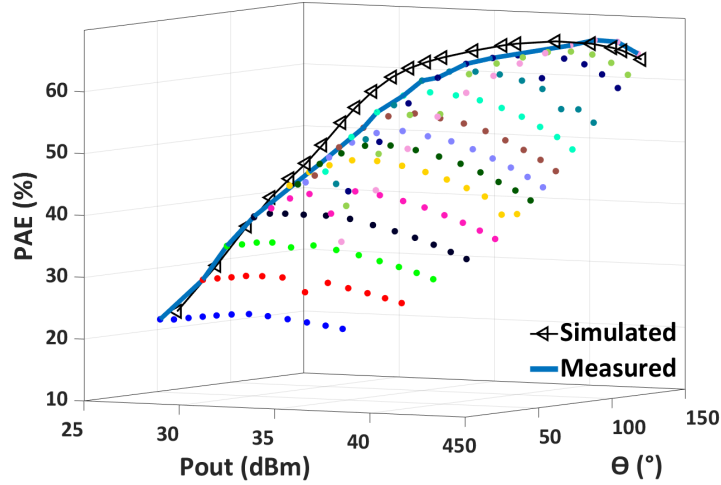


Figure 93. PAE % versus P_{out} (dBm) and outphasing angle ($^\circ$).

VSNA testbed also allows one to compute the common-mode group phase φ_{OPA} of the OPA which is defined under CW operation as the power dependent difference between the phase of the OPA output waveform ϕ_{out} and the average phase of the two OPA input signals:

$$\varphi_{OPA}(P_{out}) = \phi_{out} - \left[\frac{\phi_{x_1} + \phi_{x_2}}{2} \right]. \quad (126)$$

The resulting OPA group phase versus output power calculated from the CW measurements at ω_0 is shown in Table 10. This group phase can then be applied to the input signal $x(n)$ to remove the static AM-PM distortion:

$$x'(n) = |x(n)| \exp^{[j(\phi_x - \varphi_{OPA}(P_{out}(n)))]}$$

This upfront phase distortion correction can simplify the subsequent dynamic linearization by reducing the required DPD coefficients.

5.3.4 HD-OPA characterization using modulated signals

OFDM signals with a periodicity of 200 μs were generated in Matlab with a bandwidth of 10 MHz and 20 MHz to obtain the dynamic behavioral model of the HD-OPA a sampling frequency of 600 MHz and a PAPR of 9.2 dB and 9.9 dB, respectively.

The LUT in Table 10 which provides the highest DE is applied in Matlab to the input OFDM modulated signal $x(n) = |x(n)| \exp[j\phi_x(n)]$ expressed in discrete time n to generate the signals $x_1(n)$ and $x_2(n)$ at the inputs of the main and peaking PA according to:

$$\begin{aligned} x_1(n) &= \sqrt{P_{in,1}[P_{out}(n)]} \exp^{j(\phi'_x(n) + \frac{1}{2}\theta[P_{out}(n)])}, \\ x_2(n) &= \sqrt{P_{in,2}[P_{out}(n)]} \exp^{j(\phi'_x(n) - \frac{1}{2}\theta[P_{out}(n)])}, \\ \text{using } \phi'_x(n) &= \phi_x(n) - \varphi_{OPA}(P_{out}(n)), \end{aligned}$$

where $P_{in,i}[P_{out}]$ are the incident powers at the input ports i and $\theta[P_{out}]$ the outphasing angle between the two inputs. Note that these input signals ensure a high Drain efficiency OPA operation while implementing a preliminary AM-AM and AM-PM linearization.

Figure 94 gives a flowchart of the steps followed to acquire the dynamic behavior of the OPA with the VSNA for power calibrated modulated signals.

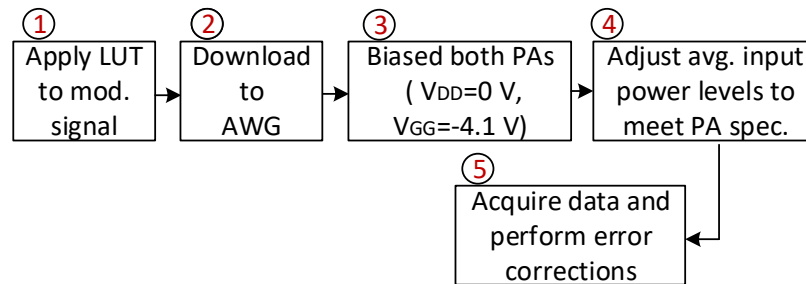


Figure 94. Flowchart describing the error correction applied in post-processing to the raw data to obtain the calibrated dynamic behavior of the OPA modulated signals.

The fifth step in Figure 94 was described in more details in Figure 71. For clarity, red boxes are used to indicate that the signal processing is done in the frequency domain, while blue boxes are used for processing in the time domain.

The proposed VSNA allows the user to acquire the static (CW) and dynamic (OFDM

signal) behaviors of a dual-input OPA with the same testbed without breaking electrical contact with the DUT.

Figures 95 and 96 draw the AM-AM, AM-PM, Gain, the output spectrum, and the IQ-constellation of the PA. using a 10 MHz and 20 MHz OFDM signals with 16 QAM modulation and 9.21 PAPR and 9.9 dB, respectively, when the LUT that describes the behavior of high efficiency is selected. It is noted that the dynamic gains follow the one extracted with CW signals, represented with red stars in Figures 95 (c) and 96 (c).

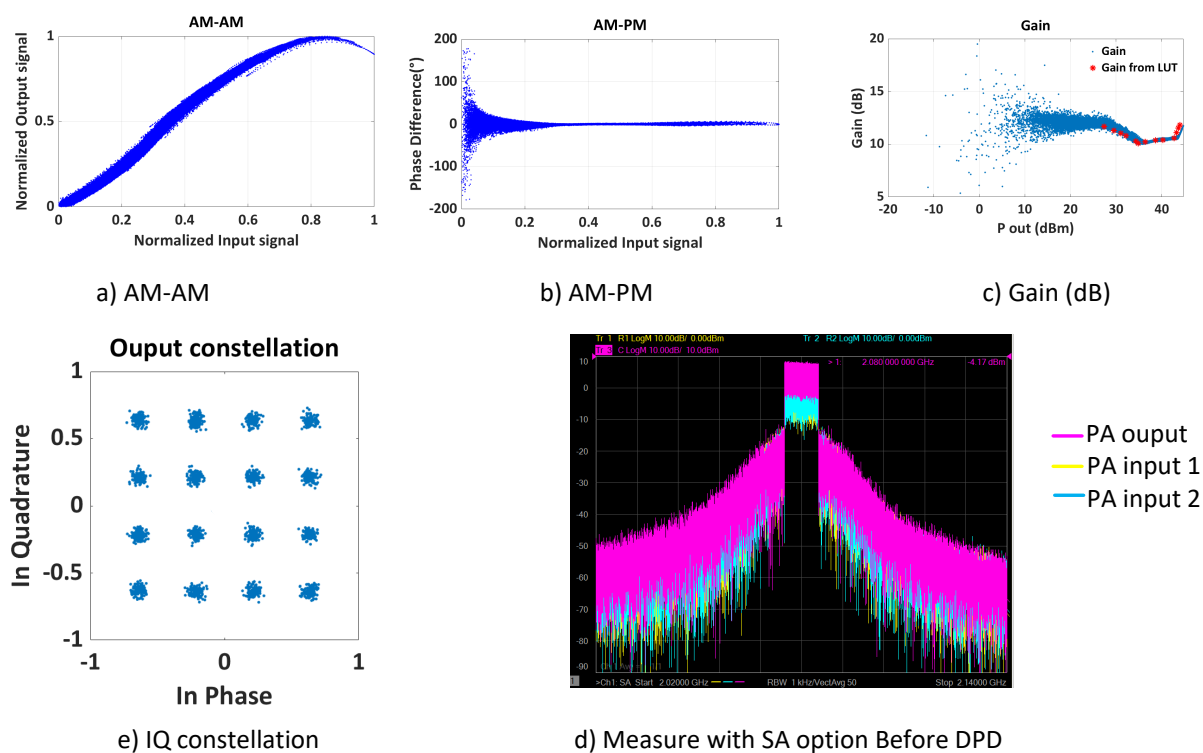


Figure 95. HD-OPA Dynamic Behavior with an OFDM 10 MHz signal.

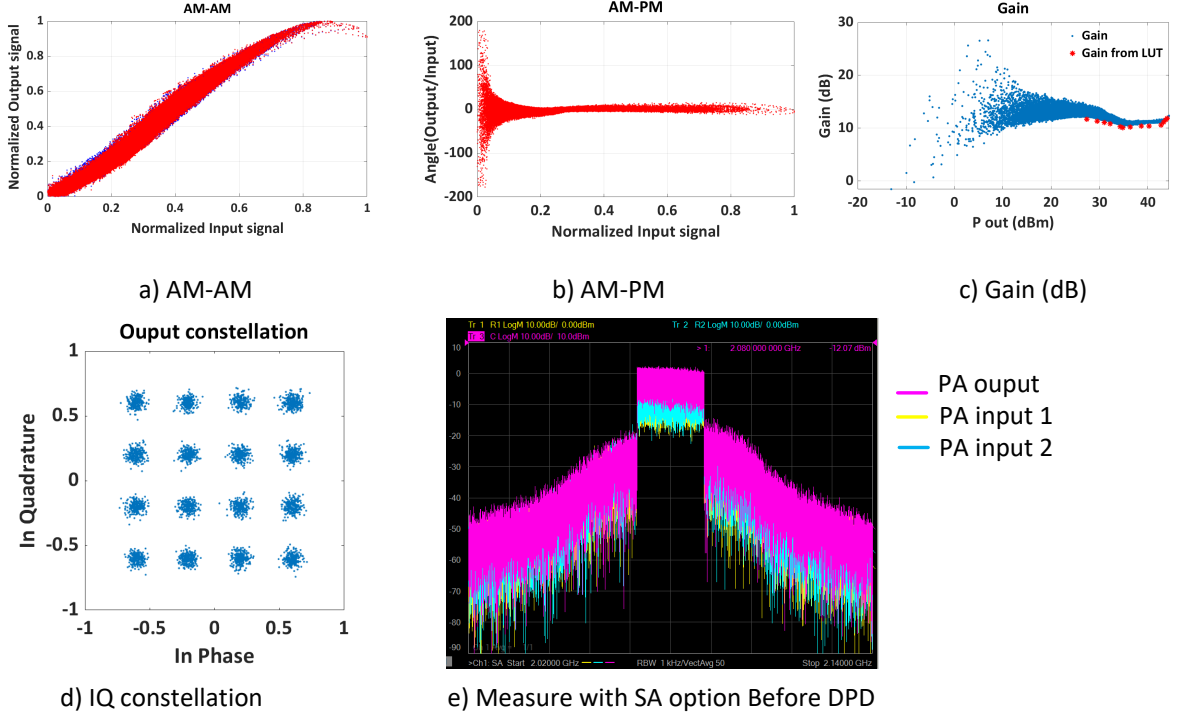


Figure 96. HD-OPA Dynamic Behavior with an OFDM 20 MHz signal.

5.3.5 Linearization results

Thanks to its IF phase calibration, the proposed VSNA (PNA-X with enhanced SA option) allows one to capture the dynamic response of multi-input multi-output devices in the time domain. It is thus possible to perform the time domain linearization of the OPA being characterized.

The HD-OPA linearization was performed by predistorting the original input signal $x(n)$ using the indirect learning technique. The input data $x(n)$ is modeled using Eqn. (127) in terms of the output data $y(n)$ using generalized memory gain functions $G_p^m(\dots)$ with a memory depth M equal to 4 and cross term depth P equal to 4:

$$x(n) = \sum_{m=0}^{M-1} \sum_{p=0}^{P-1} G_p^m(|y(n-m-p)|^2) y(n-m). \quad (127)$$

The gains G_p^m are expressed in terms of a linear superposition of the cubic-spline basis reported in Naraharsetti *et al.* (2015). The predistorted modulated time domain data

$z(n)$ presented to the OPA LUT is then given by:

$$z(n) = \sum_{m=0}^{M-1} \sum_{p=0}^{P-1} G_p^m (|x(n-m-p)|^2) x(n-m).$$

A diagram showing the location of the DPD block relative to the OPA LUT is given in Figure 97.

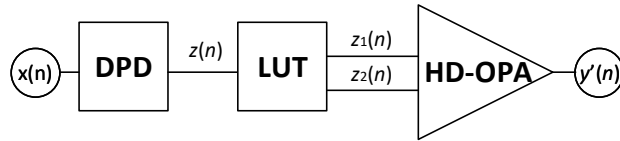


Figure 97. Simplified diagram of the integration of the DPD with the OPA LUT.

The predistorted LUT waveforms are applied to the OPA and recorded with the VSNA. The AM-AM and AM-PM responses of the HD-OPA before DPD (blue dots) and after DPD (red dots) are shown in Figure 98 (a) and (b), respectively. Nonlinearities and memory effects introduced by the HD-OPA are observed to be significantly reduced after time domain predistortion. Figure 99 (a) shows the signals at the output of the PA before

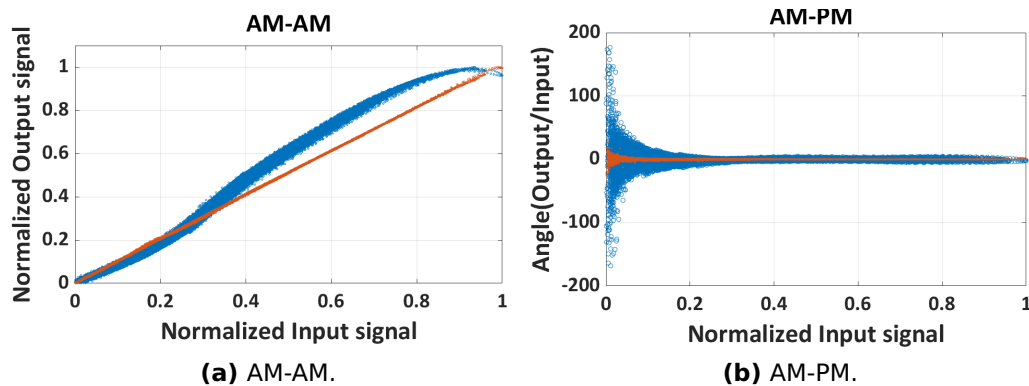


Figure 98. AM-AM and AM-PM of the HD-OPA before and after the DPD, for a 10 MHz BW signal.

(blue dots) and after the DPD (red dots). Figure 99 (b) shows the input and output signal spectra observed in the SA-PNA-X. From Figures 99 (a-b), it is appreciated that after the linearization an ACPR improvement of about 24 dB is obtained.

Figures 100 (a-b) and 101 show the AM-AM, AM-PM curves, and the output spectra, respectively, obtained for a 20 MHz signal before and after the DPD.

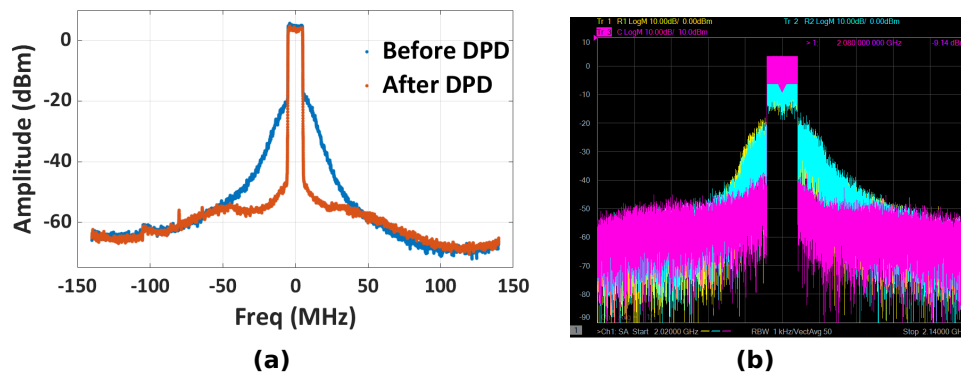


Figure 99. Output spectra observed in (a) Matlab, (b) SA-PNA-X for a 10 MHz BW signal.

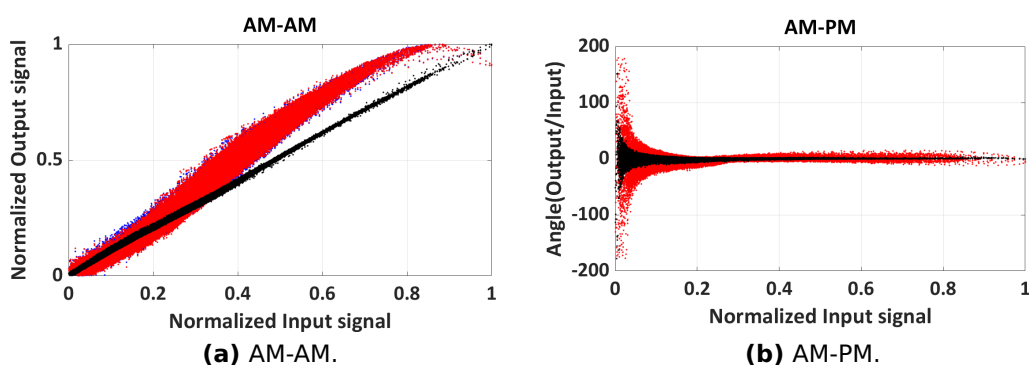


Figure 100. AM-AM and AM-PM of the HD-OPA before and after the DPD, for a 20 MHz BW signal.

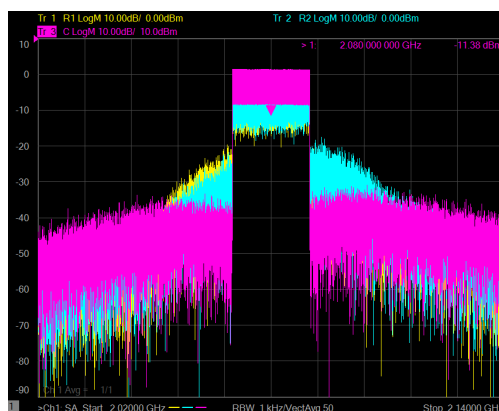


Figure 101. Output Spectrum observed in the SA-PNA-X for a 20 MHz BW signal.

Another benefit of the VSNA testbed is the possibility to compute the in-band distortion with the EVM. Figure 102 displays the IQ constellations of the received 16 QAM OFDM signal with bandwidths of 10 MHz, (a) before DPD, (b) the original input signal

(red circles), and the output signal after linearization (blue plus). A constellation EVM of 0.31 % is achieved after DPD.

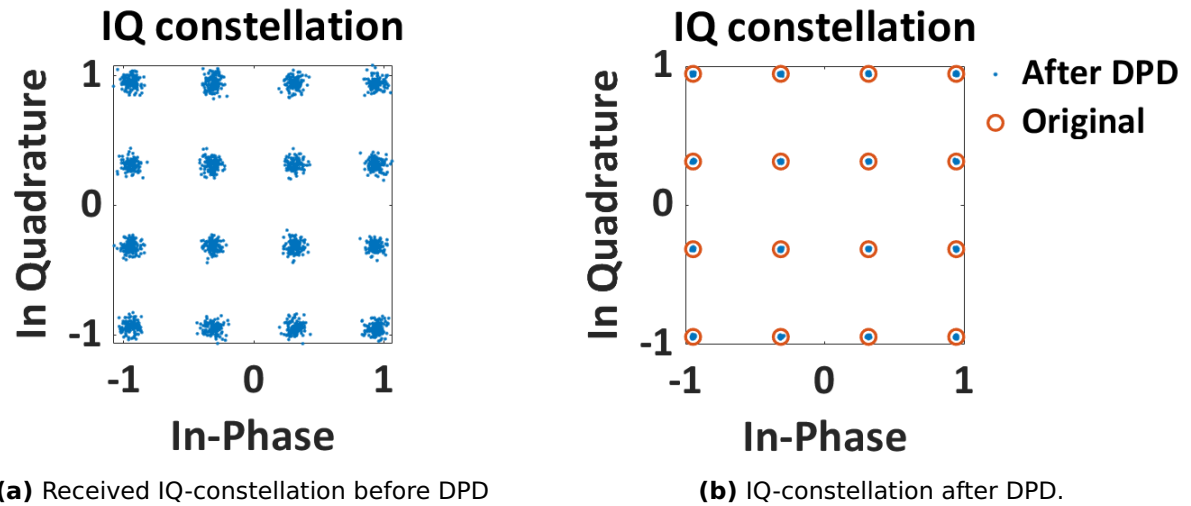


Figure 102. IQ constellations for a 16 QAM OFDM signal of 10 MHz BW.

Tables 11 and 12 summarize the figures of merit values obtained for two modulated signals with a bandwidth of 10 MHz and 20 MHz and PAPR of 9.21 and 9.90 dB, respectively.

Table 11. Figures of merit obtained with a 10 MHz OFDM signal.

Measurement Conditions	PAPR (dB)	$ACLR_{L,H}$ (dBc)	NMSE (dB)	EVM (%)	DE (%)
Output w/o DPD	8.33	-28.76,-26.57	-21.36	5.11	56.50
Output w DPD	9.02	-53.54,-53.93	-44.80	0.31	50.96

Table 12. Figures of merit obtained with a 20 MHz OFDM signal.

Measurement Conditions	PAPR (dB)	$ACLR_{L,H}$ (dBc)	NMSE (dB)	EVM (%)	DE (%)
Output w/o DPD	9.08	-27.64,-23.69	-19.88	5.79	51.12
Output w DPD	9.45	-42.97,-44.01	-36.54	0.73	49.93

Additionally, the average DEs and the ACLR (defined as shown in Figure 103, and computed as indicated in equation (128)), are displayed.

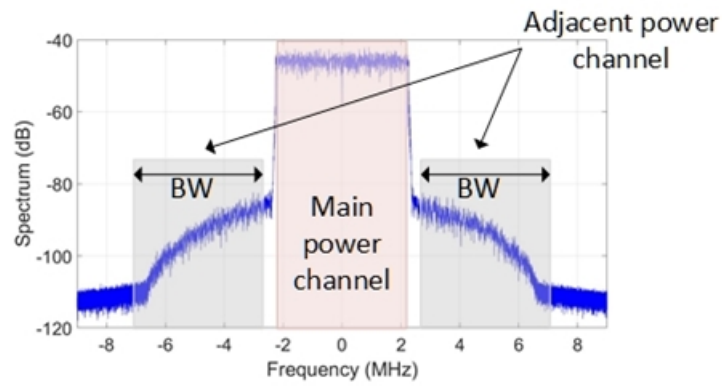


Figure 103. Adjacent Channel Leakage Ratio

$$ACLR(dBc) = 10 \cdot \log_{10} \left(\frac{P_{adj}}{P_{main}} \right) \quad (128)$$

The tables also show that the input and output PAPRs are nearly the same after DPD. Also, good NMSEs and EVMs were obtained after linearization. The DEs exhibit a reduction of around 5 % after DPD for the 10 MHz bandwidth signal, while for the 20 MHz signal, the reduction is around 1.18 %.

These results demonstrate that the VSNA enables the user to rapidly characterize an OPA and evaluate its linearization performance with a time domain linearization with the same testbed.

Chapter 6. Conclusions and future work

A system using GRC software and a Universal Software Radio Peripheral board to characterize a microwave power amplifier with multitone signals was developed. The main advantage is that this testbed does not require an AWG or to purchase the multitone option for a generator. The calibration presented allows to obtain the measurements in the reference plane of the DUT, thus providing the designers access to the linearity performances of the devices. The PNA-X-5245A does not require extra options like a SA. This makes our measurement system less expensive. Furthermore, GRC is an open source software that runs on Linux OS. As a result, the testbed is fully automated, and it can be used to teach or introduce RF students to understand LP measurements under realistic signals. Moreover, it can be operated remotely. Therefore it can be used to set up a virtual lab. It is easier to implement than the others LP setup mentioned in this dissertation. It does not require to pre-characterize the passive tuners. The daughterboard helps to lower the cost of the whole setup. The frequency offset mode allows obtaining the relative phase between the input and output of the device, so the AM/PM can be computed. Also, the low and high ACPRs are obtained for each load impedance, allowing to inspect the output spectral regrowth.

A novel VSNA (VNA+VSA) measurement scheme using a commercial 4-port VNA was proposed in this thesis to assist with the rapid and accurate characterization of the nonlinear response of dual-input OPAs under realistic large signal operation. The VSNA measurement scheme allows the user to obtain both the static and dynamic responses of dual-input OPAs in the time domain besides the frequency domain. Consequently, using the VSNA, the time domain DPD linearization of the OPA can also be performed. The VSNA system presented in this work relies on the SA option of the PNA-X VNA. It benefits from the large DR of its receivers and its ability to acquire the Fourier amplitudes and phases of periodic modulated signals. The VSNA mode extends that feature by adding an IF phase calibration on top of the RF calibration at the center frequency. This permits the testbed to correctly recover the modulated signals in the time domain by applying phase corrections in the frequency domain, which compensate for the IF transfer function of the VNA receivers. The signal constellation can then be recovered by synchronizing the measured signal to the original signal to extract the LO phase and group delay of the VNA receivers. The fidelity of the VSNA calibration

presented in this work was evaluated in the time domain and constellation domain using a 100,000 tones 64-QAM OFDM signal with a bandwidth of 500 MHz provided by a calibrated AWG. The measurement, which recorded 10,000 tones, was performed at sixteen-time the IF bandwidth of the VNA receivers. An NMSE of -46.50 dB, SNR of 46.49 dB, and a constellation EVM of 0.48 % were measured. Compared to a commercial VSA, the VSNA was verified to yield improvement in EVM measurements by up to 10 dB for OFDM signals with bandwidth up to 120 MHz (limited only by the license of the VSA used). The acquisition time for 24 000 tones signal testbed in this work was around a fraction of a second for a vector averaging of 50 and a frequency resolution of 1.25 kHz. Since, unlike the mixer-based NVNA mode that acquires each tone one at a time, the SA mode acquires them in bands of 30 MHz and performs a frequency band stitching transparent to the user. In this work, the proposed VSNA scheme was applied to characterize a dual-input GaN HEMT OPA. The LUT providing optimal drain efficiency was determined from VSNA measurements using CW signals on five channels which provided the OPA gains, PAE, and group phase. The VSNA was then used to characterize the OPA using 10 MHz and 20 MHz OFDM signals with 16 QAM modulation. The HD-OPA's dynamic AM-AM and AM-PM curves were obtained, and the NMSE and constellation EVM were calculated. The extraction of the behavioral model and the linearization of the OPA were then demonstrated using digital predistortion (DPD) at the baseband. In doing so, the VSNA was demonstrated for its ability to characterize and linearize a dual-input OPA using CW and modulated signals without breaking contact with the DUT. In summary, the phase calibration presented in this work for a commercial multiport mixer-based VNA made possible the demonstration of a new VSNA measurement mode which combines in a single instrument mode some of the attributes of both a multi-channel VSA and VNA. This VSNA mode enables the user to characterize multi-port devices with the rapid in-band acquisition of both CW and periodic broadband modulated signals without breaking contact with the DUT.

6.1 Future works

During this research, the SA option has been improved by Keysight, and a new update of the PNA-X synthesizer was done, replacing it with a Direct Digital synthesizer (DDS), which offers the lowest phase noise of the market. Moreover, the application

bandwidth has been extended to the full frequency span of the PNA-X. The enhanced SA option will be used to characterize multiple input nonlinear devices with wideband signals at fundamental and harmonic frequencies in future works.

Additionally, the IF receivers located in the rear panel of the PNA-X, will be used to measure lower frequency components. This allows performing real-time harmonic load-pull at low frequency. Therefore, the current and voltage waveforms can be obtained at the intrinsic current plane.

A third source named XSB is incorporated into the PNA-X, which has the capability to work with a wideband modulated signal from 10 MHz to 6 GHz. The XSB source will be used to identify the time-invariant phase and amplitude residual errors of each PNA-X receivers without using an external AWG.

6.2 Publications

(2021), **IEEE Transactions on Microwave Theory and Techniques**: “Time-Domain Characterization and Linearization of a Dual-Input Power Amplifier Using a Vector Network Analyzer as the Receiver.”

Abstract: A newly calibrated testbed based on a commercial vector network analyzer (VNA) is proposed for the fast in-band vector signal characterization and linearization of nonlinear multiport devices. The testbed can acquire both CW and wideband modulated periodic signals without breaking contact with the DUT, in up to five channels. The time-domain measurements are made possible by calibrating all the receivers in the frequency domain. This calibration provides a phase and amplitude correction for the modulation tones of all the incident and reflected waves in the acquisition bandwidth. The measurement bandwidth is determined at calibration by the bandwidth of the periodic OFDM signals used as a phase standard. It is independent of the VNA receivers' bandwidth. A 500-MHz 100 000-tones 64-QAM OFDM constellation is recovered with 0.48.

(2020), **RWW IEEE Tropical Conference on RF Power Amplifiers for Radio and Wireless Applications**: “Optimal Two-Way Hybrid Doherty-Outphasing Power Amplifier.”

Abstract: This paper presents a two-way hybrid Doherty-outphasing power amplifier (HD-OPA) with an optimal efficiency. The HD-OPA consists of a main PA operating in class-F and an auxiliary PA operating in class-C which jointly operate in the Doherty mode at lower power and the outphasing mode at higher power. The peak to backoff fundamental drain voltage ratio of the auxiliary PA is optimized such that the main and auxiliary transistors both deliver their maximum power at peak power. As a result, the outphasing angles between the two inputs need to be changed dynamically with the dual-input power level. This concept is validated by a fabricated 2.08 GHz PA demonstrator circuit with a drain efficiency of 71.1

(2019), **93th ARFTG Microwave Measurement Conference (ARFTG):** “Calibrated Digital Predistortion Using a Vector Network Analyzer as the Receiver.”

Abstract: This paper reports the first demonstration of the behavior modeling and predistortion linearization of a power amplifier (PA) for periodic modulated signals using a vector network analyzer (VNA) operated in the receiver mode. In this demonstration a PA operated at 2.3 GHz is characterized using a 5 MHz LTE signal with a peak-to-average power ratio (PAPR) of 10.2 dB. The phases of the Fourier spectrum of the periodic signal measured by the VNA receiver are calibrated using a 20 MHz OFDM signal. The calibrated phases and amplitudes of the 5 MHz LTE signal in the frequency domain are then used to reconstruct the signal in the time domain. After synchronization, the NMSE, dynamic AM-AM and AM-PM, ACPR, EVM, and BER of the PA before and after predistortion can then be calculated from the measured data. The predistortion linearization of the PA validates the accuracy of the VNA phase calibration and synchronization methodology used for the modulated waveforms. This work demonstrates that the same VNA and calibrated testbed can be used to characterize both the (1) continuous-wave (CW) and (2) modulated nonlinear response of a device without breaking electrical contacts with it.

References

(????). Technical report.

- Aboush, Z., Benedikt, J., and Tasker, P. (2004). High power harmonic active load-pull using broadband impedance transformers. In: *IEEE High Frequency Postgraduate Student Colloquium*. pp. 145–150.
- Aboush, Z., Jones, C., Knight, G., Sheikh, A., Lee, H., Lees, J., Benedikt, J., and Tasker, P. J. (2005a). High power active harmonic load-pull system for characterization of high power 100watt transistors. In: *35th European Microwave Conference 2005 - Conference Proceedings*. Vol. 1, pp. 609–612.
- Aboush, Z., Lees, J., Benedikt, J., and Tasker, P. (2005b). Active harmonic load-pull system for characterizing highly mismatched high power transistors. In: *IEEE MTT-S International Microwave Symposium Digest*. Vol. 2005, pp. 1311–1314.
- Alsahali, S., Gecan, D., Alt, A., Wang, G., Anera, S. M., Chen, P., Woodington, S., Sheikh, A., Tasker, P., and Lees, J. (2019). A novel modulated rapid load pull system with digital pre-distortion capabilities. In: *2019 93rd ARFTG Microwave Measurement Conference: Measurement Challenges for the Upcoming RF and mm-Wave Communications and Sensing Systems, ARFTG 2019*, jun. Institute of Electrical and Electronics Engineers Inc.
- Benedikt, J. and Tasker, P. J. (2002). High-power time-domain measurement bench for power amplifier development. In: *60th ARFTG Conference Digest: Measurements Needs for Emerging Technologies, ARFTG 2002*. Institute of Electrical and Electronics Engineers Inc., pp. 107–110.
- Benedikt, J., Gaddi, R., Tasker, P., Goss, M., and Zadeh, M. (2000). High power time domain measurement system with active harmonic load-pull for high efficiency base station amplifier design. In: *2000 IEEE MTT-S International Microwave Symposium Digest (Cat. No.00CH37017)*. IEEE, Vol. 3, pp. 1459–1462.
- Bouysse, P., Nebus, J.-M., Coupat, J.-M., and Villotte, J.-P. (1994). A novel, accurate load-pull setup allowing the characterization of highly mismatched power transistors. *IEEE Transactions on Microwave Theory and Techniques*, **42**(2): 327–332.
- Chireix, H. (1935). High power outphasing modulation. *Proceedings of the Institute of Radio Engineers*, **23**(11): 1370–1392.
- Choi, W., Nelson, S., Ferwalt, D., Mongia, R., Shichijo, H., and Kenneth, K. O. (2013). Three-harmonic time-domain load-pull measurement system with the 40-GHz maximum third order harmonic frequency for nonlinear device characterization. In: *82nd ARFTG Microwave Measurement Conference*, nov. IEEE, pp. 1–3.
- Cripps, S. C. (1999). *RF power amplifiers for wireless communications*. Artech House. p. 337.
- Darraj, R., Mousavi, P., and Ghannouchi, F. M. (2016). Doherty goes digital: Digitally enhanced doherty power amplifiers. *IEEE Microwave Magazine*, **17**(8): 41–51.
- DeGroot, D., Jargon, J., and Marks, R. (2002). Multiline TRL revealed. In: *60th ARFTG Conference Digest, Fall 2002*. IEEE, pp. 131–155.

- Doherty, W. H. (1936). Technical papers: A new high efficiency power amplifier for modulated waves. *Proceedings of the Institute of Radio Engineers*, **24**(9): 1163–1182.
- El-Deeb, W. S., Hashmi, M. S., Boulejfen, N., and Ghannouchi, F. M. (2011). On-line waveform monitoring system for the design and characterization of MIMO RF PAs. In: *Canadian Conference on Electrical and Computer Engineering*. pp. 001024–001027.
- El Mahalawy, M., Misljenovic, N., and Fayed, A. (2014). A load-pull approach using multi-frequency harmonic tuners for enhancing PAE and device model accuracy. In: *2014 IEEE 57th International Midwest Symposium on Circuits and Systems (MWS-CAS)*, aug. IEEE, pp. 603–606.
- Engen, G. and Hoer, C. (1979). Thru-Reflect-Line: An improved technique for calibrating the dual six-port automatic Network Analyzer. *IEEE Transactions on Microwave Theory and Techniques*, **27**(12): 987–993.
- Farsi, S., Draxler, P., Gheidi, H., Nauwelaers, B. K. J. C., Asbeck, P., and Schreurs, D. (2014). Characterization of intermodulation and memory effects using offset multisine excitation. *IEEE Transactions on Microwave Theory and Techniques*, **62**(3): 645–657.
- Ferrero, A. and Pisani, U. (1991). QSOLT: A new fast calibration algorithm for two port S Parameter measurements. pp. 15–24.
- Ferrero, A. and Pisani, U. (1992). Two-port network analyzer calibration using an unknown “thru”. *IEEE Microwave and Guided Wave Letters*, **2**(12): 505–507.
- Ferrero, A., Teppati, V., and Pisani, U. (2006). Recent improvements in real-time load-pull systems. In: *2006 IEEE Instrumentation and Measurement Technology Conference Proceedings*. pp. 448–451.
- F.L. Ogboi, P.J. Tasker, M. A. (2013). A LSNA configured to perform baseband engineering for device linearity investigations under modulated excitations. *IEEE*.
- Focus (2007). Comparing harmonic load-pull techniques with regards to power-added efficiency (PAE), Application Note 58.
- Ghannouchi, F. M. and Hashmi, M. S. (2013). *Load-Pull techniques with applications to power amplifier design*, Vol. 32 of *Springer Series in Advanced Microelectronics*. Springer Netherlands. Dordrecht.
- Ghannouchi, F. M., Larose, R., and Bosisio, R. G. (1991). A new multiharmonic loading method for large-signal microwave and millimeter-wave transistor characterization. *IEEE Transactions on Microwave Theory and Techniques*, **39**(6): 986–992.
- Gillet, V., Teyssier, J. P., Reveyrand, T., Laurent, S., Prigent, M., and Quere, R. (2018). A fully calibrated NVNA set-up for linearity characterization of RF power devices using Unequally Spaced Multi-Tone signal through IM3 IM5 measurements. In: *2018 91st ARFTG Microwave Measurement Conference: Wideband Modulated Test Signals for Network Analysis of Wireless Infrastructure Building Blocks, ARFTG 2018*, jul. Institute of Electrical and Electronics Engineers Inc.
- Hosein, B. and Beauchamp, T. (2013). EuMC: Impedance synthesis algorithms for hybrid harmonic load pull. In: *2013 European Microwaves Conference*. pp. 263–266.

- Kahil, S. A. K., Laurent, S., Quere, R., Sombrin, J., Floriot, D., Brunel, V., and Teyssandier, C. (2016). Linearity characterization of GaN HEMT technologies through innovative on-wafer multi-tone load-pull measurements. In: *2016 11th European Microwave Integrated Circuits Conference (EuMIC)*, oct. IEEE, pp. 37–40.
- Klopfenstein, R. W. (1956). A transmission line taper of improved design. *Proceedings of the IRE*, **44**(1): 31–35.
- Laurent, S., Kahil, S. A. K., Quere, R., and Sombrin, J. (2016). A multi-tone load pull measurement system for on-wafer characterization of microwave power transistors. In: *2016 46th European Microwave Conference (EuMC)*, oct. IEEE, pp. 1119–1122.
- Liang, C., Roblin, P., and Hahn, Y. (2019a). Accelerated design methodology for dual-input Doherty power amplifiers. *IEEE Transactions on Microwave Theory and Techniques*, **67**(10): 3983–3995.
- Liang, C., Roblin, P., Hahn, Y., Popovic, Z., and Chang, H. C. (2019b). Novel outphasing power amplifiers designed with an analytic generalized Doherty-Chireix continuum theory. *IEEE Transactions on Circuits and Systems I: Regular Papers*, **66**(8): 2935–2948.
- Liang, C., Niubo-Aleman, T., Hahn, Y., Roblin, P., and Reynoso-Hernandez, J. A. (2020). Optimal two-way hybrid Doherty-outphasing power amplifier. In: *2020 IEEE Topical Conference on RF/Microwave Power Amplifiers for Radio and Wireless Applications, PAWR 2020*, jan. Institute of Electrical and Electronics Engineers Inc., pp. 26–29.
- Lopez-Gonzalez, F., Marquez-Segura, E., Otero, P., and Camacho-Penalosa, C. (2006). Robust statistical multi-line TRL calibration approach for microwave device characterization. In: *MELECON 2006 - 2006 IEEE Mediterranean Electrotechnical Conference*. IEEE, pp. 187–190.
- Marchetti, M., Maier, T., Carrubba, V., Maroldt, S., Musser, M., and Quay, R. (2015). Examples of high-speed harmonic load pull investigations of high-efficiency GaN power transistors. In: *2015 IEEE International Conference on Microwaves, Communications, Antennas and Electronic Systems (COMCAS)*, nov. IEEE, pp. 1–4.
- Marks, R. (1991). A multiline method of network analyzer calibration. *IEEE Transactions on Microwave Theory and Techniques*, **39**(7): 1205–1215.
- Naraharisetti, N., Roblin, P., Quindroit, C., and Gheitanchi, S. (2015). Efficient least-squares 2-D-cubic spline for concurrent dual-band systems. *IEEE Transactions on Microwave Theory and Techniques*, **63**(7): 2199–2210.
- Nguyen, H. Q. and Barton, T. W. (2017). Linearity characterization of RF-input Chireix outphasing power amplifier. In: *2017 32nd General Assembly and Scientific Symposium of the International Union of Radio Science, URSI GASS 2017*, nov. Institute of Electrical and Electronics Engineers Inc., Vol. 2017-January, pp. 1–4.
- Niubo-Aleman, T., Hahn, Y., Roblin, P., Teyssier, J. P., Reynoso-Hernandez, J. A., Chen, V., and Rajan, S. (2019). Calibrated digital predistortion using a Vector Network Analyzer as the receiver. In: *2019 93rd ARFTG Microwave Measurement Conference: Measurement Challenges for the Upcoming RF and mm-Wave Communications and Sensing Systems, ARFTG 2019*, jun. Institute of Electrical and Electronics Engineers Inc.

- P. Dunsmore, J. (2012). *Calibration and vector error correction*, chapter 3, pp. 124–210. John Wiley & Sons, Ltd.
- Pozar, D. (2004). *Microwave engineering*, Vol. 2. Wiley.
- Pulido-Gaytán, M. A., Reynoso-Hernández, J. A., Loo-Yau, J. R., Zárata-De Landa, A., and Maya-Sánchez, M. D. C. (2015). Generalized theory of the thru-reflect-match calibration technique. *IEEE Transactions on Microwave Theory and Techniques*, **63**(5): 1693–1699.
- Pulido-Gaytán, M. A., Reynoso-Hernández, J. A., Maya-Sánchez, M. C., and Loo-Yau, J. R. (2016). Calibration of a real-time load-pull system using the generalized theory of the TRM technique. In: *87th ARFTG Microwave Measurement Conference: Measurements for Emerging Communications Technologies, ARFTG 2016*, jun. Institute of Electrical and Electronics Engineers Inc.
- Qiu, J. X., Darwish, A. M., Viveiros, E. A., Kingkeo, K., and Hung, H. A. (2011). Linearity characterization and optimization of millimeter-wave GaN HEMTs. In: *IEEE Transactions on Microwave Theory and Techniques*, dec. Vol. 59, pp. 3419–3427.
- Reveyrand, T., Courty, A., Portelance, M., Medrel, P., Bouysse, P., and Nebus, J. M. (2019). Automatic vector signal generator calibration method suitable for multiport large-signal measurements. In: *2019 93rd ARFTG Microwave Measurement Conference: Measurement Challenges for the Upcoming RF and mm-Wave Communications and Sensing Systems, ARFTG 2019*, jun. Institute of Electrical and Electronics Engineers Inc.
- Reynoso-Hernandez, J. A., Pulido-Gaytan, M. A., Maya-Sanchez, M. C., and Loo-Yau, J. R. (2012). What can the ABCD parameters tell us about the TRL? In: *79th ARFTG Microwave Measurement Conference*, jun. IEEE, pp. 1–4.
- Salib, M., Dawson, D., and Hahn, H. (1987). Load-Line analysis in the frequency domain with distributed amplifier design examples. In: *1987 IEEE MTT-S International Microwave Symposium Digest*. MTT005, pp. 575–578.
- Schreurs, D., ODroma, M., Goacher, A. A., and Gadringer, M., (eds.) (2008). *RF power amplifier behavioral modeling*. Cambridge University Press. Cambridge.
- Simbélle, F., Gillet, V., Laurent, S., Médrel, P., Creveuil, Y., Régis, M., Prigent, M., and Quéré, R. (2017). Envelope time-domain characterizations to assess in-band linearity performances of pre-matched MASMOS[®] power amplifier. In: *Digest of Papers - IEEE Radio Frequency Integrated Circuits Symposium*, jul. Institute of Electrical and Electronics Engineers Inc., pp. 7–10.
- Simpson, G. (2009). *A comparison of harmonic tuning methods for load pull systems*.
- Stancliff, R. and Poulin, D. (1979). Harmonic load-pull. *1979 IEEE MTT-S International Microwave Symposium Digest*, pp. 185–187.
- Taghavi, H., Akbarpour, M. H., and Ghannouchi, F. M. (2016). Sequential load-pull technique for multioctave design of RF power amplifiers. *IEEE Transactions on Circuits and Systems II: Express Briefs*, **63**(9): 818–822.

- Takayama, Y. (1976). A new load-pull characterization method for microwave power transistors. In: *MTT-S International Microwave Symposium Digest*. MTT005, Vol. 76, pp. 218–220.
- Tao, Y., Ishikawa, R., and Honjo, K. (2015). Optimum load impedance estimation for high-efficiency microwave power amplifier based on low-frequency active multi-harmonic load-pull measurement. In: *2015 Asia-Pacific Microwave Conference (APMC)*, dec. IEEE, pp. 1–3.
- Teppati, V., Ferrero, A., and Pisani, U. (2008). Recent advances in real-time load-pull systems. *IEEE Transactions on Instrumentation and Measurement*, **57**(11): 2640–2646.
- Teyssier, J. P., Sombrin, J., Quere, R., Laurent, S., and Gizard, F. (2014). A test set-up for the analysis of multi-tone intermodulation in microwave devices. In: *84th ARFTG Microwave Measurement Conference*, dec. IEEE, pp. 1–3.
- Tsironis, C. (2012). Active and hybrid harmonic load pull systems: An overview and comparison. In: *2012 Workshop on Integrated Nonlinear Microwave and Millimetre-wave Circuits*, sep. IEEE, pp. 1–3.
- Van Der Puije, P. and Mazumder, S. (1978). Two-signal method of measuring the large-signal S-parameters of transistors. In: *MTT-S International Microwave Symposium Digest*. MTT005, Vol. 78, pp. 263–266.
- Verspecht, J., Stav, A., Teyssier, J. P., and Kusano, S. (2019). Characterizing amplifier modulation distortion using a Vector Network Analyzer. In: *2019 93rd ARFTG Microwave Measurement Conference: Measurement Challenges for the Upcoming RF and mm-Wave Communications and Sensing Systems, ARFTG 2019*, jun. Institute of Electrical and Electronics Engineers Inc.
- Williams, T., Benedikt, J., and Tasker, P. J. (2004). Novel base-band envelope load pull architecture [rf device testing]. In: *High Frequency Postgraduate Student Colloquium, 2004*. pp. 157–161.
- Williams, T., Benedikt, J., and Tasker, P. (2005a). Experimental evaluation of an active envelope load pull architecture for high speed device characterization. In: *IEEE MTT-S International Microwave Symposium Digest*. IEEE, pp. 1509–1512.
- Williams, T., Benedikt, J., and Tasker, P. (2005b). Application of a novel active envelope load pull architecture in large signal device characterization. In: *2005 European Microwave Conference*. IEEE, p. 4 pp.
- Williams, T., Benedikt, J., and Tasker, P. (2006). Fully functional "real time" non-linear device characterization system incorporating active load control. In: *2006 European Microwave Conference*, sep. IEEE, pp. 1610–1613.

Appendix 1

To explain the TRL theory, the cascade T-parameters defined in equations 20 and 21, and the concept of line diagonalization are used. The T-parameters of a line with length L and propagation constant γ are defined in equation 129.

$$T_L = \frac{1}{(1 - \Gamma^2)e^{-\gamma l}} \begin{bmatrix} e^{-2\gamma l} - \Gamma^2 & \Gamma(1 - e^{-2\gamma l}) \\ \Gamma(1 - e^{-2\gamma l}) & 1 - \Gamma e^{-2\gamma l} \end{bmatrix} \quad (129)$$

A matrix T_L is diagonalizable when there exist a diagonal matrix and an invertible matrix T_Γ such that:

$$T_L = T_\Gamma T_\lambda T_\Gamma^{-1} \quad (130)$$

where T_Γ is the matrix containing the eigenvectors of matrix T_L and T_λ is a diagonal matrix containing the eigenvalues of T_L . T_Γ and T_λ are defined as indicated in equation 131.

$$T_\Gamma = \begin{bmatrix} 1 & \Gamma \\ \Gamma & 1 \end{bmatrix}, T_\lambda = \begin{bmatrix} \lambda & 0 \\ 0 & \frac{1}{\lambda} \end{bmatrix} \quad (131)$$

where $\Gamma = \frac{Z_{ref} - Z_L}{Z_L + Z_{ref}}$, Z_{ref} is the reference impedance, and $\lambda = e^{-\gamma L}$.

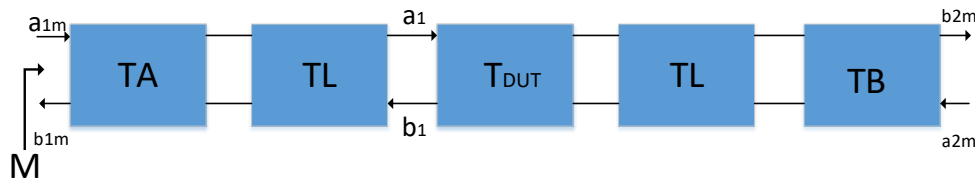


Figure 104. Representation of the DUT in a fixture with the error boxes of each port.

To find the measured matrix M shown in Figure 104 the T-parameters are used.

$$M = T_A T_L T_{DUT} T_L T_B \quad (132)$$

Substituting equation 130 in 132 result:

$$M = [T_A T_\Gamma] T_\lambda T_\Gamma^{-1} T_{DUT} T_\Gamma T_\lambda [T_\Gamma^{-1} T_B] \quad (133)$$

From equation 133 it is noticed that the reference impedance can be embed into the error boxes T_A and T_B as shown in equations below:

$$T_x = T_A T_\Gamma = D_x \begin{bmatrix} A_x & B_x \\ C_x & 1 \end{bmatrix} \quad (134)$$

$$T_y = T_\Gamma^{-1} T_B = D_y \begin{bmatrix} A_y & B_y \\ C_y & 1 \end{bmatrix} \quad (135)$$

were $A_{x,y}$, $B_{x,y}$, $C_{x,y}$, $D_{x,y}$ are the error terms.

The De-embedding is applied to equation 132 to obtain the measurements at DUT reference ports:

$$T_{DUT}^{Z_{line}} = T_\Gamma^{-1} T_{DUT}^{Z_{ref}} T_\Gamma = T_x^{-1} M T_y^{-1} \quad (136)$$

Connecting a general through as the DUT in Figure 104 results as:

$$M = T_x T_{\lambda_i} T_y = (D_x D_y) \begin{bmatrix} A'_x & B'_x \\ C'_x & 1 \end{bmatrix} \begin{bmatrix} \lambda & 0 \\ 0 & \frac{1}{\lambda} \end{bmatrix} \begin{bmatrix} A'_y & B'_y \\ C'_y & 1 \end{bmatrix} \quad (137)$$

From equation 137 it is noticed that using the 8-term error model results in 7 unknowns terms. The matrix $M = \begin{bmatrix} p_{11} & p_{12} \\ p_{21} & p_{22} \end{bmatrix}$ is the raw measurements captured with the VNA. Using the raw data $p_{i,j}$ and the equation 137 the following expressions are obtained for the error terms:

$$A'_y = \left(\frac{1}{C'_x} \right) \frac{p_{11} - p_{21} B'_x}{p_{22} \left(\frac{A'_x}{C'_x} \right) - p_{12}} e^{2\gamma L} \quad (138)$$

$$B'_y = \left(\frac{1}{C'_x} \right) \frac{p_{12} - p_{22} B'_x}{p_{22} \left(\frac{A'_x}{C'_x} \right) - p_{12}} e^{2\gamma L} \quad (139)$$

$$C'_y = \frac{\rho_{21} \left(\frac{A'_x}{C'_x} \right) - \rho_{11}}{\left(\frac{A'_x}{C'_x} \right) - \rho_{12}} \quad (140)$$

$$\frac{B'_y}{A'_y} = \frac{\rho_{12} - \rho_{22} B'_x}{\rho_{11} - \rho_{21} B'_x} \quad (141)$$

$$D_x D_y = \frac{\rho_{22} \left(\frac{A'_x}{C'_x} \right) - \rho_{12}}{\left(\frac{A'_x}{C'_x} \right) - B'_x} e^{-\gamma L} \quad (142)$$

The TRL technique uses the raw measurements of two lines (M_i, M_j) with arbitrary impedance Z_L , different lengths (L_1, L_2) and the same propagation constant (γ) to determine the error terms $\left(\frac{A'_x}{C'_x} \right)$ and B'_x .

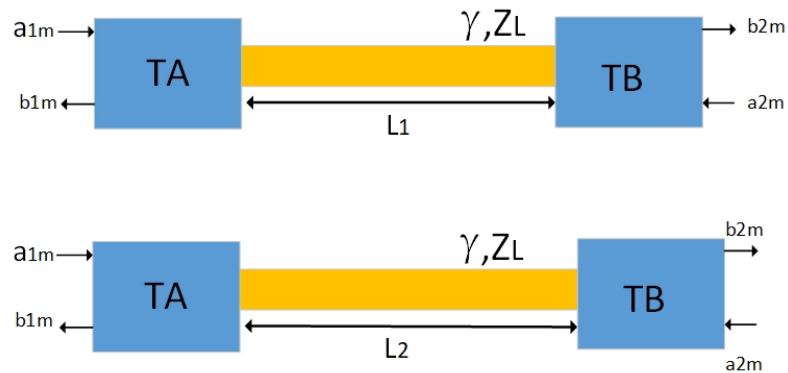


Figure 105. Two lines of different lengths.

$$\begin{aligned}
M_{i,j} &= M_i M_j^{-1} \\
M_{i,j} &= T_x T_{\lambda_i} T_y [T_x T_{\lambda_j} T_y]^{-1} \\
&= T_x T_{\lambda_i} T_y [T_x T_{\lambda_j} T_y]^{-1} \\
&= T_x T_{\lambda_i} T_y T_y^{-1} T_{\lambda_j}^{-1} T_x^{-1} \\
&= T_x T_{\lambda_i} \begin{bmatrix} 1 & 0 \\ 0 & 1 \end{bmatrix} T_{\lambda_j}^{-1} T_x^{-1} \\
M_{i,j} &= T_x T_{\lambda_{ij}} T_x^{-1} = \begin{bmatrix} k_{11} & k_{12} \\ k_{21} & k_{22} \end{bmatrix}
\end{aligned} \tag{143}$$

where $T_{\lambda_{ij}}$ is defined as:

$$T_{\lambda_{ij}} = T_{\lambda_i} T_{\lambda_j}^{-1} = \begin{bmatrix} e^{-\gamma L_1} & 0 \\ 0 & e^{\gamma L_1} \end{bmatrix} \begin{bmatrix} e^{\gamma L_2} & 0 \\ 0 & e^{-\gamma L_2} \end{bmatrix} = \begin{bmatrix} e^{\gamma(L_2-L_1)} & 0 \\ 0 & e^{-\gamma(L_2-L_1)} \end{bmatrix} \tag{144}$$

From equation 143 $T_{\lambda_{ij}}$ can be obtained:

$$T_{\lambda_{ij}} = T_x^{-1} M_{ij} T_x \tag{145}$$

By matching equations 144 and 145, a quadratic expression is derived for $\frac{A'_x}{C'_x}$ and B'_x :

$$\begin{aligned}
\left(\frac{A'_x}{C'_x}\right)^2 k_{21} + \frac{A'_x}{C'_x} (k_{22} - k_{11}) - k_{12} &= 0 \\
(B'_x)^2 k_{21} + B'_x (k_{22} - k_{11}) - k_{12} &= 0
\end{aligned} \tag{146}$$

The criterion to select the roots is $\Re\left(\frac{A'_x}{C'_x}\right) = \Re(B'_x)$. Knowing these parameters and

the length of the two lines (L_1, L_2) the propagation constant is compute as:

$$\gamma = \frac{1}{L_2 - L_1} \ln \left[\frac{\left(\frac{A'_x}{C'_x} \right) k_{11} - B'_x \left[\left(\frac{A'_x}{C'_x} \right) k_{21} + k_{22} \right] + k_{12}}{\left(\frac{A'_x}{C'_x} \right) - B'_x} \right], \quad L_2 > L_1 \quad (147)$$

The parameter C'_x is obtained using two identical reflected loads connected at port one and port two as indicated in Figure 106.

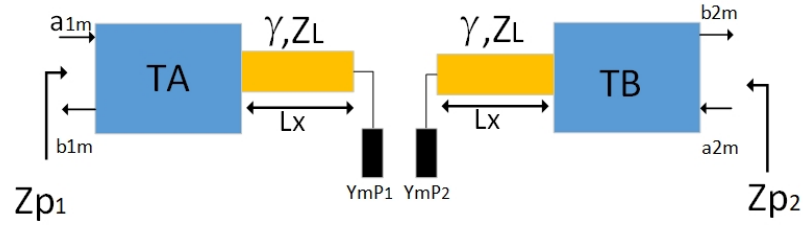


Figure 106. Reflected loads connected to each reference port.

Where Z_{p1} and Z_{p2} are the input impedance at port 1 and port 2 and are calculated as:

$$Z_{p1} = \frac{\frac{A'_x}{\lambda_{Lx}} [Z_L - Z_M] + \lambda_{Lx} B'_x [Z_L + Z_M]}{\frac{C'_x}{\lambda_{Lx}} [Z_L - Z_M] + \lambda_{Lx} [Z_L + Z_M]} \quad (148)$$

$$Z_{p2} = \frac{\frac{B'_y}{\lambda_{Lx}} [Z_M - Z_L] + \lambda_{Lx} [Z_L + Z_M]}{\frac{A'_y}{\lambda_{Lx}} [Z_M - Z_L] - C'_y [Z_L + Z_M]} \quad (149)$$

Where Z_M is a reflected load, the admittance at each port are calculated as:

$$Y_M^{p1} = Y_L \frac{\lambda_{Lx}^2 [B'_x - Z_{p1}] + [Z_{p1} C'_x - A'_x]}{[Z_{p1} C'_x - A'_x] - \lambda_{Lx}^2 [B'_x - Z_{p1}]} \quad (150)$$

$$Y_M^{p2} = Y_L \frac{\lambda_{Lx}^2 [C'_y Z_{p2} - 1] + [Z_{p2} A'_y - B'_y]}{[Z_{p2} A'_y - B'_y] - \lambda_{Lx}^2 [C'_y Z_{p2} - 1]} \quad (151)$$

Matching equations 150 and 151 the expression of C'_x is deduced, and the sign is

selected to guarantee :

$$C'_x = \pm \sqrt{\left[\frac{p_{11} - p_{21}B'_x}{p_{22}\frac{A'_x}{C'_x} - p_{12}} \right] \left[\frac{[B'_x - Z_{p1}][Z_{p2} - \frac{B'_y}{A'_y}]}{[Z_{p2}C'_y - 1][Z_{p1} - \frac{C'_x}{A'_x}]} \right]} e^{\gamma L_1} \quad (152)$$

To select the sign of C_x , a short is connected to port 1 therefore $Z_m = 0$, an estimated C''_x is obtained, where Zin^{sc} is the input impedance:

$$C''_x = \frac{B'_x - Zin^{sc}}{Zin^{sc} - \frac{A'_x}{C'_x}} \quad (153)$$

The *sign* is chosen such that:

$$\min_{sign} \{|C'_x - C''_x|^2\} \quad (154)$$

Appendix 2

In this Appendix the calibration procedure to obtain the term $(D_x)^2$ of equation 94, Γ_{out} , P_{out} , and G is detailed. Figure 107 shows the DUT output connected to the output reflectometer, where a_2 , b_2 are the reflected and the incident waveform at the output reference plane of the DUT, a_2^m and b_2^m are the raw data measured by the VNA.

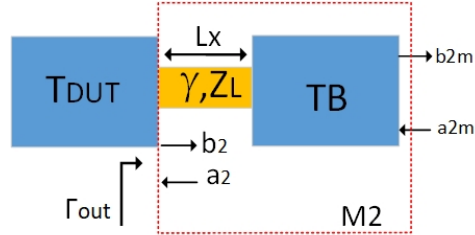


Figure 107. Scheme of the DUT output.

Using the diagonalization of a line with parameter T , the matrix M_2 is calculated as follows:

$$M_2 = T_z T_\lambda [T_z^{-1} T_B] \quad (155)$$

$$M_2 = T_z T_\lambda T_y \quad (156)$$

$$M_2 = D_y T_{M_2} \quad (157)$$

$$\begin{bmatrix} a_2 \\ b_2 \end{bmatrix} = D_y T_{M_2} \begin{bmatrix} a_2^m \\ b_2^m \end{bmatrix} \quad (158)$$

$$\text{where } T_{M_2} = \begin{bmatrix} t_{11} & t_{12} \\ t_{21} & t_{22} \end{bmatrix}$$

The $\Gamma_{22} = \frac{a_2}{b_2}$ is derived from equation 158 :

$$a_2 = D_y (t_{11} a_2^m + t_{12} b_2^m) \quad (159)$$

$$b_2 = D_y (t_{21} a_2^m + t_{22} b_2^m) \quad (160)$$

$$\Gamma_{22} = \frac{t_{11} \Gamma_{22}^m + t_{12}}{t_{21} \Gamma_{22}^m + t_{22}} \quad (161)$$

where Γ_{22}^m is the raw output reflection coefficient measured with the output reflectometer. Noticed that Γ_{22} represent Γ_{out} of the DUT for a load impedance of 50Ω . It is not possible to compute Γ_{out} for different load impedances using the conventional

two ports measurements. Therefore the TRL calibration technique for two-ports is not sufficient to obtain a real-time LP system.

The Figure 108 shows the scheme when the load tuner is connected to the measurement setup. The goal is to find an expression related Γ_{out} with Γ_t , which is the reflection coefficient at the reference plane of the load tuner. Therefore the output reflection coefficient can be obtained for all variations in the load.

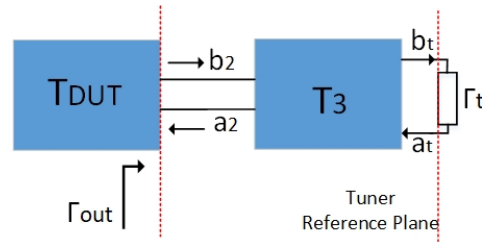


Figure 108. Scheme of the measurement setup when the load tuner is connected.

From Figure 108 the following expressions are deduced:

$$\begin{bmatrix} a_2 \\ b_2 \end{bmatrix} = T_3 \begin{bmatrix} a_t \\ b_t \end{bmatrix} \quad (162)$$

$$\begin{bmatrix} a_2 \\ b_2 \end{bmatrix} = t_{22_3} \begin{bmatrix} t_{11_3} & t_{12_3} \\ t_{21_3} & 1 \end{bmatrix} \begin{bmatrix} a_t \\ b_t \end{bmatrix} \quad (163)$$

$$\Gamma_{out} = \frac{t_{11_3}\Gamma_t + t_{12_3}}{t_{21_3}\Gamma_t + 1} \quad (164)$$

where t_{ij_3} are the unknown error terms of matrix T_3 , which represent the error boxes of a reflectometer, when the calibration at the load tuner reference plane is done by connecting three known standards and capture the measurements with the input reflectometer.

Using equation 163 Γ_t can be computed:

$$\begin{bmatrix} a_t \\ b_t \end{bmatrix} = \frac{1}{t_{22}^2 \Delta_{T_3}} \begin{bmatrix} 1 & -t_{123} \\ -t_{213} & t_{113} \end{bmatrix} \begin{bmatrix} a_2 \\ b_2 \end{bmatrix} \quad (165)$$

$$\Gamma_t = \frac{\Gamma_{22} - t_{123}}{-t_{213}\Gamma_{22} + t_{113}} \quad (166)$$

The error terms t_{ij_3} of the error box represented by T_3 are found by connecting a through between the input and output reflectometer, as shown in Figure 109. The measurements of three known standards connected at the output of T_3 are obtained with the input reflectometer.

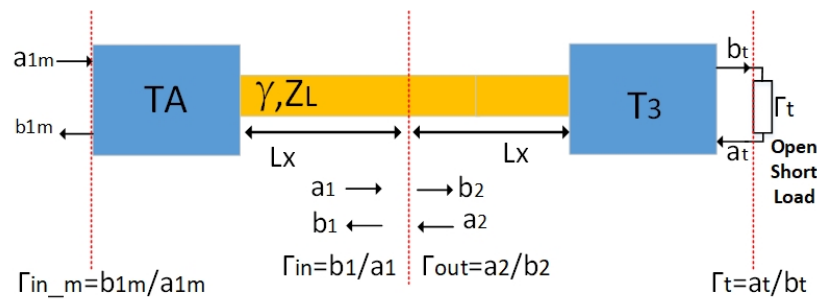


Figure 109. Through connection to measure the output reflection coefficients at DUT reference planes.

Using the TRL calibration technique, the input error box and Γ_{in} are computed. From the through connection, it is known that, $a_1 = b_2$, $a_2 = b_1$ and $\Gamma_{in} = \Gamma_{out}$, therefore:

$$\Gamma_{in} = \frac{t_{113}\Gamma_t + t_{123}}{t_{213}\Gamma_t + 1} \quad (167)$$

$$\Gamma_{in}(t_{213}\Gamma_t + 1) = t_{113}\Gamma_t + t_{123} \quad (168)$$

$$\Gamma_{in} = t_{123} - \Gamma_{in}\Gamma_t t_{213} + t_{113}\Gamma_t \quad (169)$$

From equation 169 an equation system of three unknown variables (t_{ij_3}) and three

equations is obtained:

$$\begin{bmatrix} \Gamma_{in}^{open} \\ \Gamma_{in}^{short} \\ \Gamma_{in}^{load} \end{bmatrix} = \begin{bmatrix} 1 & -\Gamma_{in}^{open} & -\Gamma_{open}^{ideal} & \Gamma_{open}^{ideal} \\ 1 & -\Gamma_{in}^{short} & -\Gamma_{short}^{ideal} & \Gamma_{short}^{ideal} \\ 1 & -\Gamma_{in}^{load} & -\Gamma_{load}^{ideal} & \Gamma_{load}^{ideal} \end{bmatrix} \begin{bmatrix} t_{12_3} \\ t_{21_3} \\ t_{11_3} \end{bmatrix} \quad (170)$$

$$A = MX \quad (171)$$

$$X = inv(M)A \quad (172)$$

where $t_{12_3} = X(1)$, $t_{21_3} = X(2)$, $t_{11_3} = X(3)$, Γ_{in}^j , ($j=open/short/load$), are the input reflection coefficients obtained at the DUT reference plane, Γ_j^{ideal} , are the ideal reflection coefficients of coaxial standards.

The output power of the device P_{out} is calculated evaluating equations 160 and 164 into 173:

$$P_{out} = |b_2|^2 (1 - |\Gamma_{out}|^2) \quad (173)$$

$$P_{out} = |D_y|^2 |t_{21} a_2^m + t_{22} b_2^m|^2 \left(1 - \left| \frac{t_{11_3} \Gamma_t + t_{12_3}}{t_{21_3} \Gamma_t + 1} \right|^2 \right) \quad (174)$$

To find $|D_x|^2$, $|D_y|^2$ terms of equations 94 and 174, respectively. A power sensor is connected at the output of T_3 , while the through is connected and the measurements are captured with the input port. The power measured by the power sensor at the output of port 2 is:

$$P_{mr} = |b_t|^2 - |a_t|^2 = |b_t|^2 (1 - |\Gamma_t|^2) \quad (175)$$

where Γ_t was defined in equation 166. Noticed that for the special case of a through connection, $\Gamma_{22} = \Gamma_{in}$.

From Figure 109 it is shown that the incident and reflected waveforms measured at the input port can be expressed as:

$$\begin{bmatrix} a_1^m \\ b_1^m \end{bmatrix} = D_x t_{22_3} \begin{bmatrix} t_{11} & t_{12} \\ t_{21} & t_{22} \end{bmatrix} \begin{bmatrix} t_{11_3} & t_{12_3} \\ t_{21_3} & 1 \end{bmatrix} \begin{bmatrix} a_t \\ b_t \end{bmatrix} \quad (176)$$

$$\begin{bmatrix} a_1^m \\ b_1^m \end{bmatrix} = D_x t_{22_3} \begin{bmatrix} x & y \\ z & w \end{bmatrix} \begin{bmatrix} a_t \\ b_t \end{bmatrix} \quad (177)$$

where x, y, z, w are the element of the matrix that results from the multiplication of T_{M_2} and T_3 .

From equation 177 the expressions for a_t and b_t are obtained as shown below:

$$a_t = \frac{b_1^m}{zD_x t_{22}} - \frac{wb_t}{z} \quad (178)$$

$$b_t = \frac{\alpha_1^m z - xb_1^m}{D_x t_{22} z (yz - xw)} \quad (179)$$

Evaluating equation 179 into equation 175 results:

$$P_{mr} = \left| \frac{\alpha_1^m z - xb_1^m}{D_x t_{22} z (yz - xw)} \right|^2 (1 - |\Gamma_t|^2) \quad (180)$$

$$|D_x|^2 = \frac{1}{P_{mr}} \left| \frac{\alpha_1^m z - xb_1^m}{t_{22} z (yz - xw)} \right|^2 (1 - |\Gamma_t|^2) \quad (181)$$

From the TRL calibration, the term $(D_x D_y)$ is obtained, therefore:

$$|D_y|^2 = \frac{|D_x D_y|^2}{|D_x|^2} \quad (182)$$

Finally, the gain of the DUT is calculated by evaluating equations 92 and 160 into 183 :

$$G = \frac{b_2}{a_1} \quad (183)$$

$$G = (D_x D_y) \left(\frac{t_{21} \Gamma_{out}^m + t_{22}}{m_{11} - m_{21} \Gamma_{in}^m} \right) (\Delta_M) \left(\frac{b_2^m}{a_1^m} \right) \quad (184)$$

The steps to calibrate the real-time load pull system proposed are summarized below:

1. The TRL calibration technique is performed with the port 1 and port 2 connected to the VNA. The through element is connected after the line and the reflect con-

nections.

2. Port 2 is disconnected from the VNA and three well known coaxial standards are connected to it and they are measured using the port 1 (while the through is connected between ports).
3. The power at the output of the port 2 is obtained by connecting a power sensor to it, and its reflection coefficient is measured with the input port while the through is connected.
4. After computing all the error terms, the validation of the calibration is required. For that, the raw measurements of a through are captured, and then the checking of $G = 0 \angle 0^\circ$, $P_{in} = P_{out}$, and $\Gamma_{in} = \Gamma_{out}$ is done.